

# Non-viral gemini surfactant-phospholipid nanoparticles for topical gene delivery to the retina

by

Samih Ahmad Alqawlaq

A thesis  
presented to the University of Waterloo  
in fulfilment of the  
thesis requirement for the degree of  
Master of Science  
in  
Pharmacy

Waterloo, Ontario, Canada, 2012

© Samih Ahmad Alqawlaq 2012

# Author's declaration

I hereby declare that I am the sole author of this thesis. This is a true copy of the thesis, including any required final revisions, as accepted by my examiners.

I understand that my thesis may be made electronically available to the public.

# Abstract

Glaucoma is a group of optic nerve degenerative diseases, which leads to gradual and permanent vision loss. Recent developments in the field of gene therapy have proposed increasingly promising treatments for glaucoma, in the form of delivery of neuro-protective or neuro-regenerative genes to the retina. Despite these developments, there are concerns related to the biocompatibility and invasiveness of common gene delivery systems, since they are commonly mediated by viral gene carriers and invasive administration methods. Non-viral gene delivery systems offer a safe and increasingly efficient alternative to deliver therapeutic genes to the retina. An example of these systems is gemini-phospholipid nanoparticles (GL-NPs), which have been successfully used to deliver genes in similarly challenging anatomical settings, such as the skin. The objective of this thesis is to demonstrate the potential of GL-NPs, as candidate gene delivery vehicles for topically administered genes, targeted to the retina.

The dicationic gemini surfactant, 12-7NH-12 was used, along with the helper lipids, 1, 2-dioleoyl-sn-glycero-3-phosphoethanolamine (DOPE), and 1,2-dipalmitoyl-sn-glycero-3-phosphocholine (DPPC), to prepare various types of GL-NPs, and assess their transfection efficiency in the rat retinal ganglion cell line (RGC-5). The transfection efficiency was evaluated using flow cytometry, as a function of several physical and chemical parameters of GL-NPs. These include a range of charge ratios (5:1 to 15:1  $p\pm$ ), helper lipid composition (several DOPE: DPPC ratios), order of assembly (plasmid-gemini + lipid versus gemini-lipid + plasmid), and manufacturing method of helper lipid vesicles (thin film versus high pressure homogenization method). Size and zeta ( $\zeta$ ) potential characterization of GL-NPs was carried out in parallel, using dynamic light scattering, to relate the physical parameters of GL-NPs to their respective

transfection efficiency. A comprehensive toxicological evaluation was undertaken to assess the extent of GL-NP's toxicity in RGC-5 cells, using the resazurin-based Prestoblu<sup>TM</sup> cell toxicity assay. Optimized GL-NPs were used to induce expression of the brain derived neurotrophic factor (BDNF) in RGC-5 cells, and were assessed in terms of their capacity to induce neurite outgrowth. Quantification of neurite outgrowth was carried out by measuring average neurite length in RGC-5 cells, by confocal microscopic imaging of immunostained neurites. Furthermore, confocal microscopic studies were carried out to assess the extent of GL-NP's corneal permeation in a 3-D human corneal epithelial (HCE) model. A parallel toxicological evaluation was completed to ensure GL-NP's biocompatibility with the corneal epithelial cells. Finally, GL-NP biodistribution pattern and gene transfer capacity was assessed in a mouse model, following topical and intravitreal administration.

The transfection efficiency in RGC-5 cells, which ranged between  $2.1 \pm 0.3\%$  and  $14.5 \pm 1.4\%$ , was highly dependent on GL-NP's charge ratio, helper lipid composition, order of assembly, and manufacturing technique. GL-NPs at 10:1  $p\pm$  charge ratio, assembled with homogenized DOPE (25%)-DPPC (75%) helper lipid vesicles, in the plasmid-gemini + lipid order, mediated the highest transfection efficiency in RGC-5 cells. These GL-NPs had a size of  $222.8 \pm 4.2$  nm and a  $\zeta$  potential of  $+33.5 \pm 2.9$  mV. Optimized GL-NPs were highly biocompatible with both RGC-5 and HCE model cells, with viability values ranging between  $94.8 \pm 6\%$  to  $100 \pm 3.4\%$ . Assessment of corneal permeation showed that GL-NPs were able to bind to the corneal epithelial surface and achieve a moderate permeation depth (35-40  $\mu\text{m}$ ), following topical application in the HCE model. Intravitreal injection of the non-viral GL-NPs in mice has successfully led to their localization within the nerve fiber layer (NFL) of the retina. Finally, GL-

NPs were non-invasively delivered to several anterior chamber tissues, including the limbus, the iris and conjunctiva, following topical administration.

GL-NPs offer several advantageous features critical to topical and intravitreal ocular administration of gene carriers, including *in vitro* corneal binding and effective biodistribution following *in vivo* topical and intravitreal administration, high biocompatibility, and a highly tunable transfection efficiency. The current data presents 12-7NH-12 GL-NPs as a promising candidate for ocular gene therapy applications.

# Acknowledgements

First and foremost, I would like to thank Dr. Marianna Foldvari for her generous support and encouragement over the course of the program. I would also like to extend my gratitude to my committee supervisors, Dr. John Flanagan and Dr. Michael Beazely, and Dr. Jeremy Sivak for sharing their knowledge and expertise. Thanks are also due to the Foldvari group's postdoctoral fellows, Dr. Torin Huzil, and Dr. Constanze Lamprecht for many helpful discussions and continuous advice. Marina Ivanova has provided valuable assistance in the *in vitro* corneal model assessment, and the *in vivo* experiment, and for that I am thankful. Additionally, my friend and colleague Chilbert Dong has been very supportive along the way in my technical aspects; a special thanks to him for all his help and friendship. Last, but not least, I am indebted to my family and friends for their unshakable faith in me over the years.

# Dedication

*“If it would cost me both of my eyes to educate my children, I will gladly meet that cost” –  
Mohamad Alqawlaq*

With utmost humility, I dedicate this work to my grandfather, Mohamad Alqawlaq, an extraordinary man, who is the very foundation of every success achieved in my family. I also dedicate this work to my father, Ahmad Alqawlaq, who carried the beacon after my grandfather, and continued his efforts to further the family’s education and excellence. Of course, this work would never have come to life if it wasn’t for our sun, my mother, Samia Ibrahim, who has never stopped giving or loving. In conclusion, this dedication would not be complete without the mention of my late brother and role model, Eyad (Sr.) Aqawlaq; you will always be with us.

# Table of contents

Author's declaration .....	ii
Abstract .....	iii
Acknowledgements .....	v
Dedication .....	vi
List of figures .....	xi
List of tables .....	xiii
List of abbreviations .....	xiv
1. Introduction .....	1
1.1. Glaucoma .....	1
1.1.1. Pathophysiology, cellular and molecular mechanisms of glaucoma: an overview	2
1.1.2. Current treatments and challenges .....	5
1.1.3. NTFs in neural regenerative medicine and glaucoma .....	6
1.1.4. Challenges of drug delivery to the retina .....	7
1.2. Ocular gene therapy .....	11
1.3. Performance of non-viral gene delivery systems in neuronal gene therapy .....	13
1.4. Neuronal gene delivery: challenges and solutions .....	16
1.4.1. Cellular binding and internalization .....	16
1.4.2. Retrograde transport and cytoplasmic trafficking .....	19
1.4.3. Endosomal escape .....	20
1.4.4. Nuclear entry and sustained gene expression .....	21
1.5. Gemini surfactants in gene delivery systems .....	22
1.6. <i>In vitro</i> and <i>in vivo</i> models for ocular drug delivery testing: an overview .....	24
1.7. Rationale and objectives of research .....	27
1.7.1. Rationale of research .....	27
1.7.2. Hypothesis .....	28
1.7.3. Objectives of research .....	29
2. Materials and methods .....	31
2.1. Plasmid DNA .....	31
2.1.1. pCMV6-AC-GFP .....	31
2.1.2. pCMV-tdTomato .....	32
2.2. NP preparation .....	33
2.2.1. Preparation of thin film helper lipid vesicles .....	34
2.2.2. Mode 1 assembly of original PGL <sub>DOPE</sub> NPs .....	35
2.2.3. Mode 1 preparation of PGL NPs with several helper lipid compositions .....	36
2.2.4. Mode 2 assembly of GL+P NPs .....	37
2.2.5. PGL NPs with microfluidized helper lipid vesicles .....	37
2.3. Assessment of particle size, polydispersity and zeta ( $\zeta$ ) potential .....	40
2.4. Transfection assay .....	40
2.4.1. 2.4.1 Cell culture and dose application .....	40
2.4.2. Cell harvesting .....	41
2.4.3. Fluorescence set up of flow cytometry analysis .....	42



2.5.	Confocal microscopic assessment of transfection efficiency .....	44
2.6.	Assessment of NP's toxicity in RGC-5 cells .....	44
2.7.	Assessing neurite outgrowth in RGC-5 cells following NTF expression.....	45
2.7.1.	Cell culture and dose preparation .....	45
2.8.	Assessment of permeation, and irritation of 12-7NH- 12 NPs in a human corneal epithelial model .....	47
2.8.1.	Cy5 labeling of pDNA for pDNA biodistribution assessment.....	48
2.8.2.	PGL <sub>DOPE</sub> NPs preparation for corneal permeation assessment.....	49
2.8.3.	Assessing corneal toxicity of NPs.....	50
2.9.	Pilot <i>in vivo</i> evaluation of biodistribution and transfection efficiency of NPs in mice eyes .....	51
2.9.1.	Animals and <i>in vivo</i> experimental design .....	51
2.9.2.	PGL NPs preparation for transfection assessment .....	51
2.9.3.	Experimental design .....	52
2.9.4.	Topical and intravitreal administration .....	54
2.10.	Tissue collection .....	56
2.11.	Statistical analysis.....	56
3.	Results.....	57
3.1.	Particle characterization of 12-NH-12 NPs .....	57
3.1.1.	PG complexes and PGL <sub>DOPE</sub> NPs of various $\rho_{\pm}$ charge ratios .....	57
3.1.2.	PGL NPs assembled with different helper lipid compositions.....	60
3.1.3.	GL+ P NPs assembled with DOPE and F4 helper lipid vesicles .....	62
3.1.4.	PGL <sub>MF</sub> NPs with microfluidized helper lipid vesicles.....	64
3.2.	Confocal microscopy assessment of transfection in RGC-5 cells .....	65
3.2.1.	Autofluorescence in RGC-5 cells .....	65
3.3.	Quantitative assessment of transfection using flow cytometry.....	67
3.3.1.	Transfection efficiency of PGL <sub>DOPE</sub> NPs as a function of charge ratio ( $\rho_{\pm}$ ) .....	67
3.3.2.	Transfection efficiency of PGL NPs as a function of helper lipid composition ....	68
3.3.3.	Transfection efficiency of GL+P NPs: effect of the order of assembly .....	70
3.3.4.	Transfection efficiency of PGL <sub>MF</sub> NPs with microfluidized helper lipid vesicles...	71
3.4.	Toxicity assessment of 12-7NH-12 based NPs in RGC-5 cells .....	74
3.5.	Assessment of RGC-5 neurite outgrowth as a function of BDNF expression in RGC-5 cells .....	76
3.6.	Assessment of PGL NP permeation and toxicity in an epithelial corneal model.....	80
3.6.1.	Permeation capacity of 10:1 $\rho_{\pm}$ 12-7NH-12 PGL <sub>DOPE</sub> NPs .....	80
3.6.2.	MTT assessment of PGL NPs toxicity in a HCE model.....	84
3.7.	<i>In vivo</i> evaluation of biodistribution and transfection in mice.....	86
3.7.1.	Evaluation of biodistribution of PGL <sub>DOPE</sub> NPs <i>in vivo</i> .....	86
4.	Discussion.....	89
4.1.	Design of 12-7NH-12 NPs for the retina .....	89
4.2.	Optimization of charge ratio of PGL <sub>DOPE</sub> NPs .....	92
4.2.1.	Size and $\zeta$ potential patterns of charge optimized PGL <sub>DOPE</sub> NPs.....	93
4.2.2.	Transfection efficiency of charge-optimized PGLDOPE NPs.....	97
4.3.	Optimization of helper lipid composition.....	100

4.3.1.	Effect of helper lipid composition on transfection efficiency .....	105
4.3.2.	Optimization of order of assembly .....	107
4.3.3.	Effect of order of assembly on transfection efficiency.....	110
4.3.4.	Optimization of NP manufacturing technique.....	111
4.3.5.	Effect of manufacturing technique of helper lipid vesicles on transfection efficiency .....	112
4.4.	Assessment of toxicity of PGL NPs in RGC-5 cells.....	113
4.5.	Effect of NP treatment on neurite outgrowth.....	114
4.6.	Assessment of corneal permeation and toxicity of PGL NPs in HCE tissue .....	118
4.7.	<i>In vivo</i> biodistribution and gene expression of PGL <sub>DOPE</sub> NPs after ocular application	121
4.7.1.	Intravitreally injected PGL NPs .....	121
4.8.	Topically administered eye drops of PGL <sub>DOPE-N</sub> NPs.....	124
5.	Conclusions and future direction.....	127
Copyright permissions .....		128
License for text and figures in introduction.....		128
License for figure used in methods (Figure 9-B).....		129
License for figure used in the discussion (Figure 30, 34).....		130
References .....		132

# List of figures

Figure 1	Glaucoma clinical characteristics.....	2
Figure 2	Structure and function of ocular factors contributing to the development of glaucoma.....	4
Figure 3	Biological barriers to topical administration of biotherapeutic molecules into the eye.....	10
Figure 4	Schematic representation of gene delivery into neural cells of the retina.....	18
Figure 5	Chemical structure of the helper lipid, DOPE.....	21
Figure 6	A schematic representation of gemini surfactants' dimeric structure.....	23
Figure 7	The bicistronic plasmid, pCMV6-AC-GFP encodes the mus musculus BDNF gene. .	32
Figure 8	The pCMV-tdTomato plasmid encodes the bright red fluorescent protein.....	33
Figure 9	Mattek EpiOcular HCE model compared to human cornea .....	48
Figure 10	Intravitreal (A) and topical (B) administration of NPs in 4-week old male C57BL/6N mice.....	55
Figure 11	Relationship between $\rho_{\pm}$ charge ratio and final PGL <sub>DOPE</sub> NP size .....	59
Figure 12	GFP expression in RGC-5 cells, stained with CBNF .....	66
Figure 13	Comparison of transfection efficiencies of PGL <sub>DOPE</sub> NPs prepared at a range of $\rho_{\pm}$ charge ratios in RGC-5 cells .....	68
Figure 14	Comparison of the transfection efficiency of PGL NPs in RGC-5 cells, as function of helper lipid composition .....	69
Figure 15	Comparison of the transfection efficiency of GL+P and PGL NPs, in RGC-5 cells.....	71
Figure 16	Comparison of the transfection efficiency of PGL NPs in RGC-5 cells, as a function of the manufacturing technique of helper lipid vesicles .....	72
Figure 17	Summary of 12-7NH-12 NPs' transfection optimization in RGC-5 cells .....	73
Figure 18	Assessment of cellular toxicity in RGC-5 cells, induced by PGL <sub>DOPE</sub> NPs, their intermediate complexes and individual components. ....	75
Figure 19	Assessment of cellular toxicity in RGC-5 cells, induced by helper lipid vesicles and corresponding PGL NPs .....	76
Figure 20	Assessment of neurite outgrowth in of RGC-5 cells, following treatments with several NPs and various concentrations of the BDNF protein. ....	78
Figure 21	CLSM images of RGC-5 cells, stained with Anti- $\beta$ III Tubulin Monoclonal Antibody, FITC conjugate.....	79
Figure 22	Confocal microscopic study of binding and permeation of 10:1 $\rho_{\pm}$ PGL <sub>DOPE</sub> NPs, 2 hours (A) and 15 hours (B) after topical application <i>in vitro</i> in the EpiOcular <sup>TM</sup> HCE model.....	81
Figure 23	Binding and permeation capacity of microfluidized GL <sub>MF-DOPE</sub> (A) and thin film GL <sub>DOPE</sub> vesicles (B), 25 hours after topical application.....	83
Figure 24	Assessment of corneal toxicity of several PGL NPs, and various surfactants in the EpiOcular HCE model .....	85
Figure 25	Biodistribution pattern of PGL <sub>DOPE-N</sub> NPs, 4 hours after topical application .....	87
Figure 26	Biodistribution pattern of PGL <sub>DOPE</sub> NPs 48 hours after intravitreal injection .....	88

Figure 27	Comparison of the change in $\zeta$ potential as a function of $\rho_{\pm}$ charge ratio in PG and PGL <sub>DOPE</sub> particles. ....	94
Figure 28	Stepwise assembly of PGL NPs and the associated structural characteristics .....	96
Figure 29	Particle size (black graph) and $\zeta$ potential (blue graph) of PGL <sub>DOPE</sub> NPs at different charge ratios. ....	97
Figure 30	A schematic diagram of the common cellular uptake mechanisms involved in uptake of NPs .....	99
Figure 31	Structure and symmetry of DOPE and DPPC lipids and their vesicular structural properties.....	102
Figure 32	Schematic diagrams and electron microscopic images of PGL NPs, assembled with different helper lipids compositions .....	104
Figure 33	Schematic illustration of dicationic-neutral mixed lipid membrane model .....	110
Figure 34	Primary mechanism involved in uptake of 10:1 $\rho_{\pm}$ PGL <sub>MF</sub> NPs in RGC-5 cells.....	113
Figure 35	Routes of transcorneal permeation of topically administered therapeutics .....	119
Figure 36	A schematic figure of the biodistribution pattern of intravitreally administered 10:1 $\rho_{\pm}$ PGL <sub>DOPE</sub> NPs in mouse eyes .....	122
Figure 37	Potential routes for topically administered, retina-targeted therapeutics.....	125
Figure 38	A schematic figure of the biodistribution pattern of topically administered PGL <sub>DOPE-N</sub> NPs in mouse eyes .....	126

# List of tables

Table 1	Summary of gene delivery systems used in non-viral gene delivery to the retina..	15
Table 2	A list of different PGL <sub>DOPE</sub> NPs prepared at a range of $\rho_{\pm}$ charge ratios .....	36
Table 3	A list of different PGL NPs, prepared using DOPE/DPPC and DPPC helper lipid vesicles.....	37
Table 4	Nomenclature explained.....	39
Table 5	A list of the fluorophores used in transfection and viability assessment.....	43
Table 6	Experimental design of <i>in vivo</i> experiment, and assignment of animals to the various conditions .....	53
Table 7	Size and PDI measurements of PG complexes and PGL NPs of various $\rho_{\pm}$ charge ratio.....	58
Table 8	$\zeta$ potential measurements of PG complexes and PGL NPs of various $\rho_{\pm}$ charge ratio .....	60
Table 9	Size and PDI measurements of PG complexes and their corresponding 10 $\rho_{\pm}$ PGL NPs.....	61
Table 10	$\zeta$ potential measurements of DOPE/DPPC helper lipid vesicles and their corresponding PGL NPs.....	62
Table 11	Size and PDI measurements of GL vesicles and GL+P NPs prepared with DOPE and F4 (25% DOPE-75% DPPC) lipid vesicles.....	63
Table 12	$\zeta$ potential of GL vesicles and GL+P NPs prepared with DOPE and F4 helper lipid vesicles .....	63
Table 13	Size and PDI of microfluidized helper lipid vesicles and the corresponding PGL <sub>MF</sub> NPs .....	64
Table 14	$\zeta$ potential of microfluidized helper lipid vesicles and the corresponding PGL <sub>MF</sub> NPs .....	65
Table 15	Advantages of employing the 12-7NH-12 gemini surfactant as a building block for a retina-targeted PGL NPs .....	90
Table 16	om values of PGL NPs assembled with DOPE/DPPC and DPPC helper lipid vesicles....	106

# List of abbreviations

BDNF	Brain-derived neurotrophic factor
CBNF	Carboxynaphthofluorescein
CD	Cup-to-disc ratio
CHO	Chinese hamster ovary cell line
CLSM	Confocal laser scanning microscopy
CMC	Critical micellar concentration
CNS	Central nervous system
CNTF	Ciliary neurotrophic factor
Coenzyme 3	C3
Crx	Cone-rod homeobox
DLC	Dynein light chain
DLC-AS	Dynein light chain -association signal
DLS	Dynamic light scattering
DOPC	1,2-dioleoyl-sn-glycero-3-phosphocholine
DOPE	1,2-dioleoyl-sn-glycero-3-phosphoethanolamine
DPPC	1,2-dipalmitoyl-sn-glycero-3-phosphocholine
DRG	Dorsal root ganglia
ECM	Extracellular matrix
FBS	Fetal bovine serum
FDA	Food and Drug Administration
FITC	Fluorescein isothiocyanate
GABA	gamma aminobutyric acid
GAGs	Glycoaminoglycans
GDNF	Glial cell line-derived neurotrophic factor
GFP	Green fluorescent protein
GL	Gemini-lipid vesicles
GL-NPs	Gemini-phospholipid nanoparticles
GTPase	Guanosine triphosphatase
H <sub>II</sub>	Inverted hexagonal phase
HCE	Human corneal epithelium
HSP	Heat shock proteins
IFN- $\alpha$	Interferon alpha
INL	Inner nuclear layer
IOP	Intraocular pressure of the eye
L $\alpha$	Lamellar phase
MTOC	Microtubule organizing centre
MTs	Microtubules
CMV	cytomegalovirus
PAM 212	Murine keratinocytes cell line
NE	Nuclear envelop

NFL	Nerve fibre layer
NMDRA	N-methyl Daspartate
NT4	Neurotrophic factor 4
NLS	Nuclear localization sequence
NTF	Neurotrophic factor
NP	Nanoparticle
NPC	Nuclear pore complex
OBF	Ocular blood flow
ONH	Optic nerve head
PC	Phosphatidylcholine
PC-12	Pheochromocytoma-12
PDI	Polydispersity index
PE	Phosphatidylethanolamine
PEG	Polyethylene glycol
PEI	Polyethyleneimine
PEO-PPO-PEO	Poly (ethylene oxide) - poly (propylene oxide) - poly (ethylene oxide)
PG	Plasmid/gemini complexes
PGL	Plasmid/gemini surfactant/lipid nanoparticles
PILs	Pegylated immunoliposomes
POD	Peptide for ocular delivery
RGC	Retinal ganglion cells
RGC-5	Rat retinal ganglion cell line
RPE	Retinal pigment epithelium
RPP	Rabies virus P-protein
SC	Superior colliculus
ScN	Sciatic nerve
scrAAV	Self complimentary recombinant adeno-associated virus
SDS	Sodium dodecyl sulfate
SiRNA	Small interfering ribonucleic acid
SLN	Solid lipid NP
SAXS	Small-angle X-ray scattering
$\sigma_m$	Surface charge density
Tf	Transferrin
$T_m$	gel-liquid crystal transition temperature
TM	Trabecular meshwork
TNF	Tumor necrosis factor
$\zeta$ potential	Zeta potential

# 1. Introduction

## 1.1. Glaucoma

Optic neuropathies remain one of the most debilitating and least treatable category of diseases in modern time. The defining feature of this category is an irreparable damage to the neural retina and the optic nerve (ON), which causes permanent vision loss. One such disease, which has received increasing attention from the scientific community over the past few decades, is glaucoma. Defined as a group of optic neuropathies, with a common phenotypic presentation of progressive and currently, irreversible vision loss, glaucoma is the second leading cause of vision loss worldwide. The estimated number of glaucoma patients is 60 million people, a figure that is expected to rise to nearly 80 million by the year 2020 [1, 2]. The immediate cause of glaucomatous vision loss is the death of retinal ganglion cells (RGCs). RGCs are neurons that relay visual signals to the central nervous system (CNS), via their axons, which converge to form the ON [3]. Glaucoma is most commonly diagnosed by the hallmark of optic disc cupping, which is an abnormal deepening of the optic nerve head (ONH). This observation, which is typically made by ophthalmoscopy [4], is a result of the excavation of RGC cells, their neighboring supporting glia, and significant rearrangement of the local extracellular matrix (ECM) [5]. In fact, the degree of disc cupping is used as a measure of the extent of glaucoma progression, with higher cup-to-disc ratio (Figure 1-A) indicating more advanced glaucomatous stages. This assessment is complemented by visual field examination (perimetry), which typically outlines the areas of visual field loss (Figure 1-B, C).



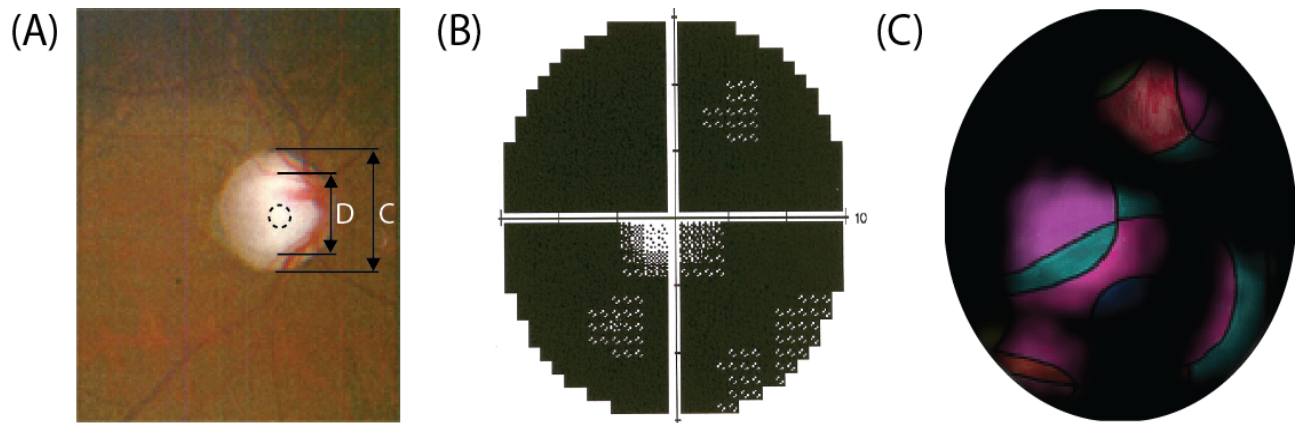


**Figure 1**      **Glaucoma clinical characteristics**

A) Photograph of a glaucoma patient's retina. The white bulb in the center is the optic nerve head showing optic disc cupping. The degree of optic nerve damage is clinically evident by ophthalmoscopy from the 'cupping' observed at the back of the eye expressed as the ratio of cup-to-disc (CD). The area normally occluded by the optic nerve is shown as a dashed circle in the center of the optic disc. B) Visual field (peripheral vision) test from the same glaucoma patient showed severe visual field loss (black areas). C) An example of the narrow 'tunnel' vision of a person with glaucoma. Perimetry examination reveals increasing areas of visual field loss with increasing CD ratio. *Adopted with permission from Alqawlaq et al, 2012 [6].*

### **1.1.1. Pathophysiology, cellular and molecular mechanisms of glaucoma: an overview**

The two most understood risk factors of glaucomatous death of RGCs (Figure 2-A) are increased intraocular pressure and poor perfusion of the retina. Increased intraocular pressure of the eye results from elevation in the intraocular pressure (IOP) of the eye, above the physiological range of 10-21 mmHg. A disturbance in the trabecular meshwork (TM) (Figure 2-B), which maintains normal IOP levels, through regulated drainage of the aqueous humor, is the most common cause of IOP elevation. On the other hand, several factors can lead to poor perfusion in the retina, most of which are manifested by vascular diseases (see review by[7]). These vascular dysfunctions play a major role glaucomatous degeneration, due to the resulting low ocular blood flow (OBF), which can be due to increased IOP or other abnormalities. Several

systemic factors can also contribute to glaucoma, including hypotension, low cerebrospinal fluid pressure, and autoimmune disorders [8-10]. Additionally, inter-individual differences in biomechanical features of the eye, such as scleral elasticity and thickness have become recognized as important glaucoma risk determinants [11]. These factors, among others, typically lead to an initial injury of the lamina cribrosa (Figure 2-C), which represents the 'trigger' of the glaucomatous neurodegenerative process.

It is widely accepted that the mode of RGC death is apoptotic [23-25]; however, the events and mechanisms responsible for triggering RGC apoptosis are still widely debated [6]. Several studies have shown that increased IOP contributes to the neurodegeneration process by restricting blood circulation in the retina and choroid [12-14], inducing glutamate and nitric oxide toxicities [15-18], inducing ECM changes that isolate RGCs from their neighboring support cells [19], and interruption of neurotrophic factor (NTF) transport between RGCs and visual centers in the CNS [20], to name a few. Similarly, reduced OBF, which creates a hypoxic environment in the retina, promotes the production of free radicals, such as nitric oxide which consequently induces oxidative stress on RGCs [9, 10]. Low OBF also mediates several other inflammatory and immunogenic reactions within the neuroretina, which further contribute to RGC death. These include astrocytes and microglia activation, excessive release of excitotoxic amino acids such as glutamate and D-serine in the extracellular space of RGCs [11-15]. A recent microarray study have also reported changes in the expression pattern of 225 genes related to cell proliferation, immune response, the extracellular matrix at early stages of injury in a rat glaucoma model [16]. This genetic change is typically manifested by activation of pro-apoptosis pathways and suppression of prosurvival pathways.

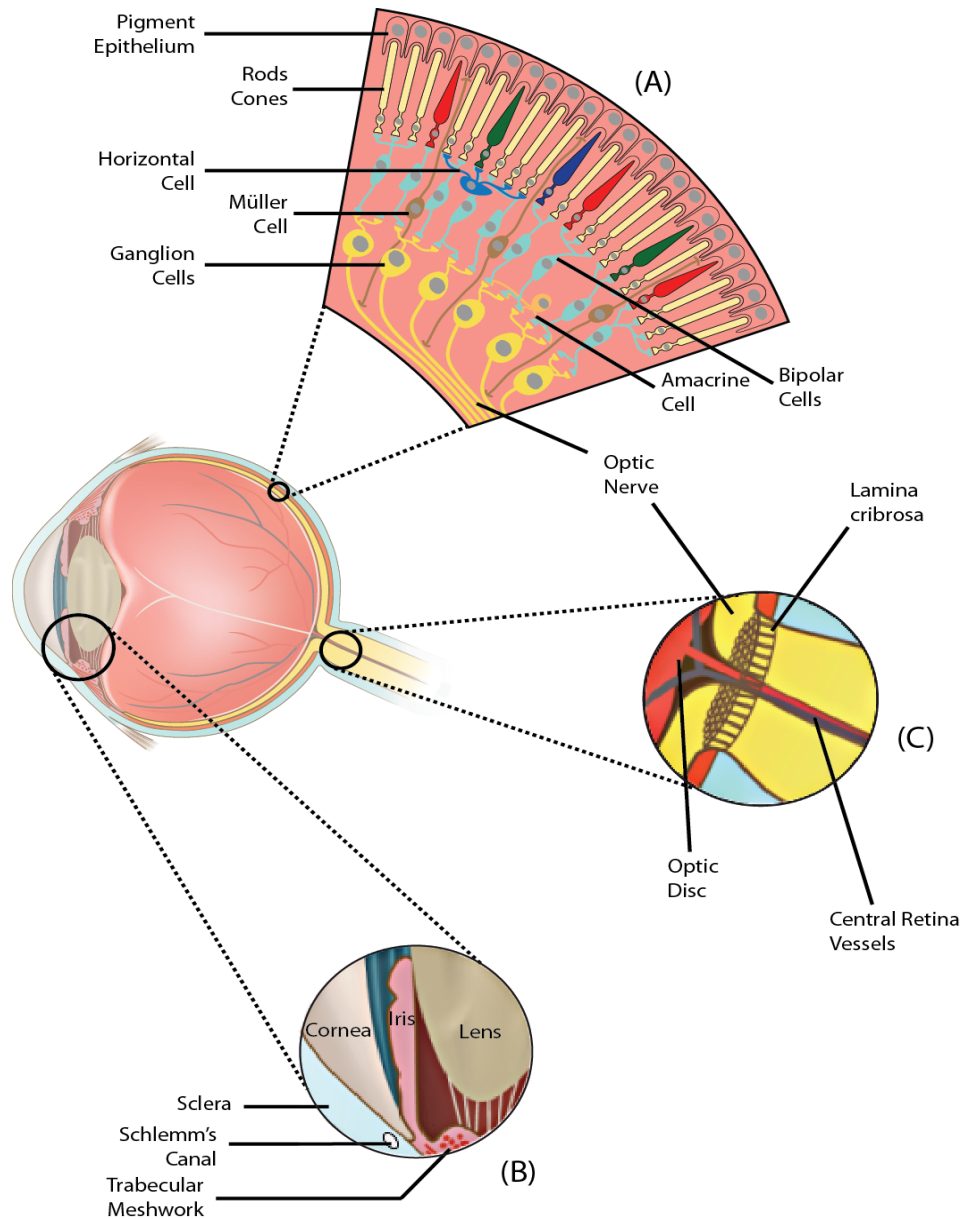


**Figure 2**

**Structure and function of ocular factors contributing to the development of glaucoma**

A) Cellular structure of the retina is shown with retinal ganglion cells (RGC), astrocytes, Müller cells, and the retinal pigment epithelium. B) The trabecular meshwork, located at the anterior angle of the eye is responsible for regulating normal ocular pressure by providing a moderate resistance to the flow of aqueous humor through its spongy tissue. C) The lamina cribrosa consists of perforated sheets of extracellular matrix through which the RGC axons pass towards the posterior of the eye. Mechanical damage may occur to the axons as they pass through the lamina cribrosa especially when they are 'squeezed' by increased pressure in the eye. *Adopted with permission from Alqawlaq et al, 2012 [6].*

### **1.1.2. Current treatments and challenges**

Currently, pharmacological treatments aimed at lowering IOP are the treatments of choice in health care systems around the world due to their baroprotective effects [21]. Beta-blockers, alpha agonists, and prostaglandin analogs are some the medication classes available to relieve elevated IOP. Notably, the required repeated administration may pose some side effects in some patients with pre-existing cardiac or asthma conditions. Similarly, surgical intervention is used to either increase the drainage rate of aqueous humor or reduce its production. One common surgical approach is the removal of a portion of the TM or creating pores in the TM using laser to increase drainage rate or reduce IOP. However, surgical procedures are invasive, and may not be suitable for patients with co-existing ocular diseases.

Several other pharmacological treatments are available to target RGC apoptosis mechanisms, such as oxidative and inflammatory stress (see reviews by [22-24]). Melatonin and Gingko biloba extract have been successfully used to combat oxidative-stress , through their targeting and neutralizing reactive oxygen species [25] . Another example is glatiramer acetate, a synthetic copolymer, derived from myelin basic protein, is being investigated for its potential in preventing harmful auto-immune reactions. Similarly, targeting the TNF-  $\alpha$  signaling pathway has also been shown as an effective way of controlling apoptosis in injured RGCs [26].

In general, while pharmacological and surgical interventions may control or delay glaucomatous vision, they are not able to reverse vision loss once it occurs. Presence of scar tissue at the neuronal damage site, gap formation in neuronal tissue as a result phagocytosis of dead neurons, and the inherent inability of neurons to spontaneously initiate axonal regeneration are all factors that challenge vision restoration in glaucoma [27]. To improve

treatment outcomes, there is a strong need to develop strategies to achieve neuronal protection and regeneration at the cellular level, by taking advantage of the available understanding of natural neuro-protective and neuro-regenerative mechanisms [28].

### **1.1.3. NTFs in neural regenerative medicine and glaucoma**

NTFs are small proteins that serve a critical role in the development, maintenance and functioning of neurons in the CNS, as well as the peripheral nervous system [29]. Deprivation of retinal neurons from sufficient NTF supply, due to bidirectional axonal transport obstruction at the ONH, is one the main causes of glaucomatous degeneration process. More specifically, this obstruction prevents proteins made by RGCs from reaching their axonal extensions, and blocks retrograde transport of NTFs, produced in the superior colliculus (SC), to reach the RGCs' soma [30]. Therefore, addressing this shortage of NTF support has become a major objective in glaucoma research, over the past few decades. Numerous studies have demonstrated that NTFs, including the brain derived neurotrophic factor (BDNF) [31], ciliary neurotrophic factor (CNTF) [32], sciatic nerve (ScN)-derived factors [33], glial cell line-derived neurotrophic factor (GDNF) [34], improve RGCs survival, and induce regeneration of their axons in several ON injury models [35-38]. Among the many examples of NTFs used, BDNF appears to provide the highest level of protection of RGCs, by compensating for the absence of bidirectional transport of NTFs. For example, following ON transection in adult rats, which leads to the death of approximately 50% of RGCs within the first week, a single injection of BDNF was shown to sustain RGCs survival for at least one week [39]. RGCs can be sustained for a longer period of time (additional two weeks), when a combination of NTFs are administered to the transected ON [37]. In addition to its ability to rescue injured RGCs, BDNF provides neurite extension guidance that

promotes the growth of severed neurons, and can act as a secondary neuro-protective agent in retinal support cells, such as glial cells [31, 40, 41]. BDNF's role in guiding axonal regeneration was suggested by studies that have shown that axonal growth cones respond to extracellular BDNF gradients in cell culture [42]. *In vivo* studies have also shown that BDNF modulates the synaptic formation process of neurons, which form increasingly sophisticated synaptic connections in the presence of BDNF [43]. Based on these considerations, delivery of NTFs to the retina appears to be a rational approach to addressing the glaucomatous neuronal degeneration, related NTF deprivation.

#### **1.1.4. Challenges of drug delivery to the retina**

In addition to identifying potential therapeutics for glaucoma treatments, it is important to employ an efficient administration method, capable of targeting the retina, without causing any harmful side effects. Generally, the methods used to reach the back of the eye are systemic, intravitreal (Figure 3-I), subconjunctival (Figure 3-II), and subretinal injection (Figure 3-III). Among these methods, intravitreal and subretinal injections are currently considered to be the most effective and common methods of gene delivery to RGCs. Intravitreal injections are commonly used for delivery to RGC and inner retinal interneurons. On the other hand, subretinal injections have been shown to be more effective in most cases for delivery to the outer retina. However, these methods are quite invasive and repeated delivery, using such methods, can cause further complications, such as retinal detachment, hemorrhages, and sub or pre-retinal fibrosis [44].

Parenteral administration allows for the delivery of larger volumes of therapeutics, and also allows for relatively safe repeated administrations. However, the therapeutic effect

achieved by these methods is very limited due to a restricting nature of the blood ocular barrier. The blood-ocular barrier is divided into two parts: the blood-aqueous barrier and the blood-retinal barrier (Figure 3-D). The blood-aqueous barrier is composed of the endothelial cells of the fenestrated blood vessels in the iris, and the pigmented cell layer of the ciliary epithelium [45]. This barrier protects the physical and chemical composition of ocular fluids, by preventing plasma albumin and hydrophilic molecules from accessing the aqueous humor [46]. On the other hand, the blood-ocular retinal barrier is comprised of retinal pigment epithelium (RPE), and the tight walls of the continuous retinal capillaries [47]. These retinal capillaries represent the bottle neck of systemic supply to the retina, allowing only small molecules and drugs to pass through.

Topical gene delivery (Figure 3-IV) to the ocular surface is the safest method for gene delivery since it is non-invasive and painless, compared to other delivery methods. This route of delivery is perhaps the most ambitious goal, due to the presence of several barriers that limit access of therapeutics to the posterior ocular tissue. First, the tear film (Figure 3A), which is an aqueous layer covered by lipids and underlined by mucin, covers the corneal and conjunctival layers and limits the bioavailability of applied therapeutics, due to tear turnover rate as well as lacrimal and nasolacrimal drainage. Tissue barriers, namely the cornea (Figure 3-B), conjunctiva, sclera, and choroid pose resistance to the passage of vectors due to the presence of epithelial tight junctions, proteoglycan matrices, and fibril collagen networks within their structures. The cornea is made up of several layers; a keratinized superficial layer, wing cell layer, basal cell layer, Bowman's membrane, stroma, Descemet's membrane, and an endothelium layer [48]. The corneal epithelium is the most limiting to drug delivery due to the presence of tight

junctions within its structure, allowing the selective passage of small molecules via the transcellular route [49]. The final barrier limiting to both topical and injected delivery of therapeutics to the retina is the vitreous (Figure 3-C), a primarily aqueous biogel consisting of collagen, hyaluronan, and proteoglycans. Electrostatic binding of anionic glycoaminoglycans (GAGs) to therapeutics, especially cationic ones, may alter their physical and the chemical integrity, therefore affecting their therapeutic potency [50].



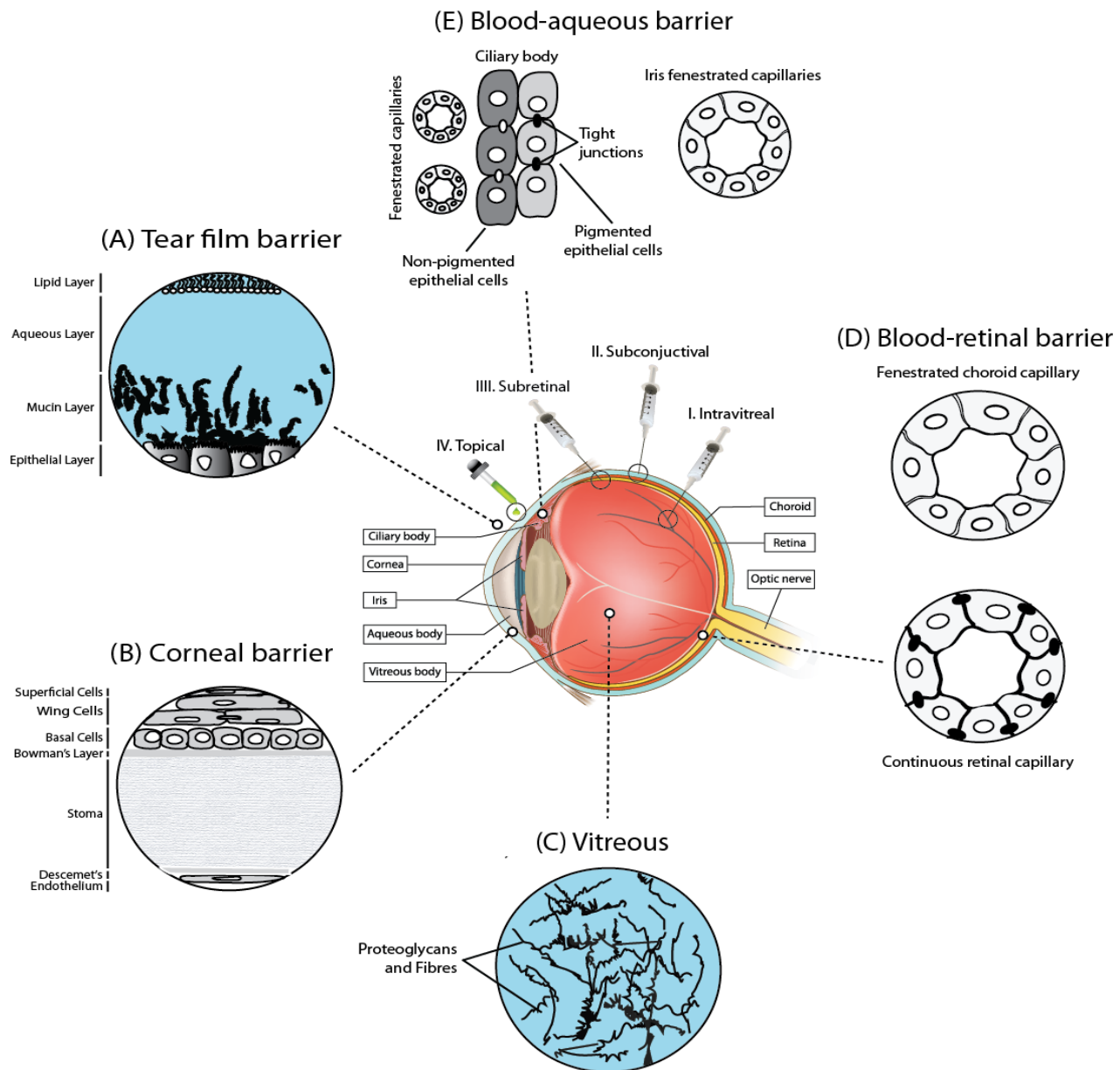


**Figure 3 Biological barriers to topical administration of biotherapeutic molecules into the eye.**

Several barriers to topical administration (IV) of drugs to the surface of the eye for delivery to the retina are illustrated. These include the (A) Tear film barrier; (B) Corneal barrier; (C) Vitreous, (D) Blood aqueous barrier and (E) Blood-retinal barrier. Several common delivery methods, including (I) Intravitreal injection; (II) Subconjunctival injection; and (III) Subretinal injection can bypass some of these barriers, but are invasive and can result in further damage to the eye. Adapted from Barar et al, 2008 and de la Fuente, 2010 [51, 52]. *Adopted with permission from Alqawlaq et al, 2012 [6].*

## 1.2. Ocular gene therapy

Gene therapy offers a promising potential to provide neuroprotective and regenerative treatments for glaucoma, by providing a twofold solution for treatment of neural glaucomatous degeneration. First, gene therapy aims towards the restoration of normal physiological functions, by combating deleterious mechanisms and restoring functional ones, at the molecular level. This is mainly achieved by delivery of a protective or an anti-apoptotic gene to injured RGCs. Second, the gene therapy approach provides solutions for effectively delivering therapeutic genes to the retina, by developing gene delivery systems that are capable of overcoming various ocular anatomical barriers. These systems range from eye drops and ointments to more advanced bio- and nanotechnology-based systems, including nanoparticles (NPs), immunoliposomes, polymeric micelles, muco-adhesive systems, iontophoresis, ocular inserts and viruses. For a gene delivery system to be effective, it must possess certain attributes. Firstly, levels of gene expression should be high enough to promote phenotypic improvement, without causing toxicity or need for repeated administration. Secondly, the therapeutic load should not cause immunogenic or inflammatory responses in the host [53]. In general, there are two approaches for the design of gene delivery systems, including viral and non-viral gene delivery systems. Viral gene delivery approaches employ the powerful DNA replication capacity of viruses to introduce therapeutic genes into target tissue. Using genetically modified viruses, whose native genome had been replaced with a therapeutic transgene, viral gene carriers can deliver therapeutic genes to target cells and tissues at a very high rate. Despite their potency, viral carriers have several disadvantages, including complicated manufacturing procedures, limited gene carrying capacity, inability to transfer genes to post-mitotic cells, and induction of

strong immunogenic and inflammatory responses [54]. In the context of ocular gene delivery applications, viral gene carriers have also shown a pattern of non-specific gene expression pattern, characterized by widespread gene expression around the target site. Provost et al. highlighted this phenomenon by evaluating the biodistribution of the viral rAAV vectors, following subretinal and intravitreal injection in dogs, rats and primates. The authors reported the presence of transgene sequences in the ON of rats and dogs following subretinal injection. More importantly, transgene sequences were also found in the brain, within the visual pathway, including the optic chiasma, the optic tract, the lateral geniculate nucleus, the colliculus, the optical radiation, and the visual cortex in rAAV-2/2 intravitreally injected dogs [55]. This passive biodistribution, which is often unwanted, is a result of the high gene delivery efficiency of viral vectors.

Non-viral gene delivery systems employ diverse cationic surfactants, polymers lipids and that compact DNA and protects it from cellular degradation mechanisms [56]. These systems rely on the electrostatic interaction between DNA's phosphate groups and the cationic head groups of the gene carrier to create NPs with various sizes and charge characteristics. This approach to gene delivery is preferred over the viral one for several reasons, including simple and economically feasible manufacturing procedures, low toxicity profiles, and ability to compact transgenes of various size ranges. However, non-viral vectors have a considerably lower transfection capacity, compared to viral vectors, therefore requiring significant development and optimization before achieving clinically significant outcomes [57, 58]. Despite this limitation, research and development of non-viral carriers has shown, and continues to show their potential as candidate glaucoma treatments.

### 1.3. Performance of non-viral gene delivery systems in neuronal gene therapy

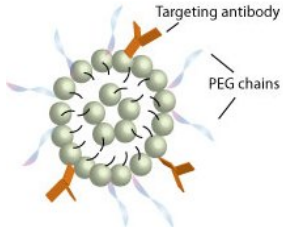
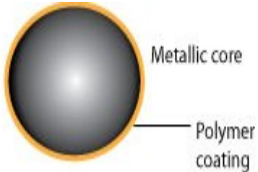
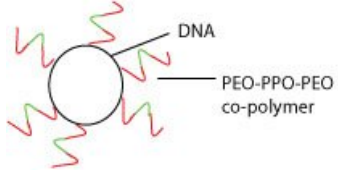
A considerable progress has been achieved, over the past ten years, in improving the gene transfer capacity of non-viral gene delivery systems *in vitro* and *in vivo*. Liposome- and polymer- mediated gene delivery systems are typically much more efficient in mitotic, immortalized neuronal cell lines than in post-mitotic primary cells. One study reported a transfection efficiency of 14% in the rat pheochromocytoma – 12 (PC-12) neuronal cell line, using polymeric polyethyleneimine (PEI)-based gene carrier. Another study reported a transfection efficiency range of 25-30% in the PC-12 cell line, using a dendrimer based transfection reagent [59]. The typical transfection efficiency of lipid-based systems in primary cortical neurons, which usually improves after several parameter optimization trials, ranges between 3%-25% [60]. Transfection efficiency was shown to improve by substituting the traditional plasmid DNA (pDNA) with small interfering RNA (siRNA), microRNA, or oligonucleotides, yielding efficiencies reaching as high as 80% [59, 61].

Several *in vivo* studies have also reported several successful attempts to deliver genes to the retina, using various administration methods (Table 1). For example, eye drop administration of poly(ethylene oxide)-poly(propylene oxide)- poly(ethylene oxide) (PEO-PPO-PEO) polymeric micelles were successfully used to induced gene expression around the iris, sclera, conjunctiva, and lateral rectus muscle of rabbit eyes and in intraocular tissue of nude mice [62, 63]. Two other studies reported successful gene delivery to retinal ganglion cells after topical administration of liposomes in rats [64, 65]. Another study employed chitosan-based NPs to in subretinal and intravitreal administration of PCMS-EGFP pDNA in rats. Gene expression was

reported in the retinal pigmented epithelium (RPE), following subretinal administration; while, intravitreal injection yielded gene expression in the inner nuclear (INL) and plexiform layers of the retina , especially in the RGC layer [66]. Intravenously delivered pegylated immunoliposomes (PILs) were successfully used to target several important ocular tissues of rhesus monkeys, including the retina, the ciliary body and the iris [67]. This was carried out, by conjugating the liposomes with a monoclonal antibody, targeted to the human insulin receptor, which is highly expressed in the outer nuclear layer of the retina and in the blood-retinal barrier. However, this approach carries a risk of non-specific absorption of the PILs by other tissues, which can result in serious toxicity issues. Recently, induction of the neuroprotective heat shock proteins (HSP) was achieved in rat retinas, by local magnetic heat stimulation of engineered superparamagnetic NPs [68]. Additionally, toxicity assessment of the superparamagnetic NPs demonstrated their safety as potential *in vivo* treatment agents.

**Table 1** Summary of gene delivery systems recently used in non-viral gene delivery to the retina

*Adopted with permission from Alqawlaq et al, 2012 [6].*

Nanocarrier	Carrier Description	Potential for treatment	Schematic diagram
Immunoliposomes	<p>Composed of a lipid bilayer, conjugated to an antibody that acquires the liposome a specific targeting functionality.</p> <p>Immunoliposomes can be further conjugated to PEG chains, which makes them especially advantageous in applications where vector shielding from ECM is needed.</p>	<p>Successful expression in the inner plexiform layer, the inner nuclear layer, the outer plexiform layer and the ganglion cell layer of monkey retinas using intravenously administered liposomes [67].</p>	
Magnetic NPs	<p>Composed of a metallic core that is coated with polymeric coatings that allow further functionalization of the NP. Offers the unique advantage of magnetic imaging of treated tissues.</p>	<p>Ocular biocompatibility assessment limited to no toxicity on the integrity of retinal cells, photoreceptor function or fluid circulation [68, 69].</p> <p>More recently, super-paramagnetic NPs were used to induce heat shock proteins [68].</p>	
Polymeric micelles	<p>Composed of amphiphilic polymers (containing both hydrophilic and hydrophobic regions) that self-assemble into nanosized particles capable of compacting and delivering DNA.</p> <p>Features include small size (&lt;150 nm), colloidal stability and a large surface area which can accommodate several functional moieties such as targeting ligands [70].</p>	<p>Successful gene delivery to retinal ganglion cells was achieved with these micelles after topical administration of liposomes in mice and rabbits [62, 63].</p>	

## **1.4. Neuronal gene delivery: challenges and solutions**

On the cellular level, neuronal gene delivery barriers include vector binding, internalization, retrograde axonal transport of distally internalized vectors towards the soma, endosomal escape, nuclear entry, and sustained gene expression [71].

### **1.4.1. Cellular binding and internalization**

Binding of naked DNA to the cell surface is typically very weak in the absence of a delivery agent due to the electrostatic repulsion that results between the DNA and the cell surface. Several DNA-condensing agents, mainly cationic lipids, have been used to enhance the vectors' binding to target cells and mediate the transfer of the DNA to the cytoplasm [72]. Furthermore, target-specific ligands can be bound to non-viral vectors to improve target specificity by ligand-receptor interactions. A wide variety of targeting ligands, including proteins, vitamins, carbohydrates, and hormones have been used for targeted DNA delivery [56].

Understanding the internalization of vectors in neuronal cells is a challenging task due to the compositional variations that exists across a neuron's different domains, including the soma, axon, and dendrites. A strong relationship appears to exist between temporal location of gene delivery along the neuron, and the efficiency of cellular internalization. More specifically, binding of cationic-lipid based delivery systems was reported to be more effective when NPs where applied near the soma, compared to when applied to distal neurites [73]. This was attributed to differences in heparan sulfate concentration between the soma and the distal neurites.

Generally, uptake of vectors into neuronal cells (Figure 4) typically occurs by endocytosis where they are engulfed by the cell membrane and taken up into endocytic vesicles. Several studies have shown the role of caveolae- and clathrin-mediated endocytosis in the internalization of various non-viral gene delivery systems [74, 75]. Recent efforts have been made to enhance the uptake rate of these mechanisms to improve cellular internalization, via conjugating integrin-targeting moieties on gene carriers ( see review by [76]).



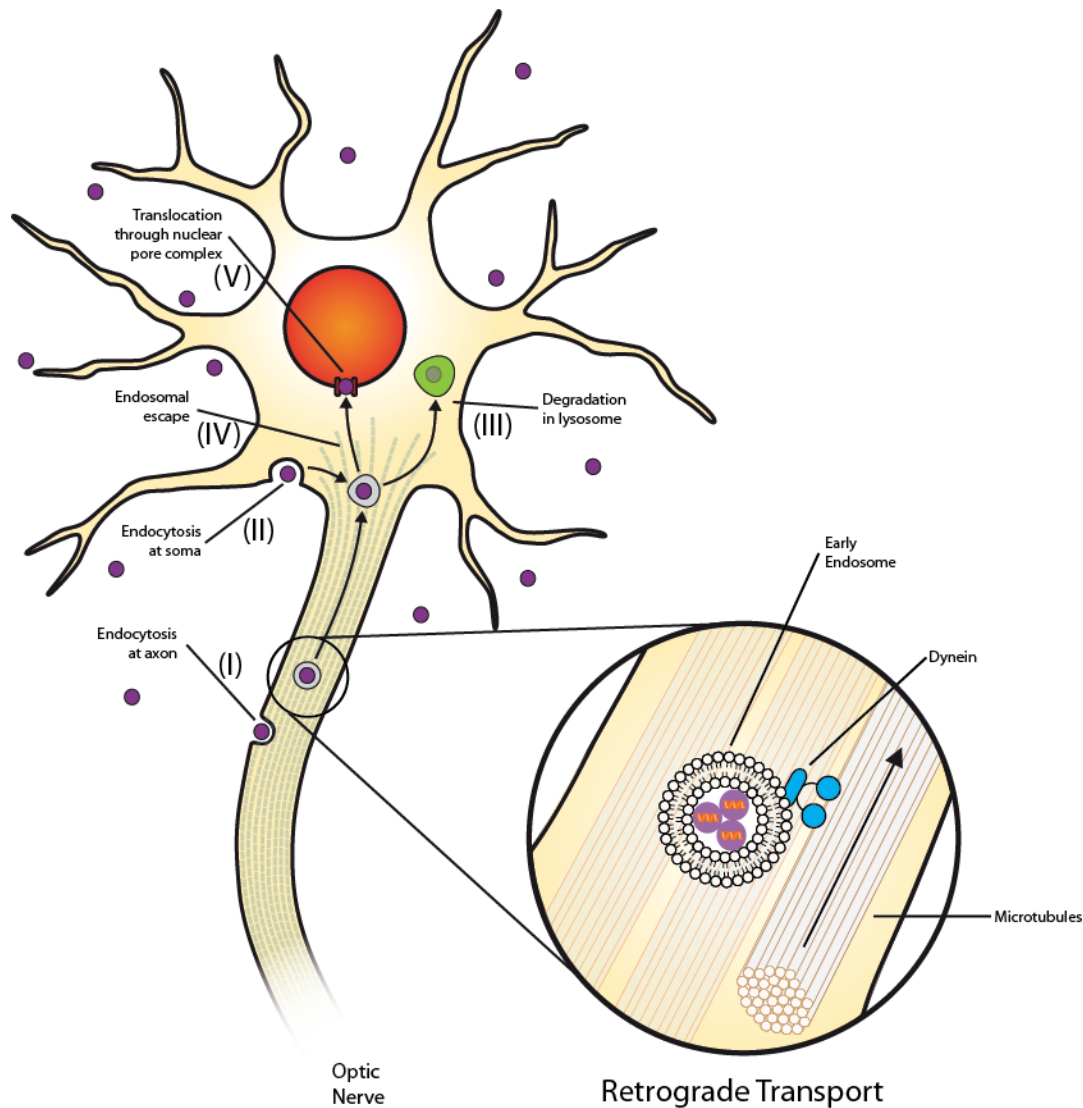


**Figure 4** Schematic representation of gene delivery into neural cells of the retina.

The process includes internalization of the gene, retrograde axonal transport, cytoplasmic trafficking, endosomal escape, and finally nuclear entry. The extent of gene internalization depends on the position of uptake on the cell surface. In neural cells, gene delivery systems are more extensively internalized at the soma than they are at the axon. (I) Gene delivery systems internalized at the axons or dendrites must undergo retrograde axonal transport towards the nucleus. This process is facilitated by motor proteins, such as dynein, along the surface of microtubules that run within the cytoplasm of the axons (Inset). (II) Gene delivery systems that are internalized at the soma do not undergo retrograde transport. (III) Internalized gene delivery systems must then travel through the cytoplasm's crowded environment filled with organelles and extensive microfilament network towards the nucleus. (IV) The genetic cargo contained within late endosomes must avoid lysosomal degradation and undergo timely endosomal escape. Finally, dissociation of the DNA-delivery system complex must occur at the right time and location for transgene to be translocated and processed in the nucleus (V). *Adopted with permission from Alqawlaq et al, 2012 [6].*

### **1.4.2. Retrograde transport and cytoplasmic trafficking**

Retrograde axonal transport (Figure 4 INSET) is an important process for neuronal signal transduction and communication. From a gene-delivery perspective, vectors delivered at a neuron's distal end must undertake retrograde axonal transport towards the soma in order to be effectively expressed [77]. Internalization at neurite ends represents a spatial barrier for distally delivered vectors, compared to vectors that are delivered near the soma (Figure 4). Some studies have attempted to utilize the dynein light chain (DLC) - association signal (DLC-AS), which is known for specific binding to dynein to improve the axonal transport process, which is highly dependent on dynein transport. One study highlighted this advantage by cloning the gene encoding the rabies virus P-protein (RPP), a well known DLC-AS, into a plasmid encoding GFP, followed by lipofectamine-mediated transfection of the plasmid in COS-7, HeLa, and Vero cell lines. As a result of the RPP/GFP gene expression, fluorescence was associated specifically along the cells' MT network and around the microtubule organizing centre (MTOC) of the cells' nuclei [78]. These results suggest the potential of DLC-AS in guiding exogenous cargo towards the nuclei of target cells.

The highly crowded environment of the cytoplasm is the main limiting factor for the diffusion of vectors towards the nucleus (Figure 4-III) [79]. The dispersion of cellular organelles as well as the presence of elaborate cytoskeleton networks represents a major obstacle to the vector trafficking in the cytoplasm, especially those that are relatively large in size. Several studies have shown an inverse relationship between the size of DNA fragments and their rate of diffusion through the cytoplasm [80].

### 1.4.3. Endosomal escape

Following entry into the cell by endocytosis, vectors typically follow the lysosomal trafficking pathway which eventually results in the degradation of the vector by lysosomal enzymes (Figure 4-III) [81]. Therefore, the ability of vectors to avoid this pathway, by escaping the endosome in time (Figure 4-IV), is a critical requirement for successful gene transfer. Typically, this occurs by disrupting the limiting membrane of the endosome by either electrostatic interaction between anionic lipids of the limiting membrane or by induced endosomal rupture. Incorporating the lipid, 1, 2-dioleoyl-sn-glycero-3-phosphoethanolamine (DOPE) (Figure 5) in cationic- and lipid-based vectors has been shown to mediate endosomal escape by undergoing a phase transition from the bilayer to the inverted hexagonal ( $H_{II}$ ) form at endo/lysosomal pH (see review by [82]). This phase transition is believed to be the trigger for endosomal escape of DOPE-based vector formulations. Another way to mediate endosomal escape is the use of cationic polymers with the ability to buffer endosomal pH. These polymers typically exhibit a buffering capacity below physiological pH, making them effective “proton sponges” [83]. Hence, protonation of these polymers following endosomal acidification triggers osmotic swelling of the endosome due to ion influx. This leads to destabilization and burst of the endosomal membrane. Examples of these polymers are polyethyleneimine (PEI) and other polyamine dendrimers [84].

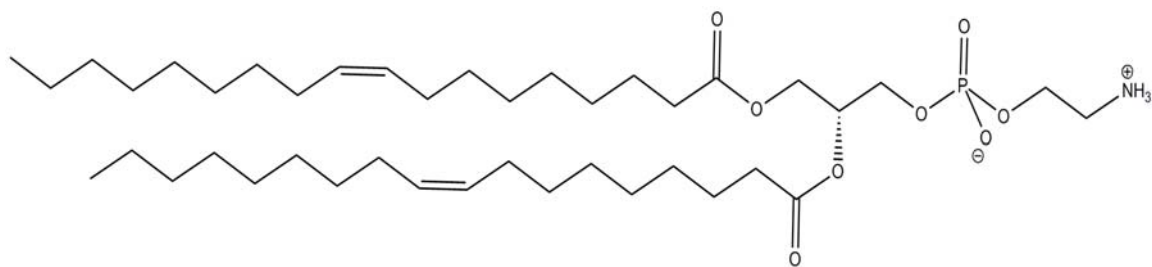


**Figure 5**      **Chemical structure of the helper lipid, DOPE**

DOPE is incorporated into various non-viral gene delivery systems to improve their transfection efficiency, by mediating effective endosomal escape.

#### **1.4.4. Nuclear entry and sustained gene expression**

Successful transgene expression also requires the passage of nucleic acid through the nuclear envelope, following endosomal escape to allow access of cellular transcriptional machinery to the transgene. To gain nuclear entry, vectors must pass through the nuclear pore complex (NPC) (Figure 4-V), which are large transmembrane proteins that mediate the cytoplasmic-nuclear transitions of macromolecules [85]. NPCs form aqueous pores within the nuclear pores which gives them the structural flexibility needed to expand their diameter up to 25 nm during active translocation, as opposed to a diameter of 9 nm during passive transport [86-88]. Macromolecules with sizes above the passive diffusion size limit (60 kDa) contain a targeting signal known as nuclear localization sequence (NLS). NLS typically consists of either one or two stretches of basic amino acids whose function is to specifically bind to nuclear surface proteins. These surface proteins, namely importins facilitate transfer of molecules through the nuclear pore in an energy dependent manner [89]. The incorporation of NLS within delivery vectors has been suggested by few studies as a method of improving intranuclear transport [90]. One study successfully identified the nucleic acid sequence of the gene encoding the NLS for nuclear transport of the photoreceptor-specific transcription factor cone-rod

homeobox (Crx) [91]. The NLS for Crx can be potentially utilized for ocular gene delivery trials, to achieve improved nuclear trafficking and gene transfer capacity. However, extensive technical improvement is needed in the ocular gene delivery field in order to realize the full potential of integrating NLS in delivery vectors.

Advanced methods to prolong gene expression include ocular and intravitreal implants. Recently, the intravitreal implant of dexamethasone was approved by the Food and Drug Administration (FDA) to treat retinal vein occlusion. A recent randomized placebo-controlled study showed that dexamethasone intravitreal implant was effective in reducing vision loss and in improving the visual recovery in retinal vein occlusion patients [92]. This is an encouraging result for further research to develop more ocular implants for sustained gene release as a step towards treating glaucoma and other retinopathies.

### **1.5. Gemini surfactants in gene delivery systems**

Gemini surfactants are molecules, composed of two hydrophilic head groups and two hydrophobic tails, linked by a spacer group (Figure 6). Conventional amphiphilic molecules (composed of a single hydrophobic tail connected to a polar head group) are often used as gene carriers due to their ability to compact DNA into micelles, capable of overcoming the various gene delivery barriers. Gemini surfactants, on the other hand have an advantage over conventional surfactants, which is their low critical micellar concentration (CMC), the minimum concentration above which surfactants form micelles. The low CMC of gemini surfactants reduces their toxicity profile, due to their functionality at lower concentrations, which also makes them more economically feasible [93].

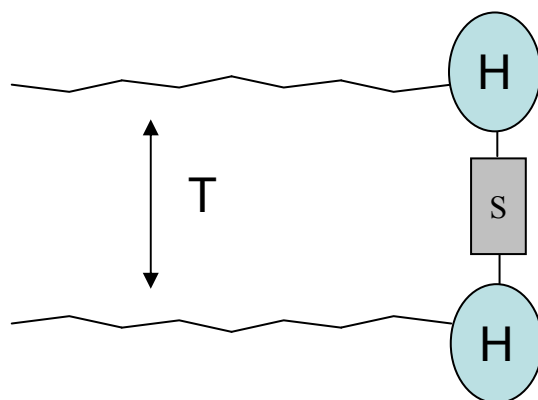


**Figure 6** A schematic representation of gemini surfactants' dimeric structure

Gemini surfactants are composed of two amphiphilic molecules, connected by a spacer group (S). Each amphiphilic molecule is composed of a polar head group (H) and a hydrophobic tail group (T).

The alkyl chain-spacer-alkyl chain structure of gemini surfactants serves as a template to an essentially unlimited number of potential structures [93]. This chemical diversity can be achieved by modifying the length or chemical composition of both the tail and spacer groups or by changing the polarity of the head groups. In fact, changing these parameters significantly influences transfection efficiency of gemini carriers. For example, increasing the tail length, while keeping spacer length constant, was shown to increase the transfection efficiency of gemini NPs in the PAM 212 keratinocyte cell line [94]. Similarly, amine, amino-acid, or carbohydrate substitution in the spacer group of gemini surfactants have been shown to significantly increase their transfection capability (as high as 90%) in several cell lines [93, 95, 96]. Gemini surfactants have also demonstrated significant success in studies performed *in vivo*. In a recent study, 16-3-16 gemini NPs carrying the interferon alpha (IFN- $\alpha$ ) gene, were topically applied on the skin of IFN- $\alpha$  deficient mice. Application of the NPs resulted in a clinically

significant increase in IFN- $\alpha$  expression in skin of treated mice, compared to the intradermally injected IFN- $\alpha$  gene [97].

Performance of gemini surfactant-based carriers can be improved by incorporating secondary components, including various phospholipids, known as helper lipids. The helper lipid, DOPE is one of the most common lipids used along with cationic transfection agents. Inclusion of DOPE improves the overall transfection efficiency of the gemini-based carrier, reduces their toxicity, and increases their colloidal stability both *in vitro* and *in vivo* [94]. At pH 9, DOPE forms lipid vesicles capable of further compacting various DNA-cationic lipid and polymer NPs.

### **1.6. *In vitro* and *in vivo* models for ocular drug delivery testing: an overview**

Cellular and tissue models are often used in early stages of assessment of ocular drug delivery systems. Testing in these models provides useful information on the gene transfer efficiency, biodistribution pattern, and toxicity of a gene delivery system of interest. Cell models, commonly used in glaucoma research, include immortalized cell lines, primary cells, and tissue explants, and animal models. The transformed retinal ganglion cell line (RGC-5) is a useful *in vitro* model for early gene delivery assessment in RGCs. RGC-5 cells express several neuronal markers, typically expressed in RGCs, which are also involved in the glaucomatous neurodegenerative process. These include Thy-1, Brn-3c, *N*-methyl d-aspartate (NMDAR1) and the  $\gamma$ -aminobutyric acid (GABA-B) receptors [98]. The main advantages of using RGC-5 cells include simple handling and preparation requirements, and economical feasibility of completing high throughput assays. However, there are some considerations to be taken into account when extrapolating findings in RGC-5 cells to *in vivo* settings. Unlike primary RGCs,

RGC-5 cells are mitotic, a property that generally enhances the gene delivery process, due to transgene transfer from parent to daughter cells. Therefore, the obtained transfection efficiency in RGC-5 cells has to be interpreted with caution, since it may be overstated. The mitotic nature of RGCs can also contribute to genetic mutations overtime, which may lead to manifestation of physiological features, different from RGCs *in vivo*. Despite these differences, RGC-5 cells exhibit a reasonable physiological and functional resemblance to RGCs, and hence can serve as a starting point for *in vitro* evaluation of gene delivery systems.

Similarly, numerous types of *in vitro* corneal models have been developed to assess toxicity, as well as the binding and permeation kinetics of topically applied therapeutics within the cornea. These include primary corneal explants, immortalized corneal cell culture models, and *in vitro* corneal epithelial cell models, all of which have been extensively reviewed by Hornof et al [99]. Given that the corneal epithelium is a major rate-limiting barrier for topically applied therapeutics, several studies employ epithelial corneal models in early drug development stages. These models offer a comparable 3-dimensional structure and similar resistance properties to that of the intact corneal epithelium. Use of these models also addresses the ethical concern of sacrificing a large number of animals, over multiple time points, to assess the corneal permeation of a single drug [99].

Several animal models have been used to study the mechanisms of glaucomatous degeneration and test potential treatments. Common methods of simulating glaucomatous injury include induction of elevated IOP, via TM obstruction, or performing ON transection in animals including, mice, rats, rabbits, monkeys, dogs, and several others [100]. Mice and rats are the most commonly used animals in glaucoma studies, mainly due to cost, and labour



considerations. The DBA/2J mouse, which develops IOP-induced glaucoma, as a result of iris abnormalities, is a common and convenient glaucoma model [101]. Preliminary assessment of gene delivery-based glaucoma treatment does not necessarily require testing in a glaucoma animal model, since focus at early stages is on the biodistribution and gene transfer capacity, as opposed to therapeutic outcome. The main disadvantage of using mice for *in vivo* assessment of a gene delivery system is their small eye size, and the relatively large size of the lens, which occupies a significantly large space of the inner ocular volume.

## **1.7. Rationale and objectives of research**

### **1.7.1. Rationale of research**

Gene therapy offers a potentially effective solution for glaucoma treatment in areas where traditional treatments fall short, such as promotion of RGC survival and neuroregeneration. While traditional treatments mainly aim to decrease IOP, gene therapy approaches could address the root causes of glaucomatous vision loss, by addressing the underlying genetic mechanisms that control neuronal survival and regeneration. In order to achieve this goal, effective and safe gene delivery systems are needed to navigate the eye's well-protected anatomy and deliver therapeutic genes to target tissues. Additionally, a safe delivery method is needed to mediate this process non-invasively and painlessly.

Despite their potential, only a limited number of studies reported successful gene delivery to the retina by non-viral gene delivery systems, and a smaller number employed non-invasive delivery methods. The majority of successful attempts employed viral gene delivery systems, or needle-based administration methods, or both. Inclination to use these approaches is a reflection of the numerous challenges associated with non-viral or non-invasive gene therapy tools, both on the cellular and anatomical levels. To name one example, the tight epithelial junctions of ocular tissues, namely the cornea are permeable only to NPs with a diameter of less than 200 nm [102]. Given the various risks associated viral and needle-based approaches, there is a strong motivation to investigate and develop efficacious non-viral gene delivery systems that can be topically applied to the eye.

The substituted class of gemini surfactant gene delivery systems is an excellent candidate to undertake this objective. There are several attractive features that make

substituted gemini surfactants suitable candidates as glaucoma gene therapy systems. First, gemini surfactants are flexible to numerous chemical modifications, resulting in unique physicochemical properties, which are often needed to improve the gene transfer process to hard-to-reach organs. This structural flexibility provides a selection of gene delivery carriers with a spectrum of size, charge, or pH. Second, gemini surfactants are cationic, which has been shown to aid gene carriers in binding to and permeating through the negatively charged cell membranes. This electrostatically assisted permeation is especially evident between cationic carriers and the negatively charged corneal surface [103-105].

With many working models of this gene delivery system, this system can carry a variety of neuro-protective and neuro-regenerative genes that can slow down or halt a range of neurodegenerative mechanisms. Among these therapeutic genes is the critical NTF genes, and specifically BDNF. BDNF is an excellent choice for a model therapeutic gene, due to its various protective and regenerative functions in neurons, including RGCs. Therefore, incorporating BDNF gene within gemini gene delivery carriers can highlight the capacity of this system to bring clinically significant changes, such as neuronal rescue and regeneration.

### **1.7.2. Hypothesis**

The **main** hypothesis of the current work is that 12-7NH-12 gemini-phospholipid NPs (GL-NPs) will effectively and safely deliver genes to the retina, following topical administration in a normal mouse model. A multi-stage optimization and development process will be carried out *in vitro* to maximize the capacity of GL-NP of overcoming the various barriers associated with the main goal. During this process, the following will be achieved:

- I. Efficient gene delivery in the rat retinal ganglion cell line (RGC-5), with minimal cytotoxic side effects. This will be accomplished by tailoring the physiochemical features, such as size and charge of GL-NPs for gene delivery in RGC-5 cells.
- II. Induction of neurite outgrowth in RGC-5 cells, following treatment with the optimized GL-NP, which carries the BDNF gene.
- III. Efficient corneal permeation in an *in vitro* model, following topical administration of the optimized GL-NPs.

### **1.7.3. Objectives of research**

Our endpoint objective of non-invasively delivering the BDNF gene to the retina will be achieved over several steps. In each of these steps, focus will be on improving one element of the gene delivery process. These steps include:

#### **A. NP preparation and characterization**

**(1) Preparation of several 12-7NH-12 GL-NP formulations, by controlled manipulation of several physical and chemical features that affect gene delivery, including:**

- (a) GL-NP charge ratio ( $\rho\pm$ ).
- (b) Composition of helper lipids.
- (c) Order of assembly of GL-NPs.
- (d) Manufacturing techniques.

**(2) Size and Zeta potential ( $\zeta$ ) characterization of the various GL-NP formulations.**

**B. Flow cytometry assessment of transfection efficiency of GL-NPs in RGC-5 cells.**

The transfection efficiency of the various GL-NPs in the RGC-5 cell line will be assessed by quantifying the pCMV-tdTomato reporter gene expression.

**C. Toxicity assessment of 12-7NH-12 GL-NP formulations in RGC-5 cells.**

A comprehensive viability assessment of RGC-5 cells, following various GL-NP treatments will be completed. The toxicity of the individual components of the GL-NP will be assessed in order to evaluate the contribution of each component to the overall toxicity.

**D. Evaluation of neurite outgrowth response in RGC-5 cells, following induction of BDNF gene expression by GL-NPs.**

**E. Assessment of permeation capacity and toxicity of optimized GL-NPs in a human corneal model, *in vitro*.**

A human corneal model will serve as an *in vitro* platform to assess GL-NP's corneal permeation capacity and ocular toxicity. The permeation capacity of GL-NPs will be assessed using confocal microscopy.

**F. Confocal microscopic assessment of gene delivery and biodistribution of GL-NPs in normal mice.**

Confocal imaging of gene delivery and biodistribution of optimized GL-NPs will be completed, following topical administration in a normal mouse model. Intravitreal injection will also be performed to compare the subsequent biodistribution and gene delivery patterns to that of topical administration.

## **2. Materials and methods**

### **2.1. Plasmid DNA**

Two plasmids were used for the experimental work: 1) pCMV6-AC-GFP (Origene technologies, Rockville, MD) and 2) pCMV-tdTomato (Clontech Laboratories Inc., Mountain View, CA).

#### **2.1.1. pCMV6-AC-GFP**

pCMV6-AC-GFP is a bicistronic plasmid (Figure 7), encoding the gene for the mouse BDNF protein as well as the reporter turbo green fluorescent protein (GFP). It is composed of 7.3 kbp. The coding region of transcript variant # 2 of the mus musculus BDNF cDNA clone (NM\_001048142), lacking the stop codon, was inserted into the Sgfl and Mlul sites of the pCMV6-AC-GFP vector to create a C-terminal turbo GFP fusion construct suitable for expression in mammalian cells. The coding region of the reporter gene, turbo GFP is located downstream of BDNF, so that the expression of turbo GFP is contingent on the expression of BDNF; additionally, it is flanked by the murine cytomegalovirus, CMV promoter. Turbo GFP is maximally excited at a 482 nm and has a maximum emission wavelength of 502 nm.

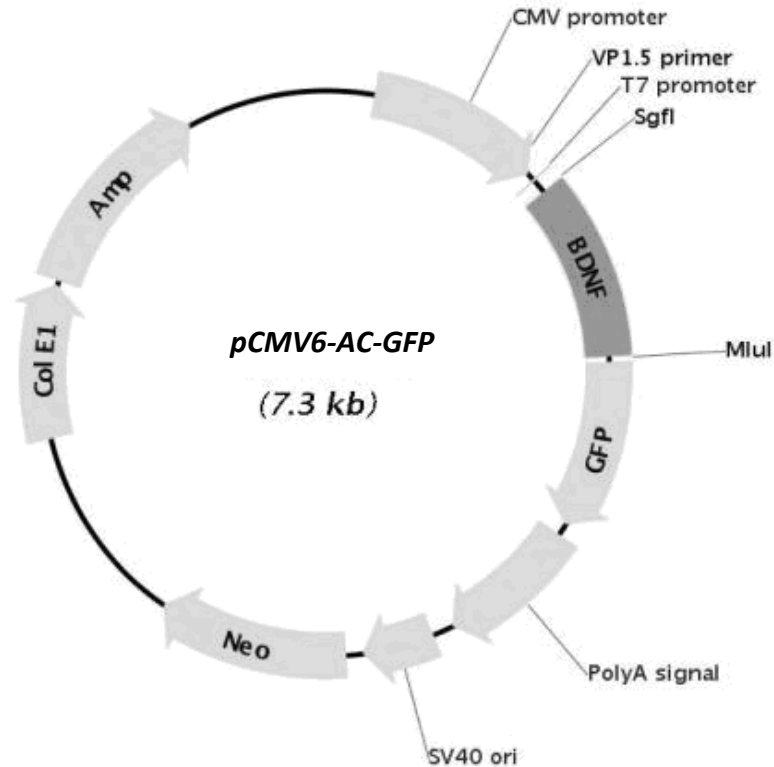


**Figure 7** The bicistronic plasmid, pCMV6-AC-GFP encodes the mus musculus BDNF gene. pCMV6-AC-GFP is 7.3 kbp and is tagged with turbo GFP for fluorescence analysis. It includes a CMV promoter for enhanced transcription efficiency.

### 2.1.2. pCMV-tdTomato

The pCMV-tdTomato plasmid encodes the reporter protein, tdTomato, a member of the fruit fluorescent proteins family and is composed of 5.4 kbp (Figure 8). The coding region of tdTomato is inserted in the NheI-NotI sites. It is also flanked by the CMV immediate early promoter,  $P_{CMV\ IE}$  (upstream), and the translation-enhancing sequence, Kozak (downstream). The tdTomato protein has excitation and emission maxima at 554 nm and 581 nm, respectively.

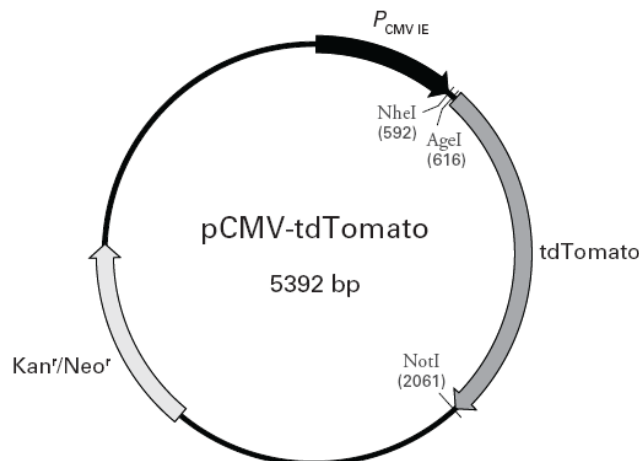


**Figure 8** The pCMV-tdTomato plasmid encodes the bright red fluorescent protein.

pCMV-tdTomato is a 5.4 kbp plasmid. It is equipped with the transcription enhancing promoter,  $P_{CMV IE}$ , as well as the translation enhancing sequence, Kozak, downstream of the reporter gene.

## 2.2. NP preparation

The 12-7NH-12 surfactant was synthesized in-house, from previous work done by our research group [106]. Several 12-7NH-12 NP compositions were prepared for systematic assessment of transfection efficiency in RGC-5 cells, over several stages of optimization. In each optimization step, one compositional parameter was modified, creating several NP types. Following transfection and particle characterization assessment, the NP with the best transfection efficiency was selected for the next stage of optimization. Four different parameters were manipulated in the optimization process:

1.  **$\rho_{\pm}$  charge ratio charge:** plasmid-gemini-DOPE (PGL<sub>DOPE</sub>) NPs were prepared at several positive:negative charge ratios ( $\rho_{\pm}$ ) using preparation Mode 1 (original). These NPs, which were developed in previous studies by our group, served as the starting point for the optimization process.



2. **Helper lipid composition:** the composition of the helper lipid vesicles was modified, by incorporating another helper lipid, 1,2-dipalmitoyl-sn-glycero-3-phosphocholine (DPPC), at various ratios, to create 3 different DOPE/DPPC, as well as DPPC lipid vesicles. The specific ratios will be shown in the next section.
3. **Order of assembly:** *Mode 1 (original):* pDNA was combined with the gemini surfactant first, to create pDNA-gemini complexes (PG). PG complexes were then combined with helper lipid vesicles (DOPE or DOPE/DPPC) to create PGL NPs. *Mode 2:* the gemini surfactant was combined with helper lipid vesicles to create gemini-lipid vesicles (GL); GL vesicles were then complexed with pDNA to create GL+P NPs.
4. **Manufacturing technique of helper lipid vesicles:** helper lipid vesicles were initially prepared by the thin film method. In later experimental stages, helper lipid vesicles were prepared by high-pressure homogenization, also known as microfluidization.

### 2.2.1. Preparation of thin film helper lipid vesicles

Two types of neutral lipids were used to prepare the helper lipid vesicles, DOPE (Avanti Polar Lipids, Alabaster, AL), and DPPC (Sigma-Aldrich Co., St. Louis, MO). In addition to DOPE vesicles, three different DOPE/DPPC helper lipid vesicles were prepared at the following DOPE:DPPC ratios: 75/25 (F2), 50/50 (F3), and 25/75 (F4). Finally, DPPC was used to prepare 100% DPPC vesicles (F5).

Lipids, in powder form, were dissolved in 99.5% (v/v) ethanol (Chem stores, Waterloo, ON) in a round bottom flask, along with 0.83 mg/mL  $\alpha$ -tocopherol, which is used as an anti-oxidant. Next, the mixture was sonicated for 5 minutes to thoroughly dissolve any lipid aggregates. Glass beads (approximately 5 g) were added to the lipid mixture to increase the

surface area of lipid dehydration. A Lipid film was created by solvent evaporation, using a rotary evaporator set at 100 rpm, and a 55°C water bath. Final traces of solvent were removed by freeze-drying the film overnight.

The lipid film was hydrated with a volume of 9.25% (w/v) aqueous sucrose solution (pH 9 for DOPE, and neutral pH for DOPE/DPPC) to obtain the desired 1 mM concentration, for 30 minutes, by placing the flask back onto the rotary evaporator. The set temperature of hydration was higher than the lipid's gel-liquid crystal transition temperature ( $T_m$ ) (DOPE  $T_m = -16^\circ\text{C}$ , DPPC  $T_m = 41^\circ\text{C}$ ). Accordingly, the DOPE film was hydrated at room temperature, while DPPC-containing films were hydrated at 55°C. After hydration, the flask was placed in a bath sonicator for 1-3 hours. During this process, aliquots of the lipid vesicles were collected to monitor the size of lipid vesicles. Once the desired vesicle size was reached (approximately 100 nm), sonication was terminated and the lipid formulation was filtered using 0.45  $\mu\text{m}$  cellulose acetate membrane filters (VWR International, Radnor, PA).

### **2.2.2. Mode 1 assembly of original PGL<sub>DOPE</sub> NPs**

This assembly method was carried out by creating PG complexes first, after which, they were combined with DOPE helper lipid vesicles. Typically, aqueous solutions of pDNA (type of pDNA depended on experiment), and 12-7NH-12 gemini surfactant were prepared separately at a concentration of 0.1  $\mu\text{g}/\mu\text{L}$  and 0.2  $\mu\text{g}/\mu\text{L}$ , respectively. The assembly process was carried out by mixing a fixed aliquot of plasmid solution with a calculated volume of gemini surfactant to achieve a certain  $p\pm$  charge ratio (Table 2). The PG mixture was left to incubate for 15 min at room temperature. Next, a calculated aliquot of 1 mM DOPE vesicles was added to the PG

complexes, at which point PGL<sub>DOPE</sub> NPs were allowed to self-assemble for 30 min, at room temperature.

**Table 2** A list of different PGL<sub>DOPE</sub> NPs prepared at a range of  $\rho_{\pm}$  charge ratios

$\rho_{\pm}$ Charge ratio	Gemini surfactant	pDNA	Helper lipid type	Type of PGL <sub>DOPE</sub> NP
5:1				5:1 $\rho_{\pm}$ PGL <sub>DOPE</sub>
7.5:1				7.5:1 $\rho_{\pm}$ PGL <sub>DOPE</sub>
10:1	12-7NH-12	td-	DOPE	10:1 $\rho_{\pm}$ PGL <sub>DOPE</sub>
12.5:1		Tomato	vesicles	12.5:1 $\rho_{\pm}$ PGL <sub>DOPE</sub>
15:1				15:1 $\rho_{\pm}$ PGL <sub>DOPE</sub>

### 2.2.3. Mode 1 preparation of PGL NPs with several helper lipid compositions

Based on the findings from the charge ratio screening, the PGL<sub>DOPE</sub> NP with optimal transfection efficiency (10:1  $\rho_{\pm}$ ) was selected for helper lipid optimization trials. DOPE/DPPC (F2-F4) and DPPC (F5) helper lipid vesicles were used to create four different 10: 1  $\rho_{\pm}$  PGL NPs, each with a different helper lipid composition (Table 3). These NPs were assembled using the original method outlined in the previous section.

**Table 3** A list of different PGL NPs, prepared using DOPE/DPPC and DPPC helper lipid vesicles

Formulation	Gemini surfactant	pDNA	DOPE:DPPC ratio		PGL complex
			DOPE	DPPC	
2			75%	25%	10: 1 $\rho_{\pm}$ PGL <sub>F2</sub>
3	12-7NH-12	td-Tomato	50%	50%	10: 1 $\rho_{\pm}$ PGL <sub>F3</sub>
4			25%	75%	10: 1 $\rho_{\pm}$ PGL <sub>F4</sub>
5			-	100%	10: 1 $\rho_{\pm}$ PGL <sub>F5</sub>

#### 2.2.4. Mode 2 assembly of GL+P NPs

Preparation of 10:1  $\rho_{\pm}$  GL+P NPs was carried out by creating GL vesicles, using the thin film method, followed by complexation of GL vesicles with pDNA. A calculated amount of 12-7NH-12 surfactant powder and lipid powder were weighed and processed as outlined in the thin film preparation method. Two types of GL vesicles were created, using DOPE and the optimized DOPE/DPPC helper lipid vesicles (F4), to create GL<sub>DOPE</sub> and GL<sub>F4</sub> vesicles. GL vesicles were complexed with pDNA for thirty minutes before use.

#### 2.2.5. PGL NPs with microfluidized helper lipid vesicles

Based on the results of the order of assembly optimization, Mode 1 assembly was selected for further NP optimization trials. Two types of 10: 1  $\rho_{\pm}$  NPs were prepared with

microfluidized lipid vesicles ( $PGL_{MF}$ ); the first with microfluidized DOPE vesicles ( $PGL_{MF-DOPE}$ ) and the second with microfluidized F4 vesicles ( $PGL_{MF-F4}$ ).

To prepare microfluidized helper lipid vesicles, a calculated amount of lipid powder was weighed and added to an aliquot of 9.25% (w/v) aqueous sucrose solution (pH 9 for DOPE, and pH 7 for DOPE/DPPC), yielding 1mM final lipid concentration. The mixture was sonicated for 10 minutes to dissociate large lipid aggregates. Next, the LV1 microfluidizer (Microfluidics Corporation, Newton, MA) was primed with 2 mL of sucrose solution at the appropriate pH. Using a glass syringe, the lipid mixture was loaded into the loading chamber of the microfluidizer and passed twice through the 87  $\mu\text{m}$  wide pores of the Y-type interaction chamber at 20,000 psi. Microfluidized lipid vesicles were then filtered, using 0.45 $\mu\text{m}$  cellulose acetate membrane filter, and allowed to complex with 10: 1  $\rho\pm$  PG complexes for 30 minutes. A summary of all prepared NPs is provided in Table 4.

**Table 4** Nomenclature explained: a list of all the NPs used over the optimization process, and the different components of each NP. (P) pDNA; (G) 12-7NH-12 gemini surfactant (L) Helper lipid vesicles; MF microfluidized

Category of NP	Preparation steps		Type of helper lipid (L)		Method of vesicles preparation	Name of NP
	Step 1	Step 2	% DOPE	% DPPC		
<b>Original PGL<sub>DOPE</sub> NPs at different <math>\rho\pm</math> charge ratios</b>	Create (PG) complexes	Add (L) vesicles	100	0	Thin film	PGL <sub>DOPE</sub>
Selected optimization condition: <b>10:1 <math>\rho\pm</math></b> Next parameter change: Helper lipid composition ( DOPE $\rightarrow$ DOPE/DPPC)						
<b>10:1 <math>\rho\pm</math> PGL NP<sub>s</sub> with DOPE/DPPC helper lipid vesicles</b>	Create (PG) complexes	Add (L) vesicles	75	25	Thin film	PGL <sub>F2</sub>
			50	50		PGL <sub>F3</sub>
			25	75		PGL <sub>F4</sub>
			100	0		PGL <sub>F5</sub>
Selected optimization conditions: <b>100% DOPE, 25% DOPE-75% DPPC (F4)</b> Next Parameter change: Order of assembly ( Mode 1 PGL $\rightarrow$ Mode 2 GL+P )						
<b>GL+P NPs prepared using Mode 2 assembly method</b>	Create (GL) vesicles	Add pDNA	100	0	Thin film	GL <sub>DOPE</sub> +P
			25	75		GL <sub>F4</sub> +P
Selected optimization condition: <b>Mode 1 (original)</b> assembly method. Next Parameter change: Manufacturing technique of vesicles ( Thin film $\rightarrow$ Microfluidization)						
<b>PGL NPs with microfluidized helper lipid vesicles</b>	Create (PG) complexes	Add (L) vesicles	100	0	Thin film	PGL <sub>MF-DOPE</sub>
			25	75		PGL <sub>MF-F4</sub>

### **2.3. Assessment of particle size, polydispersity and zeta ( $\zeta$ ) potential**

Size (hydrodynamic diameter), polydispersity and  $\zeta$  potential measurements were carried out on: i) lipid vesicles, ii) PG complexes, iii) PGL NPs, iv) GL vesicles and v) GL+P NPs, prepared with the two manufacturing techniques. Aliquots of 100  $\mu$ L and 1000  $\mu$ L of each formulation were prepared for size and  $\zeta$  potential measurements, respectively. Measurements were performed using the Nano ZS Zetasizer (Malvern Instruments, Worcestershire, UK), which employs dynamic light scattering (DLS) as a principal technique for measuring the hydrodynamic size of molecules. Measurements were carried out in triplicates for each condition. Z-average size values are considered valid for samples with a PDI index < 0.5 (according to manufacturer's protocol).

### **2.4. Transfection assay**

#### **2.4.1. 2.4.1 Cell culture and dose application**

One day before dosing, RGC-5 cells were seeded in a 6-well cell culture plate (BD, Franklin Lakes, NJ) at a density of 200,000 per well to achieve a confluency of 60-70% on the day of dosing. Three wells were assigned for transfection assessment of each NP formulation. RGC-5 cells were seeded in Dulbecco's Modified Eagles Medium (DMEM), low glucose with L-glutamine (Thermo scientific, Waltham, MA), supplemented with 10% fetal bovine serum (FBS) (Sigma-Aldrich Co., St. Louis, MO) only. One hour before dosing, the supplemented media was replaced with serum-free DMEM.

Preparation of each NP type was carried out as described in the NP preparation section. The amount of pCMV-tdTomato or pCMV6-AC-GF plasmid used in all transfection trials was 0.5

µg per well. The commercially available Lipofectamine™ Plus reagent (Invitrogen, Grand Island, NY) was used as a positive control for transfection efficiency analysis. A Lipofectamine dose was prepared by combining pDNA, diluted in 25 µL of non-supplemented DMEM media with 4 µL of Plus™ reagent. After a 15 minute incubation period at room temperature, the complexed Plus™ reagent was combined with 1 µL of Lipofectamine™ reagent, diluted in 25 µL of non-supplemented media. The two mixtures were incubated for 15 minutes at room temperature, before application. All prepared doses were mixed with 1.5 mL of non-supplemented DMEM media, and added to the RGC-5 cells after changing the culturing media. Doses were left on cells for 12 hours before transfection and viability analysis.

#### **2.4.2. Cell harvesting**

Twelve hours after dose application, the treatment media was removed from the wells, and cells were gently washed with Dulbecco's phosphate buffered saline (DPBS) with calcium and magnesium (Thermo scientific, Waltham, MA). Cells were then harvested using 0.25% Trypsin + 0.2 g/L EDTA solution (Thermo scientific, Waltham, MA). Collected cells were centrifuged at 460 g for 5 minutes, and the supernatant was removed. The pellet was centrifuged and resuspended in fresh DPBS twice. Cells were then counted using the Countess cell counter (Invitrogen, Grand Island, NY). After counting the cells, they were centrifuged for 5 minutes, their supernatant was removed, and they were resuspended in an appropriate cell buffer volume to yield a final concentration of  $2.5 \times 10^6$  cells/mL.



### **2.4.3. Fluorescence set up of flow cytometry analysis**

The transfection efficiency and toxicity of the various prepared NPs were assessed using on-chip flow cytometry analysis, using the Agilent Bioanalyzer (Agilent Technologies, Santa Clara, CA). The Bioanalyzer has a blue and red spectrum laser/detector module. Each module has a fixed excitation and detection wavelength and is used to assess one distinct biological characteristic; either transfection or viability. Accordingly, these two modules were used to simultaneously to measure two parameters, following transfection: 1) transfection efficiency and 2) viability of RGC-5 cells. Assessment of NP transfection efficiency was undertaken by measuring fluorescence associated with the reporter gene expression. Viability assessment of transfected cells was completed by measuring the viability fluorescence, following treatment with a viability dye (shown below). A transfection efficiency value was calculated based on the percentage of viable cells that exhibited a supra-threshold transfection signal. The threshold value was determined based on the natural fluorescence of untreated cells.

Two fluorophore pairs were initially used to assess transfection efficiency and viability in pilot stages (Table 5). The pairs were selected in accordance with the Bioanalyzer's optical specifications. The pair which demonstrated better sensitivity was selected to complete the entire transfection assessment. The first pair consists of the reporter gene turbo GFP (in pCMV6-AC-GFP) and the viability stain, Carboxynaphthofluorescein (CBNF) (Invitrogen, Grand Island, NY). The second pair consists of the reporter gene tdTomato (in pCMV-tdTomato) and the viability stain, calcein (Invitrogen, Grand Island, NY).

**Table 5** A list of the fluorophore pairs used in parallel transfection and viability assessment

For each pair, the excitation and emission properties are outlined along with the respective laser/detector module assigned for each measured parameter.

<b>Fluorophore</b>	<b>Assay</b>	<b>Excitation <math>\lambda</math> (nm)</b>	<b>Emission <math>\lambda</math> (nm)</b>	<b>Excitation Laser</b>
Pair 1 : GFP/CBNF				
GFP	Transfection	482	502	Blue
CBNF	Viability	595	675	Red
Pair 2: tdTomato/Calcein				
tdTomato	Transfection	554	581	Red
Calcein	Viability	494	514	Blue

For each flow cytometry run, a microfluidic chip was prepared for cell loading using the cell kit for fluorescently stained cells (Agilent Technologies, Santa Clara, CA); 25,000 cells from each sample were loaded in each sample well. On-chip viability staining and chip preparation was performed according to the manufacturer's protocol.

## **2.5. Confocal microscopic assessment of transfection efficiency**

The confocal laser scanning microscope LSM 710 (Carl Zeiss, Oberkochen, Germany) was used in the initial stages of transfection optimization to gain a qualitative measure of the transfection capacity of PGL NPs. The transfection procedure followed was identical to the one outlined in the previous sections (2.4.1-2.4.3), with one exception: cells were cultured in glass-bottom 35 mm cell culture dishes (Greiner bio-one, GmbH, Germany). RGC-5 cells that were transfected with GFP, and stained with the CBNF viability dye were imaged using a 488 nm and 647 nm laser, simultaneously.

## **2.6. Assessment of NP's toxicity in RGC-5 cells**

The viability reagent PrestoBlue™ (Invitrogen, Grand Island, NY) was used to assess the toxicities of various NPs, vesicles, and complexes used in the particle characterization stage. PrestoBlue™ is a resazurin-based, cell permeable solution that gauges cell viability as a function of cells' metabolic conversion of resazurin to resorufin, a red fluorescent molecule [107]. This study investigated the toxicity of 1) the 12-7NH-12 gemini surfactant at different concentrations, 2) PG complexes at all tested  $\rho_{\pm}$  charge ratios, 3) PGL NPs prepared at all tested  $\rho_{\pm}$  charge ratios and with 5 different lipid formulations, 4) and all five individual lipid formulations.

The day before dose application, 7,500 RGC-5 cells were plated in each well of an opaque-walled 96-well plate (Corning Incorporated, Corning, NY). Three wells were assigned for each screened formulation. Formulations were prepared as described in the NP preparation section (Section 2.2), after which they were mixed with a volume of serum-free media to yield a

200  $\mu$ L final well volume. The resulting concentration is equivalent to that used in transfection assessment. Doses were left for 12 hours, after which, 20  $\mu$ L of the PrestoBlue™ reagent was directly added to each well, followed by an hour incubation period at 37°C. Viability fluorescence was measured using the SpectraMax M5 plate reader (Molecular Devices, Sunnyvale, CA), at 560 nm and 590 nm excitation and emission wavelengths, respectively.

## **2.7. Assessing neurite outgrowth in RGC-5 cells following NTF expression**

Neurite extension in RGC-5 cells was assessed, following treatment with two optimized PGL NPs and Lipofectamine Plus. The human recombinant BDNF (hrBDNF) protein (Origene Technologies, Rockville, MD) was used as a control.

### **2.7.1. Cell culture and dose preparation**

The day before the experiment, a 24-well, glass-bottom cell culture plate (Greiner bio-one, GmbH, Germany) was seeded with  $1 \times 10^4$  RGC-5 cells per well, in 10% FBS-supplemented DMEM. The day of the treatment, dishes were visually inspected to ensure that the plate's confluency was consistent across all wells, and that it is below 50%. Six different treatments were applied to the RGC-5 cells, each in triplicate. The first three treatments included the optimized 10:1  $\rho_{\pm}$  PGL<sub>DOPE</sub>, 10:1, and  $\rho_{\pm}$  PGL<sub>F4</sub> NPs, as well as Lipofectamine lipoplexes, each carrying 0.1  $\mu$ g of the pCMV6-AC-GF plasmid, which encodes for the BDNF gene. As a comparative control, we used direct stimulation of RGC-5 cells with BDNF protein. In this case, hrBDNF protein, variant #6 (NP\_733930) was prepared at the following three concentrations in 1.5 mL of serum-free DMEM: 50 ng/mL, 100 ng/mL and 200 ng/mL. One set of cells was left untreated, to be used as negative control. Shortly before dose application, the

supplemented media was removed from the dishes, and replaced with serum-free DMEM media. Twelve hours after treatment applications, treatment media was exchanged with fresh 10% FBS-supplemented DMEM and allowed to incubate for another 12 hours.

At the end of the incubation period, media was removed from the dishes, and cells were rinsed with Dulbecco's Phosphate-Buffered Saline (DPBS) (Thermo scientific, Waltham, MA). Next, cells were fixed with a 10% formaldehyde solution in DPBS, for 2 hours. Cells were then rinsed with DPBS (2 x 5 minutes), and treated with a blocking/permeabilization solution, composed of 5% bovine serum albumin (Sigma-Aldrich Co., St. Louis, MO) and 0.2% Triton X solution (Sigma-Aldrich Co., St. Louis, MO), in DPBS. After an hour of incubation at room temperature, the blocking/permeabilization solution was removed, and cells were rinsed with DPBS (2x 5 minutes). A  $2.5 \times 10^{-2}$   $\mu\text{g}/\mu\text{L}$  solution of the Anti- $\beta$  III Tubulin Monoclonal Antibody (TU-20 clone), conjugated with fluorescein isothiocyanate (FITC) (Thermo scientific, Waltham, MA), was prepared in DPBS to immunostain RGC-5 cells. An aliquot of 200  $\mu\text{L}$  of the antibody solution was applied to the glass slip of each plate, and was left to incubate for 8 hours at room temperature [108].

Immunostained cells were visualized using confocal microscopy, at an excitation wavelength of 495 nm and an emission wavelength of 525 nm (FITC maxima). Six images were captured (100 X magnification) from random locations of each dish, in areas of similar cell densities. Each image (containing approximately 250 cells) was quantified in terms of average neurite length. The selection criteria for neurite length quantification included free neurites, which are not in contact with adjacent cells, in addition to neurites that are in contact with non-adjacent cells. Neurites that were extended to immediately adjacent cells were excluded. This is

because the length of this category of neurites is influenced by confluency and not by the applied treatment. Neurite length quantification was completed using the NeuronJ function of the image processing software, ImageJ. Average and a standard deviation value, for each triplicate measurement was obtained in each treatment condition.

## **2.8. Assessment of permeation, and irritation of 12-7NH- 12 NPs in a human corneal epithelial model**

The EpiOcular Corneal model (MatTek Corporation, Ashland, MA) was used as a platform for assessing the degree of permeation and toxicity of PGL NPs in the cornea. This 3-D model is a multi-layered tissue composed of stratified, squamous epithelium equivalent to that found in the cornea. It is originally derived from human epidermal keratinocytes that have been differentiated to form a cornea-like structure [109]. Below are two histological sections of the Mattek EpiOcular human corneal model (Figure 9-A) and a human cornea (Figure 9-B). The structure of the corneal model used in this experiment correlated closely to that of the rabbit cornea, which is used in the standard Draize test.

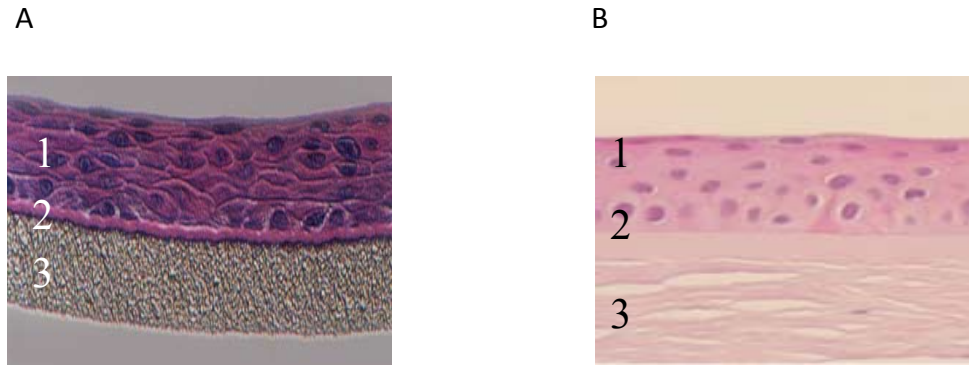


**Figure 9** **Mattek EpiOcular HCE model compared to human cornea**  
 Histological sections of the A) Mattek EpiOcular human corneal model (Mattek corporation) and B) human cornea. The sections show the main corneal layers, including the 1) epithelium, 2) Bowman's membrane, and 3-A) HCE's microporous support membrane, 3-B) stroma. The EpiOcular model closely resembles the structural organization of the rabbit cornea. *Figure 9-B adopted from Ehlers et al, 2010 [110].*

### 2.8.1. Cy5 labeling of pDNA for pDNA biodistribution assessment

The pDNA used in this experiment (pCMV6-GFP) was tagged with the nucleic acid labeling reagent, Cy5 (Mirus Bio LLC., Madison, WI), to allow for monitoring of pDNA biodistribution within the HCE tissue, following administration. Cy5 is a cyanin-based labeling dye, which has a maximum excitation wavelength of 649 nm and emission wavelength of 670 nm. The labeling procedure was carried out according to manufacturer's protocol. Briefly, the labeling reagent was incubated with the pDNA at a ratio of 0.5:1 ( $v_{\text{dye}}: w_{\text{DNA}}$ ) for 1 hour at 37°C. The pDNA was precipitated from the mixture by adding 0.1 volumes of 5 M sodium chloride and 2 volumes of ice cold 100% ethanol to the reaction mixture. Following a 30-minute precipitation period, recovery of the pDNA was achieved by centrifugation of the reaction mixture, pellet washing using 70% ethanol, and resuspension of pDNA in the supplied labeling buffer. The concentration of pDNA was verified using the Nanodrop 2000c spectrophotometer (Thermo scientific, Waltham, MA).

### 2.8.2. PGL<sub>DOPE</sub> NPs preparation for corneal permeation assessment

The optimized 10:1  $\rho_{\pm}$  PGL<sub>DOPE</sub> NPs were prepared, using 2.5  $\mu\text{g}$  of Cy5-labeled pCMV6-AC-GFP plasmid per treatment. DOPE helper lipid vesicles were prepared, using the thin film method, at a concentration of 10 mM, to meet the dose volume restriction (50  $\mu\text{L}$ ). Two vehicle controls were used: thin film GL vesicles (no pDNA) and microfluidized GL vesicles. Both GL vesicles were prepared using DOPE and the fluorescent lipid, 1,2-dipalmitoyl-sn-glycero-3-phosphoethanolamine-N-(7-nitro-2-1,3-benzoxadiazol-4-yl) (NBD-PE) (Avanti Polar Lipids, Alabaster, AL), to allow for tracking of vesicles post administration. Particle size assessment for microfluidized GL vesicles was carried out as previously described (Section 2.1). Two tissue inserts were assigned for dosing with 10:1 PGL<sub>DOPE</sub> NPs, while one insert was assigned for each GL vesicle dose. NBD-PE has an excitation and emission maxima of 466 nm and 539 nm, respectively.

Two days before dose application, HCE tissue inserts were equilibrated in their provided growth media at 37°C, according to manufacturer's protocol. To apply a dose, formulations were applied by gently dispensing the prepared formulation directly to the surface of the HCE tissue, using a micropipette. Two hours after dose application, HCE tissue inserts were carefully excised from their plastic insert, and washed with sterile water. Following an extensive rinse, the tissue was transferred to a glass-bottom 6-well plate (MatTek Corporation, Ashland, MA), and visualized using the CLSM 710. Permeation of NPs was monitored by tracking of Cy5, and NBD-PE fluorescence. Subsequent imaging was undertaken every 2 hours, for at least 15 hours. After each imaging session, the tissue was returned to its well and allowed to incubate in media, at 37°C in the CO<sub>2</sub> incubator. Tissue staining was carried out, at the last time point, for



HCE tissue treated with control GL vesicles, using DRAQ5 (excitation at 647 nm, emission at 670 nm) (BioStatus Limited, Leicestershire, UK).

### **2.8.3. Assessing corneal toxicity of NPs**

The toxicity screening was performed following HCE tissue treatment with three NPs, including 10:1  $\rho_{\pm}$ , 20:1 PGL<sub>DOPE</sub>, as well as 10:1  $\rho_{\pm}$  PGL<sub>MF-DOPE</sub> NPs. The 20:1 PGL<sub>DOPE</sub> NPs were used in this assay to highlight the effect of  $\rho_{\pm}$  charge ratio on corneal toxicity. On the other hand, 10:1  $\rho_{\pm}$  PGL<sub>MF-DOPE</sub> NPs were used to investigate the effect of the manufacturing process of helper lipid vesicles on corneal toxicity. The 3-[4,5-dimethylthiazol-2-yl]-2,5-diphenyl tetrazolium bromide (MTT) toxicological screening reagent (Sigma-Aldrich Co., St. Louis, MO) was used to assess the NP-induced toxicity, according to the manufacturer's protocol. A negative control (no treatment) was used as baseline condition. Three commonly used surfactants, were used as positive controls, including: 1 % v/v Benzalkonium chloride, 1% w/v Sodium dodecyl sulfate (SDS) and 1% w/w Tween 80 (Sigma-Aldrich Co., St. Louis, MO). All treatments, were applied in duplicates, except the positive controls (1 treatment each, due to a set number of inserts), and were incubated for 24 hours before analysis.

At the end of the incubation period, tissue inserts were thoroughly rinsed with sterile water and transferred to a 24-well plate, containing the MTT reagent. The plate was then incubated for 3 hours in a 37°C CO<sub>2</sub> incubator. Next, HCE inserts were removed from the 24-well plate, and transferred to a new 24-well plate, containing 2mL of isopropanol in each well, so that isopropanol is immersing the surface of the tissue insert. The plate was then placed on an orbital plate shaker (at 30 rpm) for 3 hours, at room temperature. At the end of this extraction period, the tissue was pierced with a needle, and the liquid within each insert was

decanted into the well from which it was taken. The extracted solution was then mixed, and two 200 $\mu$ L aliquots were transferred from each well into an appropriately labeled 96-well plate. Absorbance values were obtained for each well, at 570 nm, and were used to calculate viability values, which were normalized to the no-treatment condition.

## **2.9. Pilot *in vivo* evaluation of biodistribution and transfection efficiency of NPs in mice eyes**

This experiment was completed in collaboration with Dr. Jeremy Sivak, at the Toronto Western Research Institute, Vision Science Research Program, of the University Health network. The purpose of this experiment was to investigate the biodistribution patterns and transfection efficiency of 10:1 PGL<sub>DOPE</sub> NPs, following topical and intravitreal administration in C57BL/6N mice.

### **2.9.1. Animals and *in vivo* experimental design**

Ten 4-week old male C57BL/6N mice (Taconic Hudson, NY) were randomly assigned to four experimental groups: I) topically administered NPs for transfection assessment (3 animals) II) intravitreally injected NPs for transfection assessment (3 animals) III) intravitreally and topically administered fluorescent NPs for short term biodistribution assessment (1 animal each), IV) intravitreally injected Cy5 labeled pCMV6-GFP (1 animal), and V) negative control (no treatment) (1 animal).

### **2.9.2. PGL NPs preparation for transfection assessment**

For assessment of transfection following topical and intravitreal administration, 10:1 PGL<sub>DOPE</sub> NPs were prepared with DOPE helper lipid vesicles. Doses were prepared such that

topical and intravitreal doses contained 1  $\mu\text{g}$  and 0.1  $\mu\text{g}$  of Cy5 labeled pCMV6-GFP plasmid, respectively. Lipid vesicles were concentrated using centrifugal filter units, with a 30 kDa pore size (EMD Millipore, Billerica, MA), to minimize the final dose volume. *In vivo* dose volumes for topical and intravitreal administration were 5  $\mu\text{L}$  and 2  $\mu\text{L}$ , respectively. To assess short-term biodistribution, 10:1 PGL NPs were assembled with DOPE helper vesicles, containing 10% of the fluorescent lipid, NBD-PE. These NPs were prepared to track potential NP dissociation from pDNA, and will be referred to as 10:1 PGL<sub>DOPE-N</sub>. Control doses included blank GL vesicles (without pDNA), and Cy5 labeled pDNA.

### **2.9.3. Experimental design**

Three animals received a topical dose of 10:1 PGL<sub>DOPE</sub> NPs in each left eye; in their right eyes, two mice received blank GL vesicles, while the third animal's eye was left untreated. The same administration pattern was followed for administration of three mice that received intravitreal doses of the 10:1 PGL<sub>DOPE</sub> NPs. For short-term biodistribution assessment, one animal received a topical dose of 10:1 PGL<sub>DOPE-N</sub> NPs in one eye (second eye was left untreated), while another animal received an intravitreal dose of PGL<sub>DOPE-N</sub> NPs in one eye (second eye was left untreated). An additional mouse received an intravitreal injection of 0.1  $\mu\text{g}$  of Cy5 labeled pDNA in one eye (second eye untreated). A summary of the animal assignment to group conditions is provided in Table 6.

**Table 6** Experimental design of *in vivo* experiment, and assignment of animals to the various conditions

Condition/ Number of animals	Left Eye treatment	Right eye treatment
Topical Administration N = 3 animals	10:1 PGL <sub>DOPE</sub>	GL vesicles
	10:1 PGL <sub>DOPE</sub>	GL vesicles
	10:1 PGL <sub>DOPE</sub>	No treatment
Intravitreal Injection N = 3 animals	10:1 PGL <sub>DOPE</sub>	GL vesicles
	10:1 PGL <sub>DOPE</sub>	GL vesicles
	10:1 PGL <sub>DOPE</sub>	No treatment
Short term topical NP N = 1 animal	10:1 PGL <sub>DOPE-N</sub>	No treatment
Short term intravitreal NP N = 1 animal	10:1 PGL <sub>DOPE-N</sub>	No treatment
Long term Intravitreal pDNA N = 1 animal	Cy5 labeled pCMV6-AC-GFP	No treatment
Naïve eyes N= 1 animal	No treatment	No treatment

#### **2.9.4. Topical and intravitreal administration**

To administer intravitreal doses (Figure 11-A), mice were anaesthetized by intraperitoneal injection with ketamine/xylazine mixture in sterile PBS, at a final concentration of 10 mg/mL, and 1 mg/mL, respectively. Prior to the intravitreal injection, one drop of the mydriatic agent, Cyclogyl (1 % Cyclopentolate Hydrochloride) was administered to each eye, followed by one drop of the local anesthetic, Alcaine (0.5% Proparacaine Hydrochloride). After five minutes, mice were positioned for injection under a standard stereomicroscope (Zeiss, Oberkochen, Germany). A 30 gauge needle was used to pierce an opening 2 mm posterior to the limbus, through which an injection can be administered. The 2  $\mu$ L intravitreal dose was delivered using a 33 gauge, 0.5 inch blunt-end needle and a glass microsyringe (Hamilton, Reno, NV). After injection, a drop of Optimyxin antibiotic (Sandoz, QC, Canada) was applied to each eye. Initial topical administrations (Figure 11-B) were done following anesthetizing animals as previously described. Topical doses were administered twice times, 2 hours apart, by gently dispensing the 5  $\mu$ L dose onto the cornea, using a 10  $\mu$ L micropipette.

**A**



**B**

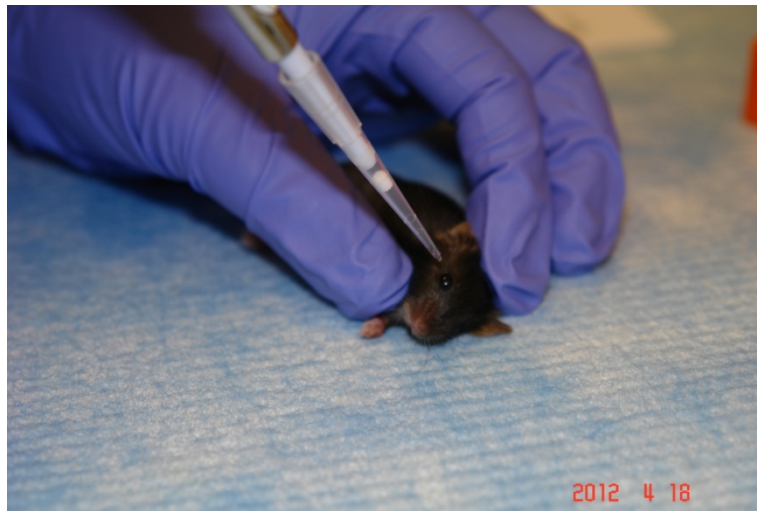


**Figure 10 Intravitreal (A) and topical (B) administration of NPs in 4-week old male C57BL/6N mice**

Topical administration was carried out twice, 2 hours apart, while intravitreal injection was performed once. Topical (5  $\mu\text{L}$ ) and intravitreal (2  $\mu\text{L}$ ) doses of PGL<sub>DOPE</sub> NPs contained 1  $\mu\text{g}$  and 0.1  $\mu\text{g}$  of Cy5 labeled pDNA, respectively. Animals treated for transfection assessment were sacrificed 48 hours after treatment, while those who were treated for short-term biodistribution, were sacrificed 4 hours after treatment.

## **2.10. Tissue collection**

All animals were sacrificed 48 hours after dose application, except for animals in the short-term biodistribution assessment group; those were sacrificed 4 hours after dose application. Animals were euthanized by cervical dislocation, after they were anesthetized. Eyes of euthanized animals were surgically removed and fixed in 4% paraformaldehyde solution in sterile PBS overnight at 4°C. The following day, eyes were removed from the fixative solution, washed with PBS, and placed in 30% w/v sucrose solution in PBS overnight at 4°C. Eyes were then embedded in molds containing optimal cutting temperature (OCT) mounting media (Thermo scientific, Waltham, MA), ensuring positioning in the right orientation for cross sectional tissue cryo-sectioning. Molds were snap frozen on dry ice, and stored at -80°C until they were sectioned. Sectioning was carried out using a CM3050 cryostat, set at - 20°C (Leica Biosystems, Concord, ON). Eyes were sectioned at a thickness of 80 µm and placed on glass slides for imaging. Sections were imaged using CLSM, at the appropriate excitation and emission wavelengths for GFP, Cy-5 and NBD-PE, which were previously mentioned. Sections that did not shown GFP expression were stained with the Wheat Germ Agglutinin (WGA), Alexa Fluor® 488 Conjugate dye (Invitrogen, Grand Island, NY), for tissue visualization. WGA has an excitation and emission wavelengths of 495nm and 519nm, respectively.

## **2.11. Statistical analysis**

Statistical analysis was undertaken using one-way ANOVA comparison test(in SPSS). Post-test analysis was performed using Tukey's multiple comparison. Significance of difference in groups' means was established based on a  $p < 0.05$  certainty limit.

### 3. Results

#### 3.1. Particle characterization of 12-NH-12 NPs

Particle characterization for each tested formulation is presented in terms of their particle size, polydispersity index (PDI), and  $\zeta$  potential.

##### 3.1.1. PG complexes and PGL<sub>DOPE</sub> NPs of various $\rho_{\pm}$ charge ratios

Table 7 lists size and PDI measurements of PG complexes and PGL<sub>DOPE</sub> NPs, prepared at several  $\rho_{\pm}$  charge ratios. Sizes of PG complexes, at all tested charge ratios, fall within an approximate size range of 500-1000 nm. These measurements indicate that the initial complexation of pDNA with the 12-7NH-12 gemini surfactant results in the formation of relatively large aggregates. The data does not suggest any correlation between the  $\rho_{\pm}$  charge ratio of PG complexes and their respective sizes. The addition of the DOPE vesicles to PG complexes produces significantly smaller PGL<sub>DOPE</sub> NPs in all tested  $\rho_{\pm}$  charge ratio (Table 7). The compacted PGL<sub>DOPE</sub> NP sizes range between  $158.7 \pm 4.7$  to  $220.1 \pm 7.0$  nm.



**Table 7** Size and PDI measurements of PG complexes and PGL NPs of various  $\rho_{\pm}$  charge ratio

$\rho_{\pm}$ charge ratio	Measurement	PG Complexes (n = 3)	PGL NPs (n = 3)
5:1	Size (nm) $\pm$ SD	692.8 $\pm$ 57.6	220.1 $\pm$ 7.0
	PDI $\pm$ SD	0.35 $\pm$ 0.06	0.40 $\pm$ 0.01
7.5:1	Size (nm) $\pm$ SD	968.5 $\pm$ 45.8	202.5 $\pm$ 6.5
	PDI $\pm$ SD	0.25 $\pm$ 0.02	0.38 $\pm$ 0.01
10:1	Size (nm) $\pm$ SD	590 $\pm$ 28.8	166.7 $\pm$ 5.7
	PDI $\pm$ SD	0.45 $\pm$ 0.03	0.42 $\pm$ 0.04
12.5:1	Size (nm) $\pm$ SD	693.8 $\pm$ 52.6	167.1 $\pm$ 7.4
	PDI $\pm$ SD	0.47 $\pm$ 0.09	0.41 $\pm$ 0.07
15:1	Size (nm) $\pm$ SD	534.4 $\pm$ 16.3	158.7 $\pm$ 4.7
	PDI $\pm$ SD	0.41 $\pm$ 0.01	0.38 $\pm$ 0.04

Table 7 additionally shows a negative correlation between the  $\rho_{\pm}$  charge ratio of PGL<sub>DOPE</sub> NPs and their respective sizes. This effect is reproduced in Figure 11, where increasing the  $\rho_{\pm}$  charge ratio of PGL<sub>DOPE</sub> NPs is shown to decrease the NP size. For example, increasing the charge ratio of PGL<sub>DOPE</sub> NPs, over the 5:1 - 10:1  $\rho_{\pm}$  charge ratio range, led to a decrease in their size, by approximately 50 nm. Mean PDIs of PG complexes and PGL<sub>DOPE</sub> NPs are below 0.5, indicating validity of the normal distribution assumption for the calculation of particle size z-average. Generally, since PGL<sub>DOPE</sub> NP PDI values are only marginally lower than 0.5, they are considered to have a relatively heterogeneous size distribution. Typically, a PDI value above 0.2 indicates a heterogeneous particle size distribution.

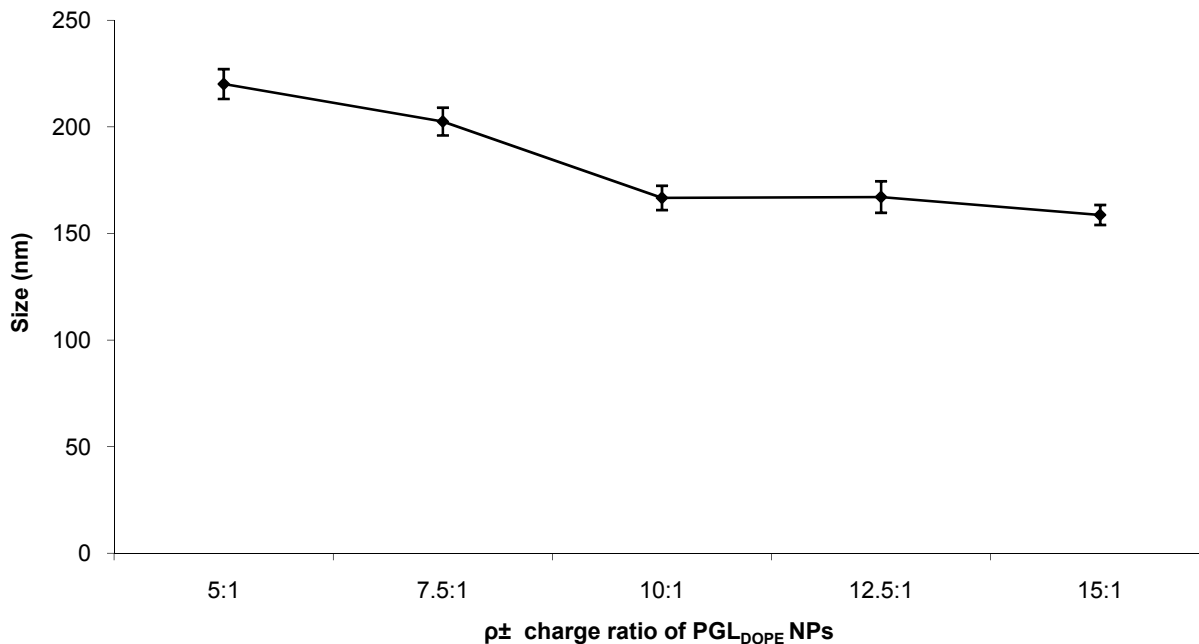


**Figure 11 Relationship between  $\rho_{\pm}$  charge ratio and final PGL<sub>DOPE</sub> NP size**

Increasing the  $\rho_{\pm}$  charge ratio of PGL NPs is associated with a decrease in their sizes, as demonstrated by the 50 nm size decrease of the 5:1 – 10:1  $\rho_{\pm}$  charge ratio range. Further increase in the  $\rho_{\pm}$  charge ratio of PGL<sub>DOPE</sub> NPs did not result in further compaction.

Table 8 compares the  $\zeta$  potential values of PG complexes to those of PGL<sub>DOPE</sub> NPs. Generally, colloidal suspensions with  $+30 \text{ mV} < \zeta < -30 \text{ mV}$  are considered stable [111], with no aggregation or precipitation risk. Table 8 also shows a positive relationship between the  $\rho_{\pm}$  charge ratios of PG complexes and their corresponding  $\zeta$  potential values. However, PG complexes, at all tested  $\rho_{\pm}$  charge ratios, do not meet the  $\zeta$  potential colloidal stability threshold of  $\pm 30 \text{ mV}$ . This indicates that the colloidal stability of PG complexes alone is low, and that the potential for aggregation and sedimentation is relatively high. The addition of DOPE helper lipid vesicles to PG complexes produces NPs with  $\zeta > +30 \text{ mV}$  in all charge ratio conditions, significantly improving colloidal stability.

**Table 8**  $\zeta$  potential measurements of PG complexes and PGL NPs of various  $\rho_{\pm}$  charge ratio

$\rho_{\pm}$ of formulation	<i>Mean <math>\zeta</math> potential (mV) <math>\pm</math> SD</i>	
	PG complexes (n=3)	PGL NPs (n=3)
<b>5:1</b>	+ 3.7 $\pm$ 1.5	+ 41.7 $\pm$ 3.0
<b>7.5:1</b>	+ 9.7 $\pm$ 3.9	+ 48.7 $\pm$ 2.2
<b>10:1</b>	+ 13.2 $\pm$ 3.0	+ 41.9 $\pm$ 2.5
<b>12.5:1</b>	+ 14.8 $\pm$ 3.0	+ 38.6 $\pm$ 0.8
<b>15:1</b>	+ 18.7 $\pm$ 0.4	+ 36.2 $\pm$ 2.5

### 3.1.2. PGL NPs assembled with different helper lipid compositions

Helper lipid vesicles prepared at the three DOPE/DPPC ratios, and using DPPC, ranged between  $104.0 \pm 0.2$  nm and  $121.4 \pm 0.8$  nm (Table 9). In contrast, DOPE helper lipid vesicles had a diameter of  $90.6 \pm 1.3$  nm. PGL NPs assembled with DPPC-based lipid vesicles (at 10:1  $\rho_{\pm}$  charge ratio), had a size range of  $118.1 \pm 2.2$  nm to  $156.8 \pm 4.6$  nm. PDIs of all lipid vesicles and their corresponding PGL NPs were slightly below 0.5, indicating a relatively heterogeneous particle size distribution.

**Table 9** Size and PDI measurements of PG complexes and their corresponding 10  $\rho_{\pm}$  PGL NPs

Helper lipid	Measurement	Lipid vesicles (n=3)	10 $\rho_{\pm}$ PGL NPs (n=3)
100% DOPE	Size (nm) $\pm$ SD	90.6 $\pm$ 1.3	166.7 $\pm$ 5.7
	PDI $\pm$ SD	0.08 $\pm$ 0.03	0.42 $\pm$ 0.04
F2 75% DOPE-25% DPPC	Size (nm) $\pm$ SD	116.8 $\pm$ 1.8	128.5 $\pm$ 3.4
	PDI $\pm$ SD	0.20 $\pm$ 0.003	0.40 $\pm$ 0.01
F3 50% DOPE-50% DPPC	Size (nm) $\pm$ SD	124.6 $\pm$ 0.4	146.1 $\pm$ 3.4
	PDI $\pm$ SD	0.20 $\pm$ 0.01	0.40 $\pm$ 0.03
F4 25% DOPE-75% DPPC	Size (nm) $\pm$ SD	104.0 $\pm$ 0.2	118.1 $\pm$ 2.2
	PDI $\pm$ SD	0.22 $\pm$ 0.01	0.35 $\pm$ 0.02
F5 100% DPPC	Size (nm) $\pm$ SD	121.4 $\pm$ 0.80	156.8 $\pm$ 4.6
	PDI $\pm$ SD	0.22 $\pm$ 0.01	0.36 $\pm$ 0.02

Increasing the proportion of DPPC in DOPE/DPPC helper lipid vesicles was associated with an increase in the corresponding  $\zeta$  potential values (Table 10). The effect of DPPC ratio on  $\zeta$  potential values of the corresponding PGL NPs was not as clear as that seen in co-lipid vesicles. However, PGL NPs assembled with DOPE/DPPC helper lipid vesicles, had positive  $\zeta$  potential values that ranged between +14.2  $\pm$  0.84 mV to +22.5  $\pm$  1.64 mV. It is important to recall that the  $\zeta$  potential of 10:1  $\rho_{\pm}$  PG NPs (without helper lipid vesicles), which was measured in the previous section was +13.2  $\pm$  3.0 mV. The addition of DOPE/DPPC helper lipid vesicles did in fact improve the colloidal stability of 10:1  $\rho_{\pm}$  PG, only to a lesser extent than DOPE vesicles alone ( $\zeta$  potential of PGL<sub>DOPE</sub> = +41.9  $\pm$  2.5 mV).

**Table 10**  $\zeta$  potential measurements of DOPE/DPPC helper lipid vesicles and their corresponding PGL NPs

Mean $\zeta$ potential (mV) $\pm$ SD		
Helper lipid	Lipid vesicles (n=3)	10:1 p $\pm$ PGL NPs (n=3)
100% DOPE	-11.5 $\pm$ 0.6	+41.9 $\pm$ 2.5
F2	-9.6 $\pm$ 0.1	+14.2 $\pm$ 0.235
F3	-5.0 $\pm$ 0.2	+22.5 $\pm$ 1.64
F4	-2.4 $\pm$ 0.1	+19.3 $\pm$ 0.84
F5	+3.3 $\pm$ 0.2	+20.1 $\pm$ 0.642

### 3.1.3. GL+ P NPs assembled with DOPE and F4 helper lipid vesicles

The average size of GL<sub>DOPE</sub> vesicles was 153.7  $\pm$  2.0 nm, which similar to that of GL<sub>F4</sub> vesicles 157.7  $\pm$  0.9 nm. The addition of pDNA to GL NPs revealed a lipid-dependent compaction of pDNA (Table 11). Compared to their GL<sub>DOPE</sub> intermediates, GL<sub>DOPE</sub>+P NPs were smaller (125.3  $\pm$  0.6 nm), while GL<sub>F4</sub>+P NPs were significantly larger (257.1  $\pm$  18.6 nm). These measurements confirm the compaction capacity of DOPE vesicles that was observed in the charge ratio optimization experiment. All PDI values were around 0.2, indicating fairly homogeneous size distribution, and high accuracy of the calculated cumulant z-average size value.

**Table 11** Size and PDI measurements of GL vesicles and GL+P NPs prepared with DOPE and F4 (25% DOPE-75% DPPC) lipid vesicles

Helper lipid	Measurement	GL vesicles (n = 3)	10:1 p <sub>±</sub> GL+P NPs (n = 3)
DOPE	Size (nm) ± SD	153.7 ± 2.0	125.3 ± 0.6
	PDI ± SD	0.22 ± 0.10	0.26 ± 0.0
F4	Size (nm) ± SD	157.7 ± 0.9	257.1 ± 18.6
	PDI ± SD	0.25 ± 0.01	0.36 ± 0.0

GL<sub>DOPE</sub> and GL<sub>F4</sub> vesicles were highly stable, as evident by their respective  $\zeta$  potential values of  $+52.8 \pm 1.5$  mV and  $+38.9 \pm 3.7$  mV, respectively. Combining GL vesicles with pDNA reduced the final  $\zeta$  potential of GL<sub>DOPE</sub>+P and GL<sub>F4</sub>+P NPs to  $+26.4 \pm 0.4$  mV and  $+23.8 \pm 0.7$  mV, respectively (Table 12). These values still infer reasonable colloidal stability for both types of GL+P NPs.

**Table 12**  $\zeta$  potential of GL vesicles and GL+P NPs prepared with DOPE and F4 helper lipid vesicles

Mean $\zeta$ potential (mV) ± SD		
Helper lipid	GL vesicles (n=3)	10:1 p <sub>±</sub> GL+P NPs (n=3)
DOPE	+52.8 ± 1.5	+26.4 ± 0.4
F4	+38.9 ± 3.7	+23.8 ± 0.7

### 3.1.4. PGL<sub>MF</sub> NPs with microfluidized helper lipid vesicles

Microfluidization of DOPE or F4 lipids successfully formed lipid vesicles, sized  $189.0 \pm 3.3$  nm and  $186.1 \pm 5.8$  nm, respectively. DOPE<sub>MF</sub> helper lipid vesicles had a PDI of  $0.09 \pm 0.02$ , indicating a highly uniform lipid vesicle population. PDI of F4<sub>MF</sub> helper lipid vesicles was higher ( $0.37 \pm 0.01$ ) than that of DOPE<sub>MF</sub> lipid vesicles, but was below the 0.5, indicating a normal distribution of vesicle size. The addition of microfluidized lipid vesicles to PG complexes produced PGL<sub>MF-DOPE</sub> with an average size of  $294.3 \pm 11.3$  nm, and PGL<sub>MF-F4</sub> NPs with a  $222.8 \pm 4.2$  nm average size (Table 13). Given that the average size 10:1  $\rho_{\pm}$  PG NPs was  $590 \pm 28.8$  nm, the addition of microfluidized lipid vesicles to PG complexes provided substantial compaction, similar to that seen with thin film helper lipid vesicles.

**Table 13** Size and PDI of microfluidized helper lipid vesicles and the corresponding PGL<sub>MF</sub> NPs

Helper lipid	Measurement	Microfluidized lipid vesicles (n=3)	10:1 $\rho_{\pm}$ PGL <sub>MF</sub> NPs (n=3)
DOPE	Size (nm) $\pm$ SD	$189.0 \pm 3.3$	$294.3 \pm 11.3$
	PDI $\pm$ SD	$0.09 \pm 0.02$	$0.48 \pm 0.03$
F4	Size (nm) $\pm$ SD	$186.1 \pm 5.8$	$222.8 \pm 4.2$
	PDI $\pm$ SD	$0.30 \pm 0.03$	$0.37 \pm 0.01$

10:1  $\rho_{\pm}$  PGL<sub>MF-F4</sub> NPs had a higher  $\zeta$  potential ( $+33.5 \pm 2.9$  mV), and exhibited better colloidal stability than PGL<sub>MF-DOPE</sub> NPs ( $+9.2 \pm 2.1$  mV) (Table 14). Interestingly,  $\zeta$  potential of PGL<sub>MF-DOPE</sub> NPs was lower than that of the original PGL equivalent ( $+41.9 \pm 2.5$  mV). This

suggests that helper lipid vesicle manufacturing method appears to affect the stability of PGL NPs differently, depending on the composition of the helper lipid vesicle.

**Table 14**  $\zeta$  potential of microfluidized helper lipid vesicles and the corresponding PGL<sub>MF</sub> NPs

Helper lipid	Mean $\zeta$ potential (mV) $\pm$ SD	
	Microfluidized lipid vesicles (n=3)	10:1 $\rho_{\pm}$ PGL NPs (n=3)
DOPE	-22.1 $\pm$ 0.77	+9.2 $\pm$ 2.1
F4	+3.2 $\pm$ 0.50	+33.5 $\pm$ 2.9

### 3.2. Confocal microscopy assessment of transfection in RGC-5 cells

#### 3.2.1. Autofluorescence in RGC-5 cells

Pilot flow cytometry assessment of GFP fluorescence in RGC-5 cells, transfected with 10:1  $\rho_{\pm}$  PGL<sub>DOPE</sub> NPs, did not differ from baseline. Subsequent troubleshooting by confocal microscopy of untreated RGC-5 cells revealed a relatively high level of autofluorescence signal in the blue-green spectrum (Figure 12 A). This background autofluorescence resulted in low signal/noise ratio in the flow cytometer's green detection channel. This reduced the sensitivity of the green channel to GFP fluorescence, despite confirmation of GFP expression using confocal microscopy (Figure 12 B). Based on these findings, the tdTomato/calcein fluorophore pair was selected for subsequent flow cytometry assessment, instead of the GFP/CBNF pair. This ensured that gene expression measurement is carried out with a red fluorophore, far from the range of the green autofluorescence spectrum.



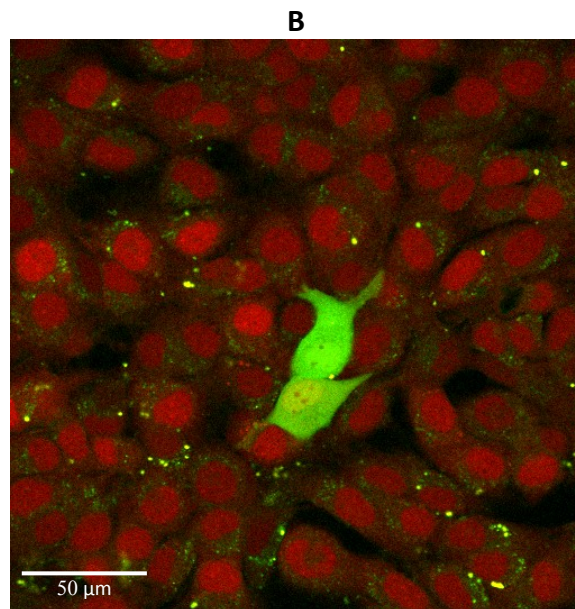
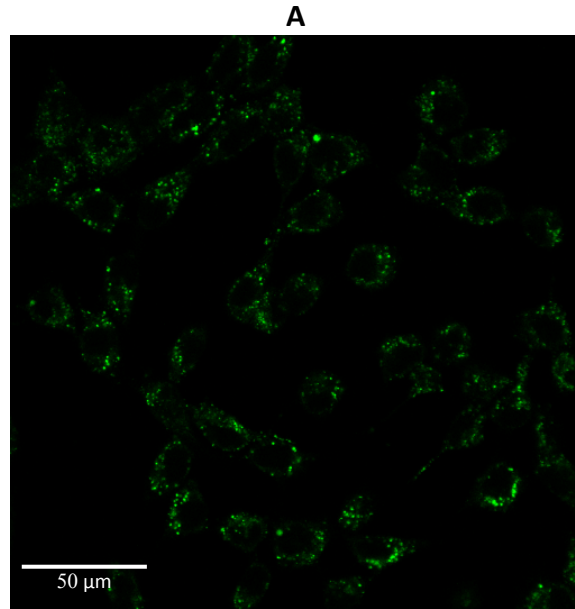


**Figure 12**

**GFP expression in RGC-5 cells, stained with CBNF**

**A.** Confocal microscopy image, taken with the 488 nm laser (5% laser power), of untreated RGC-5 cells in PBS, showing green autofluorescence **B.** RGC-5 cells showing GFP expression (center) were treated with 10:1  $\rho_{\pm}$  PGL<sub>DOPE</sub> NPs. Cells were stained with viability stain CBNF (red) for viability assessment. Green speckles around the cell sample reflects the green spectrum autofluorescence observed in both transfected and untreated RGC-5 cells.

### 3.3. Quantitative assessment of transfection using flow cytometry

#### 3.3.1. Transfection efficiency of PGL<sub>DOPE</sub> NPs as a function of charge ratio ( $\rho_{\pm}$ )

The transfection efficiencies of PGL<sub>DOPE</sub> NPs, prepared at different  $\rho_{\pm}$  charge ratios, was assessed, and compared to that of Lipofectamine. Figure 13 demonstrates that increasing the charge ratio of PGL<sub>DOPE</sub> NPs improves the transfection efficiency to a certain limit, beyond which transfection efficiency decreases. The highest transfection efficiency was obtained using 10:1  $\rho_{\pm}$  PGL<sub>DOPE</sub> NPs ( $M_{TE} = 8.6 \pm 1.6 \%$ ). The transfection efficiencies of 12.5:1 and 15:1  $\rho_{\pm}$  PGL NPs were not significantly different from those prepared at 10:1  $\rho_{\pm}$  charge ratio. However, the 10:1  $\rho_{\pm}$  charge ratio was selected as the optimum condition, based on other considerations, such as toxicity, which will be discussed in later sections. Compared to the optimal 10:1  $\rho_{\pm}$  PGL NPs, Lipofectamine showed higher transfection efficiency in RGC-5 cells ( $M_{TE} = 16.0 \pm 1.2 \%$ ).

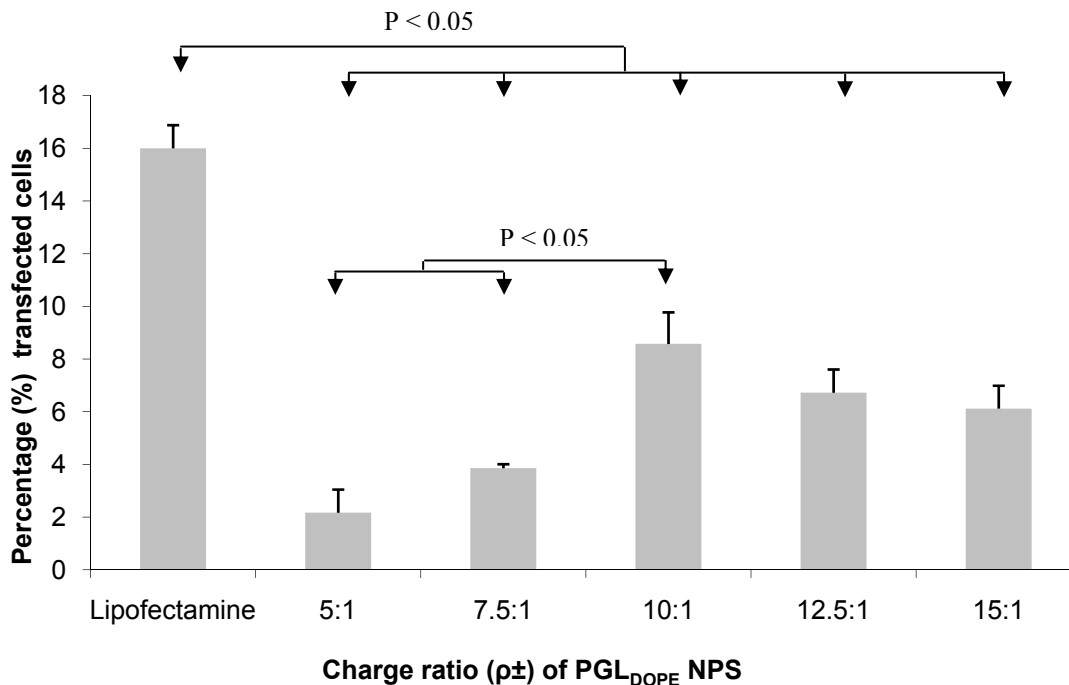


**Figure 13** Comparison of transfection efficiencies of PGL<sub>DOPE</sub> NPs prepared at a range of  $\rho\pm$  charge ratios in RGC-5 cells

RGC-5 cells were transfected with PGL<sub>DOPE</sub> NPs at various  $\rho\pm$  charge ratios. Each dose contained 0.5  $\mu\text{g}$  of pCMV-tdTomato and was applied to approximately  $2 \times 10^5$  RGC-5 cells for 12 hours before analysis. Percentage value  $p < 0.05$  proportion of sampled RGC-5 cells that expressed the tdTomato protein, as determined by cells exhibiting supra-threshold red fluorescence levels. Average intensity of red autofluorescence in no-treatment samples was used as the threshold, beyond which a signal is considered a positive transfection signal. Results are shown as mean ( $n=3$ ); error bars represent standard deviation.

### 3.3.2. Transfection efficiency of PGL NPs as a function of helper lipid composition

The transfection efficiency of PGL NPs was investigated as a function of the helper lipid composition. Figure 14 shows the effect of employing DPPC as a helper lipid, by itself and in combination with DOPE helper lipid vesicles, on the transfection efficiency in RGC-5 cells. Of the

four tested DPPC-based lipid vesicles (F2-F5), the highest transfection efficiency was achieved with PGL<sub>F4</sub> NPs, assembled with the helper lipid, F4 ( $M_{TE} = 5.2 \pm 1.6 \%$ ). PGL<sub>F4</sub> NP transfection efficiency was statistically higher than PGL<sub>F2</sub> NPs only ( $P < 0.05$ ). While PGL<sub>DOPE</sub> NPs were superior to those assembled by the F4 lipid (Figure 14), PGL<sub>F4</sub> NPs were included in further optimization trials, since they can be suitably prepared in neutral pH, an advantage for future ocular applications.

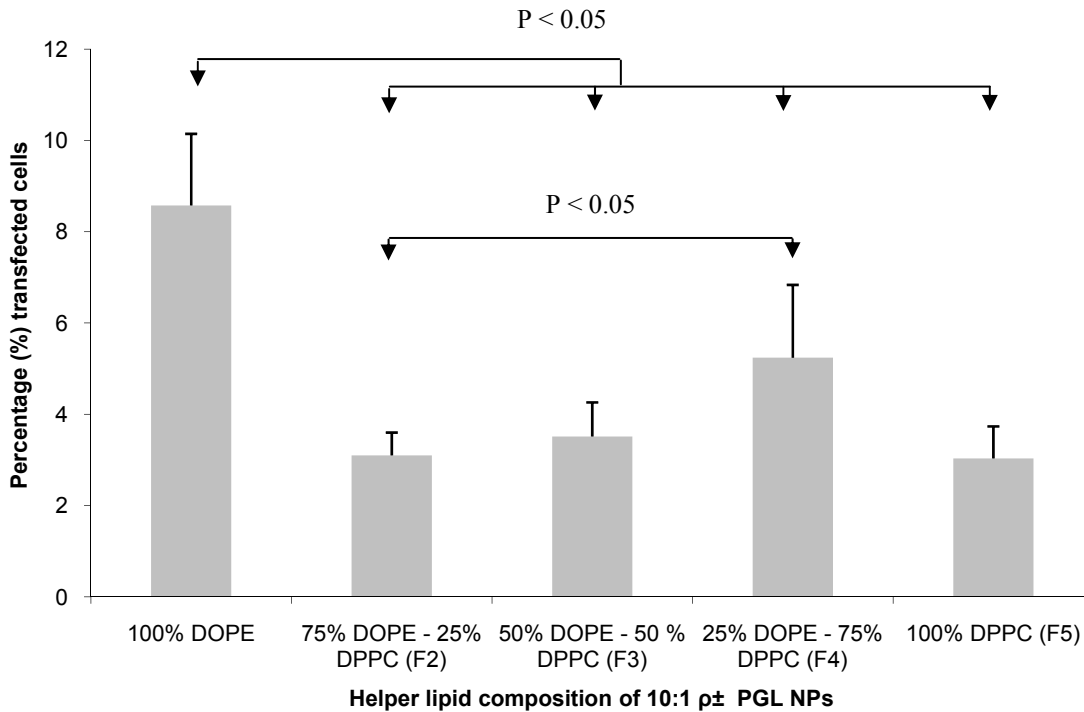


**Figure 14 Comparison of the transfection efficiency of PGL NPs in RGC-5 cells, as function of helper lipid composition**

RGC-5 cells were transfected with 10:1  $\rho_{\pm}$  PGL NPs, assembled with four different DPPC and DOPE/DPPC helper lipid vesicles. The mean transfection efficiency ( $n=3$ ) is presented as a function of the composition of the helper lipid vesicles. Transfection conditions were identical to those used in the previous (charge ratio) optimization experiment. Error bars represent standard deviation.

### 3.3.3. Transfection efficiency of GL+P NPs: effect of the order of assembly

In this experiment, investigation was focused on optimizing the nature of interaction between components of the NP. Here, GL+P NPs were prepared by combining pDNA with preformed gemini-lipid vesicles (GL) in thin film (Mode 2), using DOPE and F4 lipids, separately. The mean transfection efficiency of  $GL_{DOPE} + P$  ( $M_{TE} = 4.6 \pm 3.0 \%$ ) was lower than that of the original  $PGL_{DOPE}$  NPs ( $M_{TE} = 8.6 \pm 1.6 \%$ ); however, the difference was not statistically significant (Figure 15). On the other hand, the transfection efficiency of  $GL_{F4} + P$  ( $M_{TE} = 2.1 \pm 0.3 \%$ ) was significantly lower ( $P < 0.05$ ), compared to that of  $PGL_{F4}$  NPs ( $M_{TE} = 5.2 \pm 1.6 \%$ ). Accordingly, Mode 2 order of assembly was not selected for further optimization, as it does not improve the overall transfection efficiency.

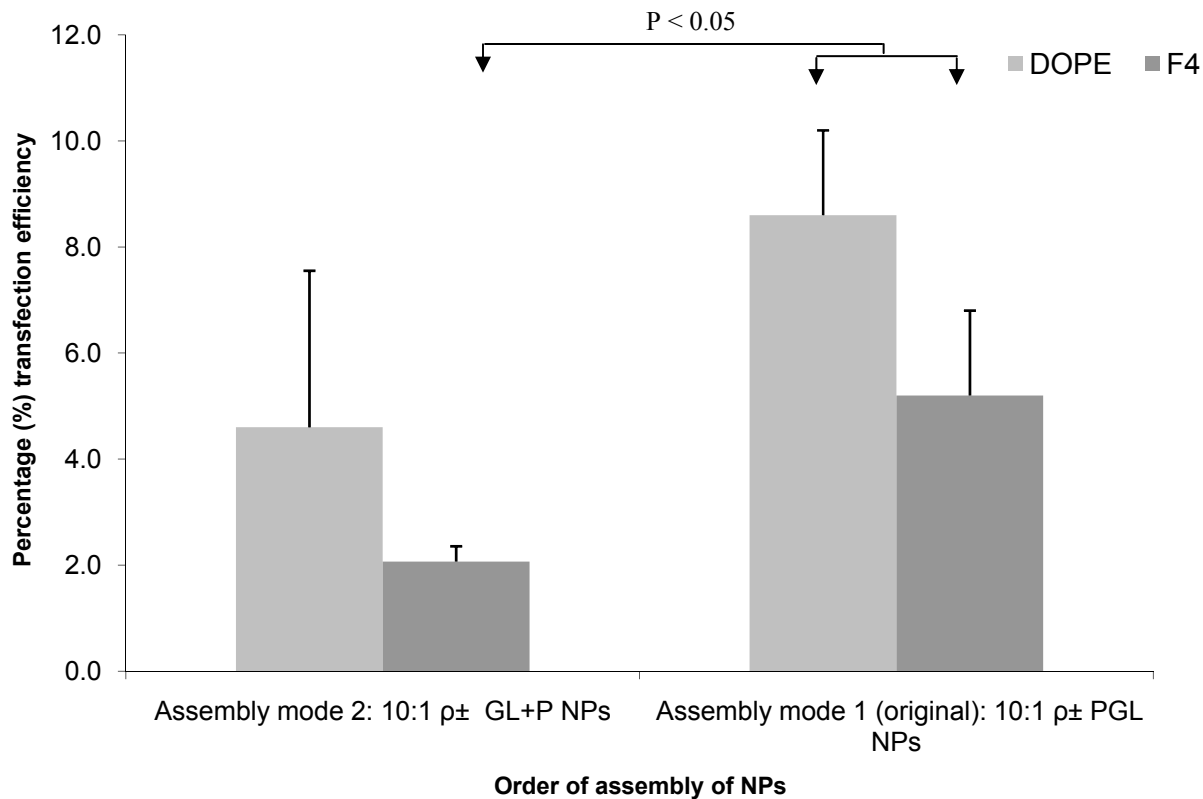


**Figure 15** Comparison of the transfection efficiency of GL+P and PGL NPs, in RGC-5 cells

The effect of NPs' order of assembly on the transfection efficiency in RGC-5 cells is shown, by comparing the transfection efficiency of GL+P NPs to that of PGL NPs. The two optimized helper lipid vesicles, DOPE and F4, were used to prepare NPs, in both modes of assembly. Transfection conditions were identical to those in previous transfection experiments (n=3). Error bars represent standard deviation.

### 3.3.4. Transfection efficiency of PGL<sub>MF</sub> NPs with microfluidized helper lipid vesicles

The following data will highlight the effect of the manufacturing technique of helper lipid vesicles on the transfection efficiency of PGL NPs. Figure 16 shows the transfection efficiency of PGL<sub>MF</sub> NPs, with microfluidized helper lipid vesicles, compared to their original PGL equivalents, which were prepared with thin film lipid vesicles. The transfection efficiency of

both PGL<sub>MF-DOPE</sub> ( $M = 12.3 \pm 1.0 \%$ ) and PGL<sub>MF-F4</sub> ( $M = 14.5 \pm 1.4 \%$ ) NPs, were significantly higher ( $P < 0.05$ ) than their traditional PGL equivalents. While these NPs mediated the highest transfection efficiency, we were unable to use them in further experimentation, since they were developed during final stage of the current work. Accordingly, 10:1  $\rho_{\pm}$  PGL<sub>DOPE</sub>, and 10:1  $\rho_{\pm}$  PGL<sub>F4</sub> NPs were selected as the optimum NPs for subsequent experiments.

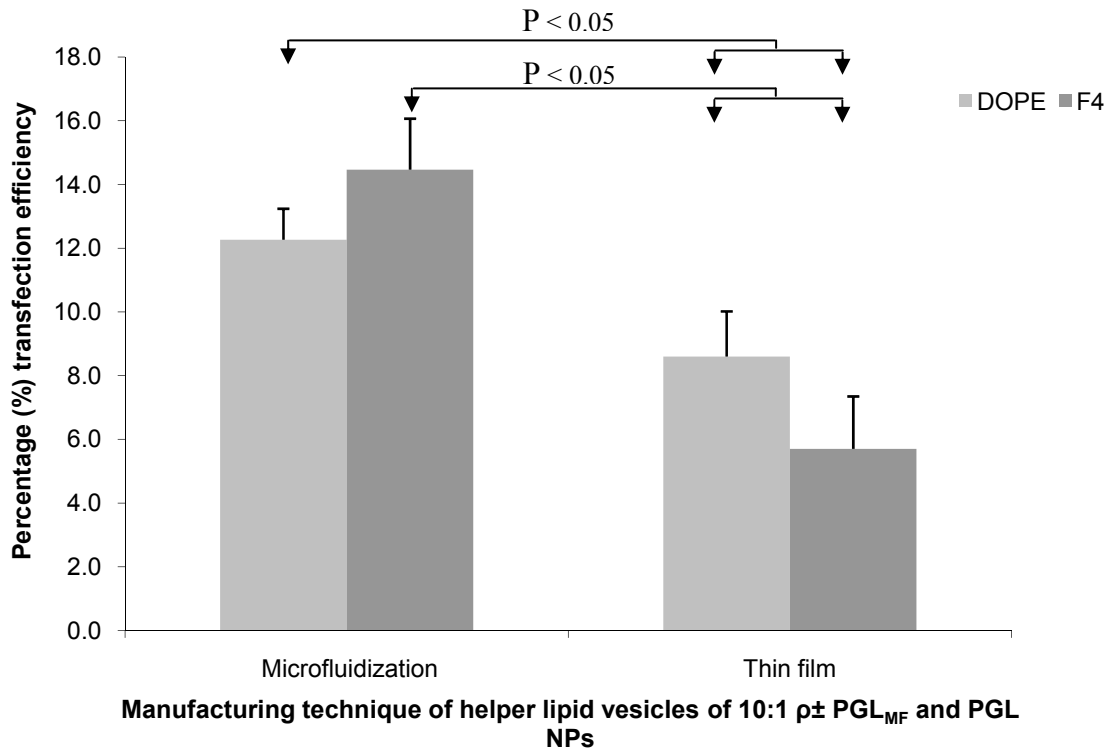
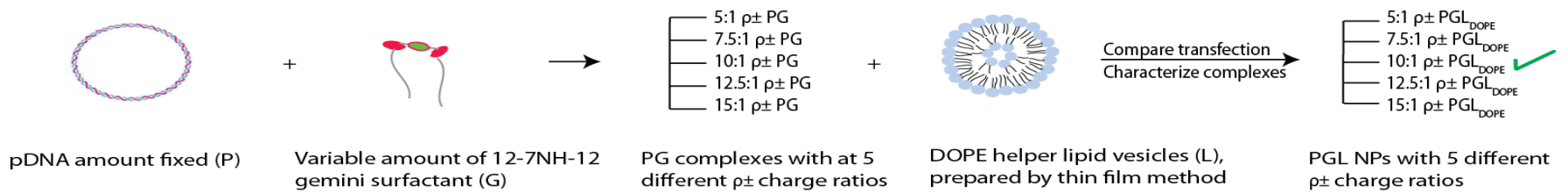


**Figure 16** Comparison of the transfection efficiency of PGL NPs in RGC-5 cells, as a function of the manufacturing technique of helper lipid vesicles

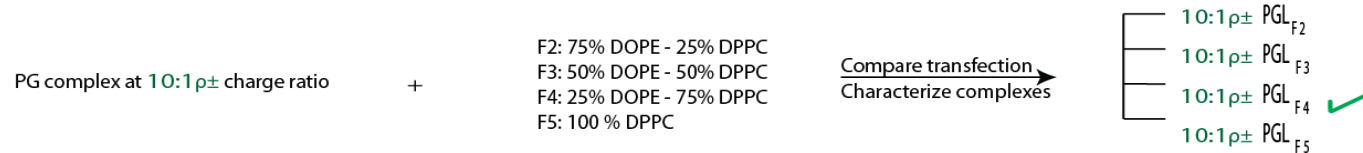
The mean transfection efficiency ( $n=3$ ) of 10:1  $\rho_{\pm}$  PGL<sub>MF</sub> NPs is presented in comparison to that of PGL NPs (assembled with thin film lipid vesicles). Two types of lipids were used to prepare the helper lipid vesicles, including the two optimized DOPE and F4 lipids. Transfection conditions were identical to those in previous transfection experiments. Error bars represent standard deviation.

**Step 1 - Charge ratio optimization:** what is the plasmid-gemini charge ratio ( $\rho_{\pm}$ ) that yields optimal transfection ?



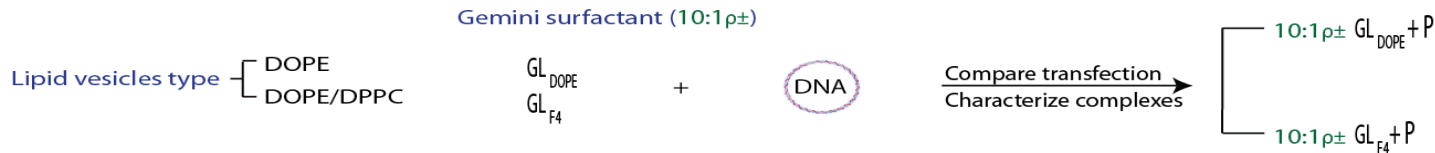
Optimal charge ratio (10:1 $\rho_{\pm}$ ) is advanced to Step 2

**Step 2 - Lipid vesicle composition optimization:** the helper lipid, DPPC was incorporated into DOPE vesicles to create 4 new DOPE/DPPC lipid formulations ( F2-F5). Using the 10:1 $\rho_{\pm}$  PGL NPs, does including DPPC, into their DOPE helper lipids vesicles, improve transfection efficiency ?



F4 ( 25% DOPE - 75% DPPC) lipid composition is advanced to Step 3

**Step 3 - Order of assembly:** NPs were alternatively assembled by firstly combining the gemini surfactant with lipid vesicles (GL), followed by DNA complexation (GL+P). While maintaining optimized parameters, does the order of combining components of NPs affect their transfection efficiency ?



Original mode of preparation is maintained as an optimal mode and is used in Step 4

**Step 4 - Lipid manufacturing optimization:** optimized helper lipid vesicles were alternatively manufactured using high pressure microfluidization. Does the manufacturing method have an effect on the transfection efficiency ?

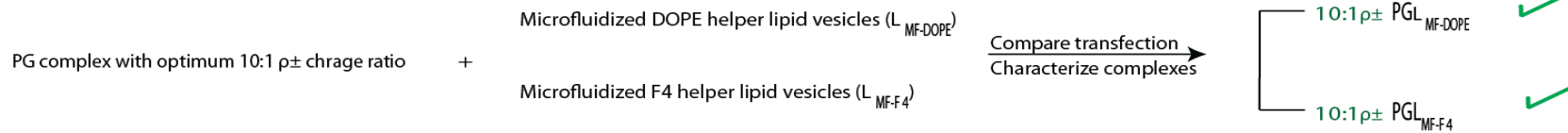


**Figure 17** Summary of 12-7NH-12 NPs' transfection optimization in RGC-5 cells

A multi-stage optimization process was followed to select NP parameters that yield the highest transfection efficiency of NPs in RGC-5 cells. The investigated parameters included NPs'  $\rho_{\pm}$  charge ratio, helper lipid composition, order of assembly, and helper lipid manufacturing technique. The parameter level that yielded the highest transfection efficiency (check mark) was selected for further optimization trials.



### 3.4. Toxicity assessment of 12-7NH-12 based NPs in RGC-5 cells

The viability of RGC-5 cells, following treatment with various 12-7NH-12 formulations was investigated. Exposure of RGC-5 cells to the 12-7NH-12 surfactant alone was the most toxic, with toxicity increasing as the surfactant concentration increased. Toxicity of PG complexes did not significantly differ from that of the 12-7NH-12 surfactant alone (Figure 18). However, similar to the increasing concentration of the applied surfactant, increasing the  $\rho_{\pm}$  charge ratio of PG NPs led to higher toxicity in RGC-5 cells. Incorporating the helper lipid, DOPE into PG complexes provided significant protection of RGC-5 cells, as seen by the relatively high viability readings across all  $\rho_{\pm}$  charge ratios of PGL<sub>DOPE</sub> NPs. The protective effect of DOPE from 12-7NH-12 toxicity is especially apparent at high charge ratios (>10:1  $\rho_{\pm}$ ) where PGL-induced toxicity was several folds lower than PG-induced toxicity. The optimized 10:1  $\rho_{\pm}$  PGL<sub>DOPE</sub> NPs caused no toxicity in RGC-5 cells ( $M_{viability} = 104.0 \pm 10.0 \%$ ).

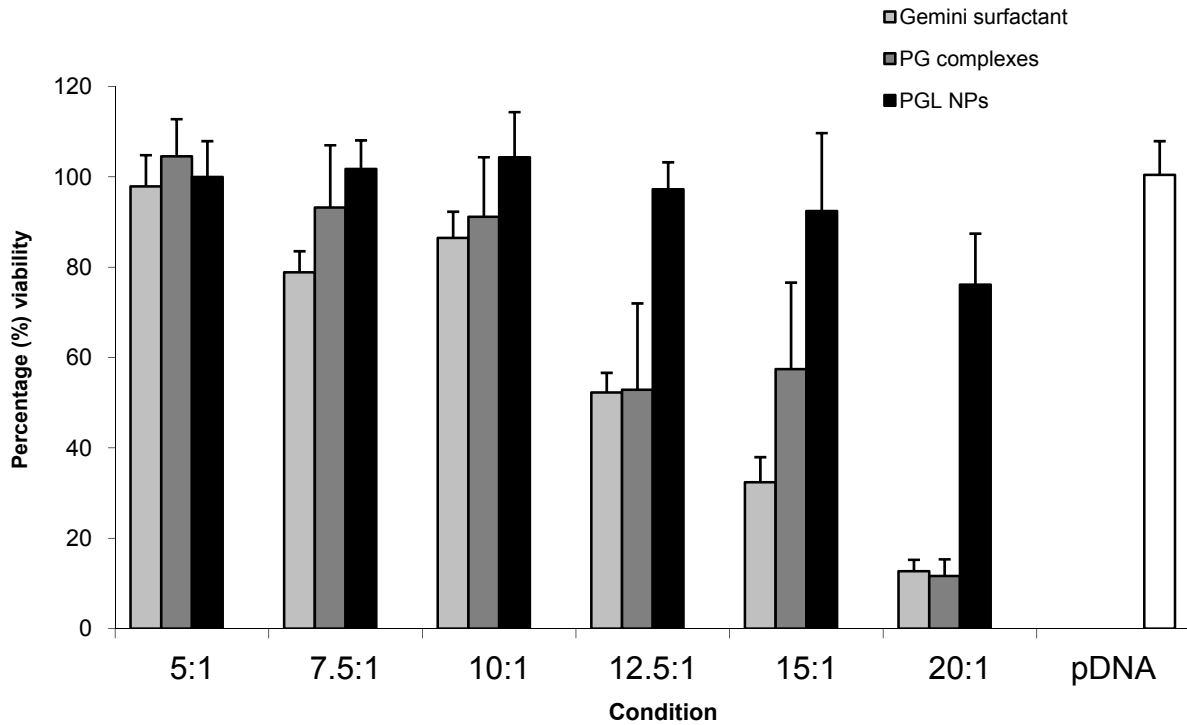


**Figure 18** Assessment of cellular toxicity in RGC-5 cells, induced by PGL<sub>DOPE</sub> NPs, their intermediate complexes and individual components.

RGC-5 cell viability was assessed after a 12 hour incubation period with a range of 12-7NH-12 surfactant concentrations (light grey bars), PG complexes at various charge ratios (dark grey bars), and PGL<sub>DOPE</sub> NPs at different  $\rho_{\pm}$  charge ratios (black bars). The concentrations used in this assay are identical to those used in the transfection efficiency assessment. Viability measurements are presented as a mean (n=3); error bars represent standard deviation.

DOPE, DPPC and DOPE/DPPC helper lipid vesicles, as well as their corresponding PGL NPs were highly biocompatible with RGC-5 cells, causing no significant toxicity (Figure 18). Viability of RGC-5 cells, following treatment with DOPE, DOPE/DPPC, and DPPC helper lipid vesicles, between 90%-100% (Figure 19). The viability of RGC-5 cells following treatment with the corresponding PGL NPs was ~ 100%.

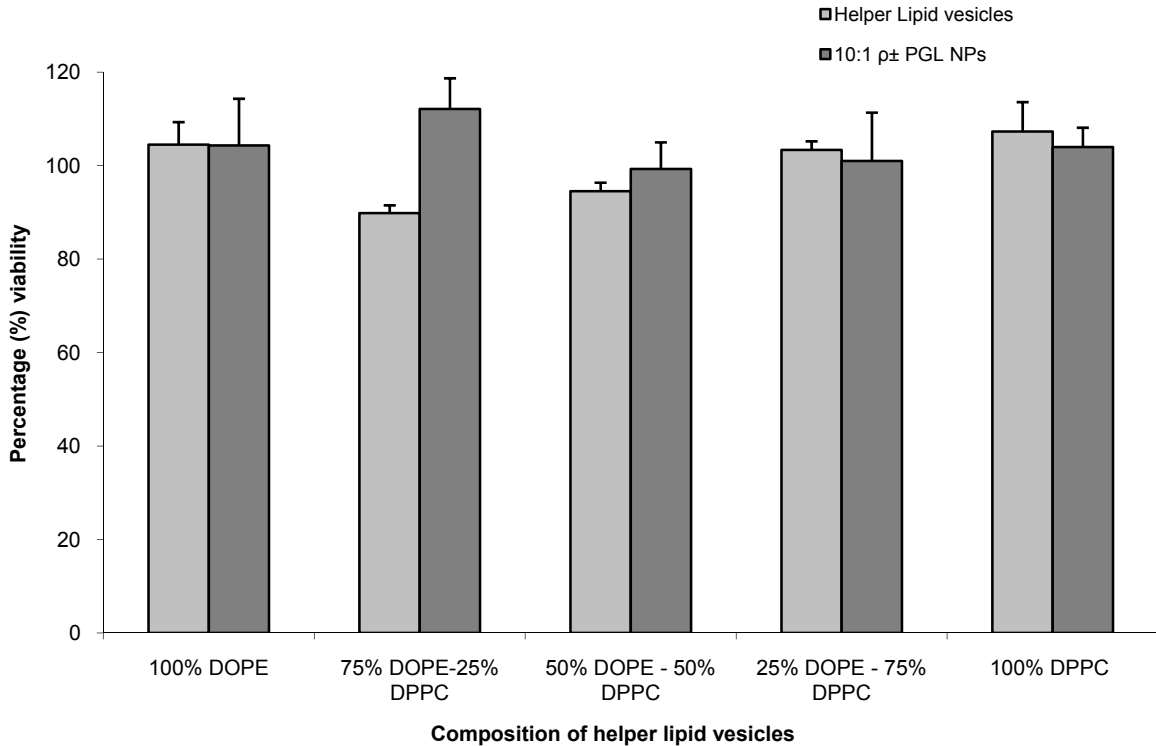


**Figure 19 Assessment of cellular toxicity in RGC-5 cells, induced by helper lipid vesicles and corresponding PGL NPs**

RGC-5 cell viability was assessed after a 12 hour incubation period with DOPE, DPPC, and DOPE/DPPC helper lipid vesicles (light grey bars), as well as the corresponding PGL NPs (black bars). The concentrations used in this assay are identical to those used in the transfection efficiency assessment. Viability measurements are presented as a mean (n=3); error bars represent standard deviation.

### 3.5. Assessment of RGC-5 neurite outgrowth as a function of BDNF expression in RGC-5 cells

Expression of BDNF in RGC-5 cells was induced, using PGL<sub>DOPE</sub>, PGL<sub>F4</sub> NPs and Lipofectamine, each carrying the BDNF gene in the bicistronic plasmid, pCMV6-AC-GF. Average neurite length of RGC-5 cells, treated with these NPs did not induce any significant neurite outgrowth (Figure 20). Treatment of RGC-5 cells with the human hrBDNF was used as a control, to compare its effect on neurite outgrowth, to that of NPs. This study revealed that the mean

neurite outgrowth in RGC-5 cells treated with 50 ng/mL BDNF ( $M_{neurite\ length} = 58.4 \pm 11.7 \mu\text{m}$ ) (Figure 21-A), was statistically higher ( $p < 0.05$ ) than baseline ( $M_{neurite\ length} = 38.8 \pm 3.4 \mu\text{m}$ ) (Figure 21-B). Increasing the concentration of the BDNF protein to 100 ng/mL and 200 ng/mL did not induce any significant neurite outgrowth in RGC-5 cells.

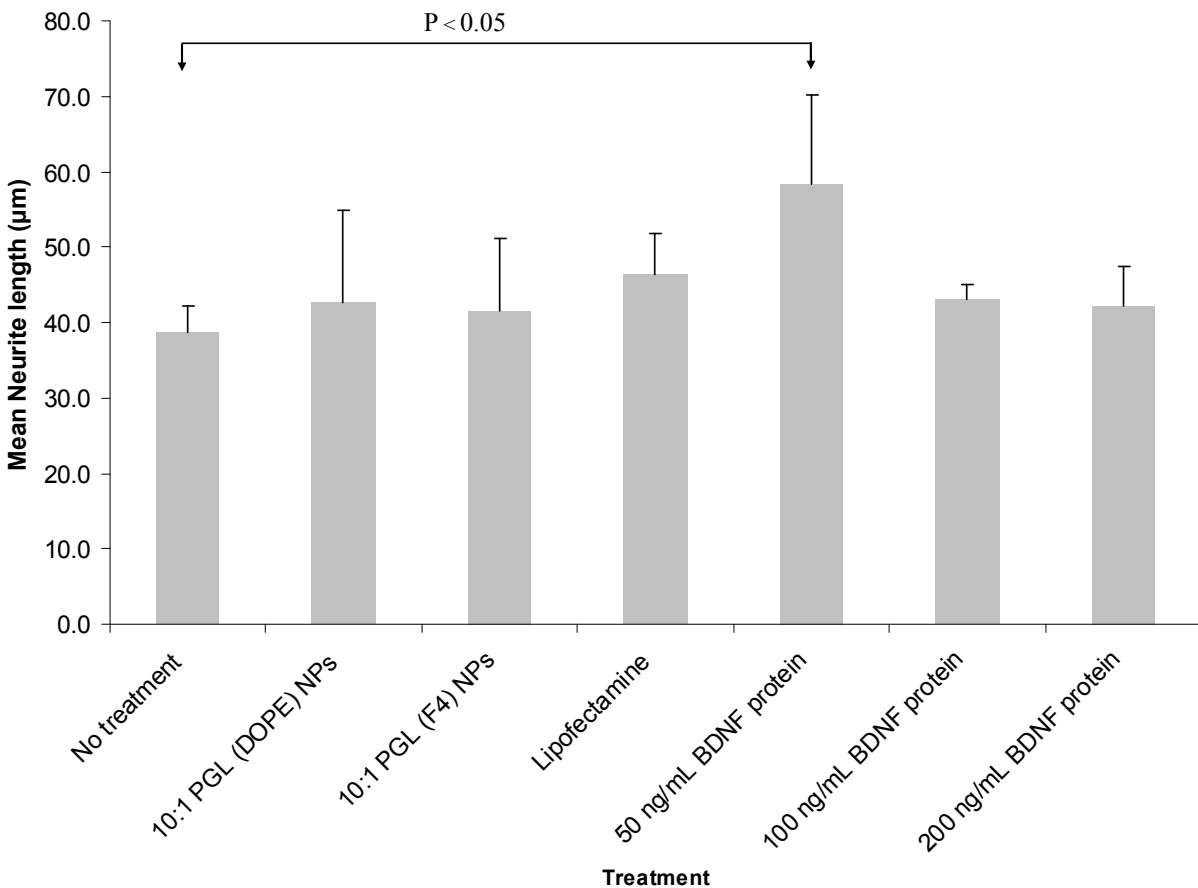


**Figure 20** **Assessment of neurite outgrowth in of RGC-5 cells, following treatments with several NPs and various concentrations of the BDNF protein.**

RGC-5 cells were treated with three NPs carrying pCMV6-AC-GFP, which encodes for the BDNF gene. NPs included the two optimized 10:1  $\rho\pm$  PGL<sub>DOPE</sub> and 10:1 PGL<sub>F4</sub> NPs, as well as Lipofectamine Plus lipoplexes. Additionally, the hrBDNF protein was used at three different concentrations 50 ng/mL, 100 ng/mL, and 200 ng/mL, to generate a standard curve, which would enable estimation of BDNF expression levels in tranfected cells, based on neurite outgrowth response. Cells were exposed to the treatments for a total period of 24 hours. Neurite outgrowth is presented as a mean neurite length of analyzed RGC-5 groups (n=3); error bars represent standard deviation.

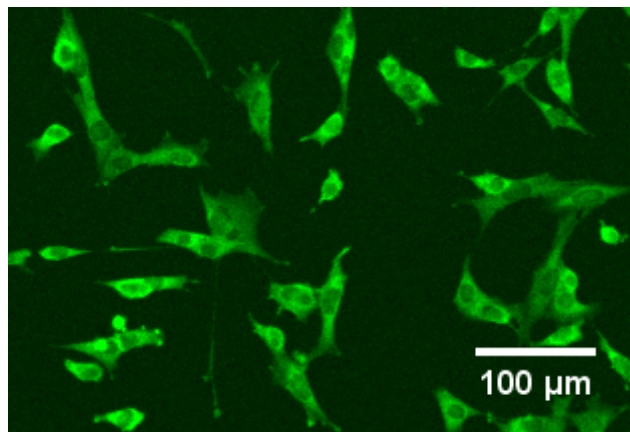
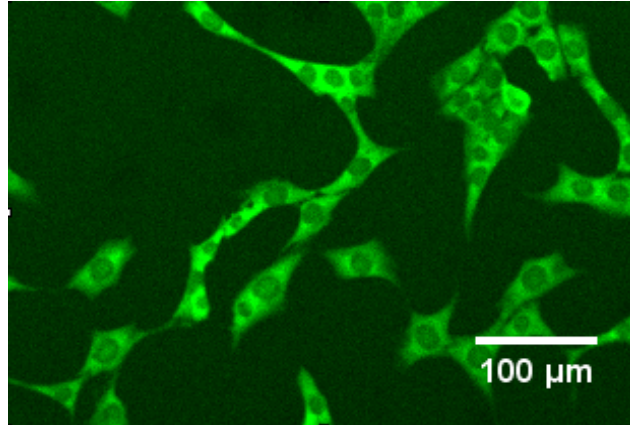


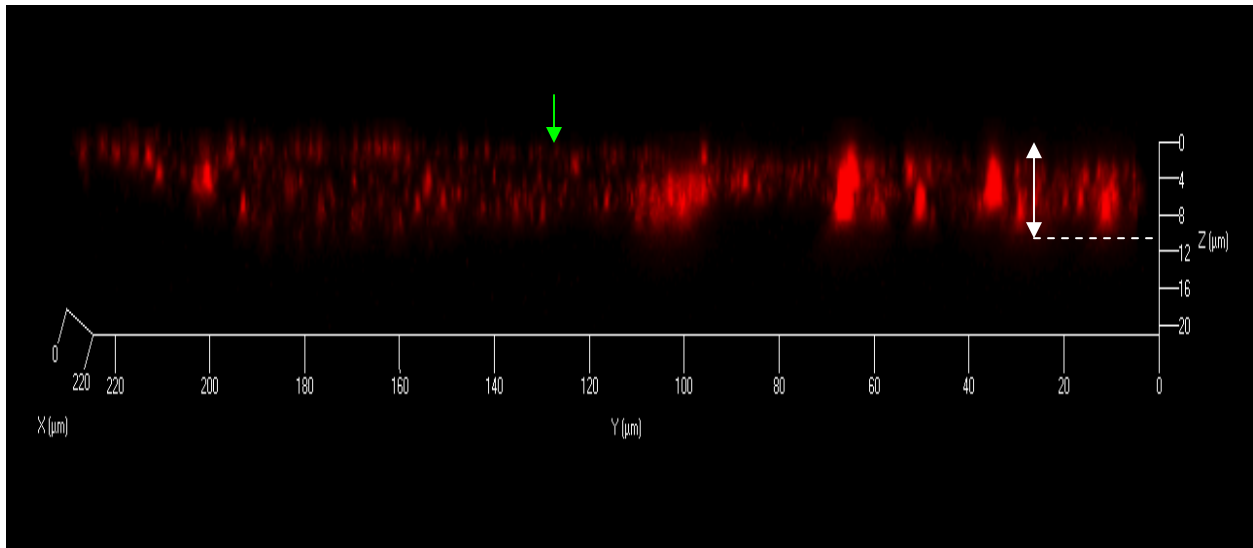
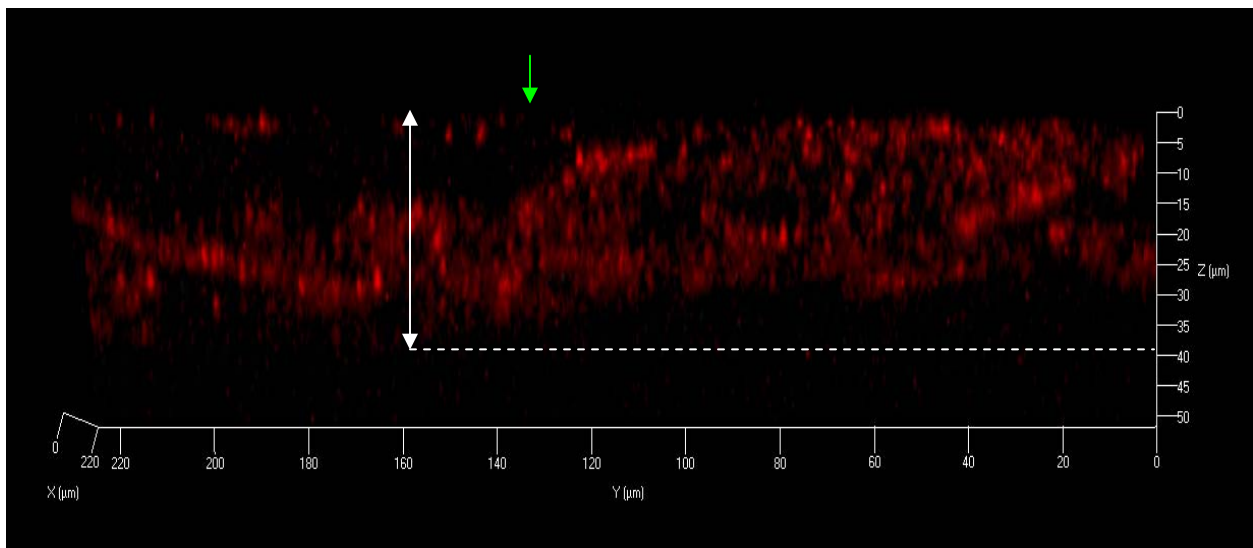
**Figure 21** Confocal microscopic images of RGC-5 cells, stained with Anti- $\beta$  III Tubulin Monoclonal Antibody, FITC conjugate.

Images are representative of typical neurite length of RGC-5 cells treated with A) 50 ng/mL hrBDNF, and B) serum-free media. Neurite length was assessed 24 hours after dose treatment. FITC has an excitation wavelength of 495 nm and an emission wavelength of 525 nm. Images were captured using the 488 nm laser of the Zeiss CLSM 710 at 100 x magnification.

### **3.6. Assessment of PGL NP permeation and toxicity in an epithelial corneal model**

#### **3.6.1. Permeation capacity of 10:1 p $\pm$ 12-7NH-12 PGL<sub>DOPE</sub> NPs**

This study was carried out to determine whether PGL<sub>DOPE</sub> NPs could permeate across the corneal epithelium, since the transcorneal pathway could be a potential route towards the retina. Following topical application, confocal microscopic assessment of HCE tissues indicated that 10:1 p $\pm$  PGL<sub>DOPE</sub> NPs successfully adhered to the surface of the epithelium, within the first two hours, as can be seen by the localization pattern of the Cy5 labeled pDNA (Figure 22-A). Additionally, a permeation depth of 10 – 12  $\mu$ m, within the superficial corneal epithelial layer, can be observed. Fifteen hours post-treatment, NPs appeared to have reached the centre of the corneal epithelium, after achieving a maximum permeation depth of approximately 35-40  $\mu$ m (Figure 22-B). A proportion of the applied NPs remained at the surface of the epithelium, while the majority of NPs were distributed throughout the first half of the epithelium. The entire thickness of the HCE is approximately 65  $\mu$ m, as was determined in this experiment. The reported average thickness of the corneal epithelium, measured *in vivo* is approximately 50  $\mu$ m [112].

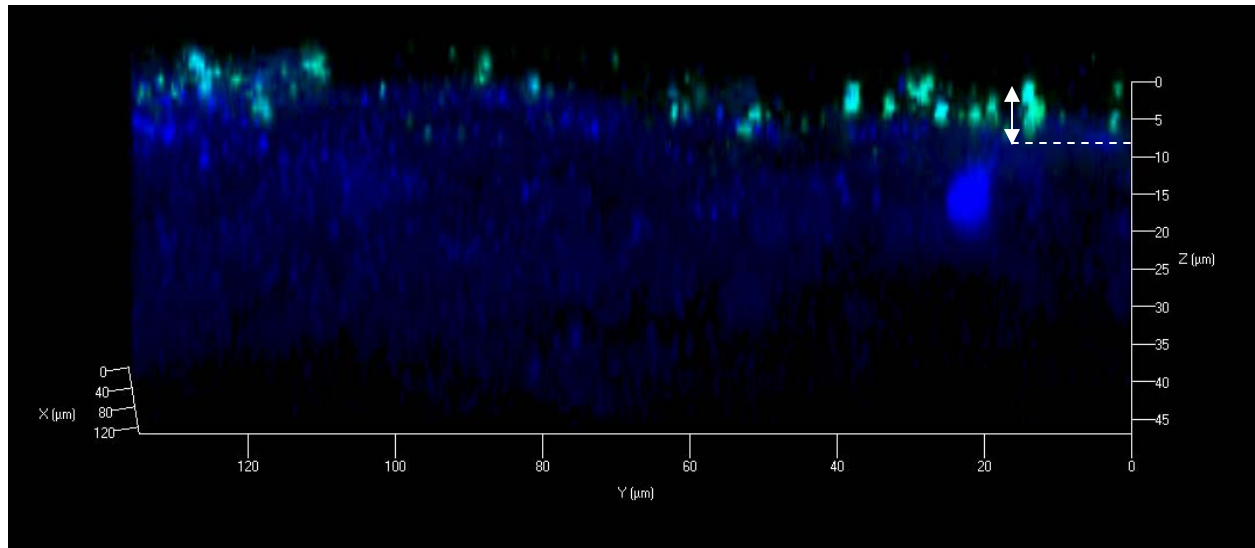
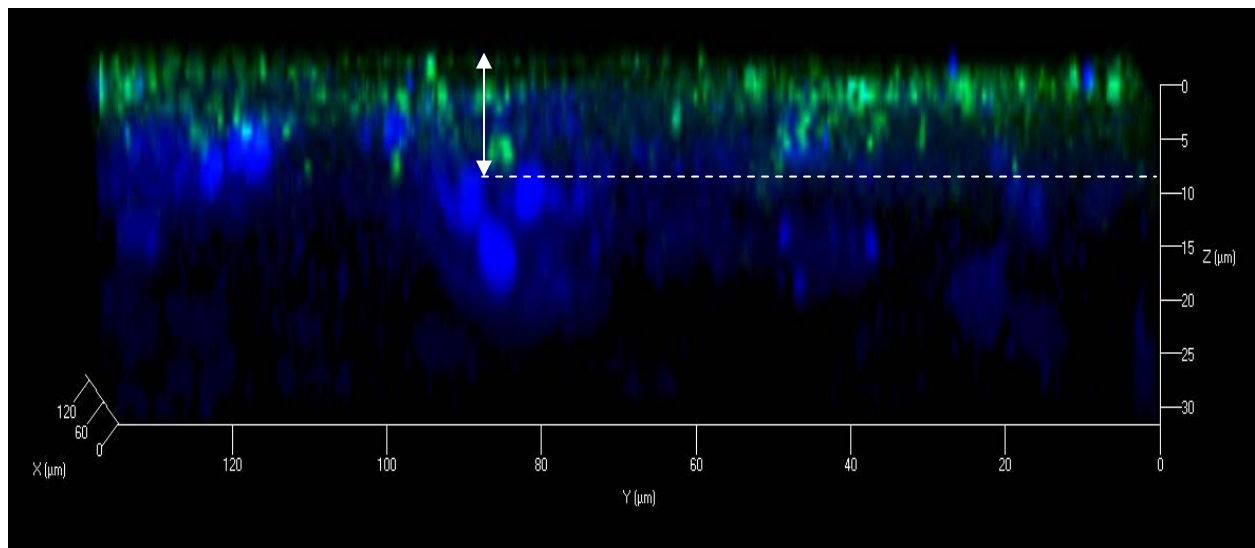
**A****B**

**Figure 22** Confocal microscopic study of binding and permeation of 10:1  $\rho_{\pm}$  PGL<sub>DOPE</sub> NPs, 2 hours (A) and 15 hours (B) after topical application *in vitro* in the EpiOcular™ HCE model.

3D rendered images of human corneal epithelial tissue treated with 10:1  $\rho_{\pm}$  PGL<sub>DOPE</sub> NPs, carrying Cy5 labeled pCMV6-AC-GFP (red). (A) 2 hours after topical application, PGL NPs achieved a permeation depth of 10–12  $\mu\text{m}$  into the corneal epithelium (double-headed arrow). (B) After 15 hours, a proportion of PGL NPs completed a maximum permeation distance of approximately 35–40  $\mu\text{m}$  (double-headed arrow), while a proportion of the NPs remained trapped on the corneal surface (green arrow).



Two control GL vesicles, void of pDNA were used as comparison for the PGL<sub>DOPE</sub> NP's structure-related corneal permeation. Microfluidized GL vesicles, which were shown to have an equivalent size ( $150.2 \pm 3.2$  nm) to that of PGL<sub>DOPE</sub> NPs ( $166.7 \pm 5.7$  nm), achieved a permeation depth of less than 5  $\mu$ m (Figure 23-A). This finding indicates the electrostatic configuration of gemini NPs, favors corneal permeation, in the presence of pDNA, compared with its absence. Similarly, thin film GL vesicles (also void of pDNA), achieved a similar permeation depth (8  $\mu$ m), 25 hours after topical application in the HCE model (Figure 23-B). The extended permeation was time was allowed only for these vesicles to highlight their limited permeation capacity.

**A****B**

**Figure 23** Binding and permeation capacity of microfluidized  $GL_{MF-DOPE}$  (A) and thin film  $GL_{DOPE}$  vesicles (B), 25 hours after topical application.

Microfluidized  $GL_{MF-DOPE}$  and  $GL_{DOPE}$  vesicles were tagged with the fluorescent lipid, NBD-PE (green) for tracking of vesicles, following topical administration. Both types of GL vesicles achieved a permeation depth of 5-8  $\mu\text{m}$ , 25 hours after application to the HCE tissue. Corneal inserts were stained with the nucleic acid stain DRAQ-5 (blue) to highlight the depth of the tissue.

### 3.6.2. MTT assessment of PGL NPs toxicity in a HCE model

An MTT assay was used to assess the corneal toxicity induced by several PGL NP formulations in the EpiOcular HCE model. Figure 24 shows the normalized viability of HCE model tissue, after a 24 hour exposure to three PGL NPs, including 10:1, 20:1  $\rho_{\pm}$  PGL<sub>DOPE</sub> and 10:1  $\rho_{\pm}$  PGL<sub>MF-DOPE</sub>. The optimized 10:1  $\rho_{\pm}$  PGL<sub>DOPE</sub> NPs caused a low level of toxicity within the HCE tissue ( $M_{\text{viability}}$ : 94.8  $\pm$  6%). The manufacturing method of DOPE helper lipid vesicles does not appear to affect the viability HCE tissue, which can be seen by only a relatively high viability, following treatment of HCE tissue with 10:1  $\rho_{\pm}$  PGL<sub>MF-DOPE</sub> ( $M_{\text{viability}}$ : 94.4  $\pm$  22%). Increasing the charge ratio of PGL<sub>DOPE</sub> NPs to 20:1  $\rho_{\pm}$  reduced the viability of corneal model cells ( $M_{\text{viability}}$ : 81.8  $\pm$  22%), compared to treatment with 10:1  $\rho_{\pm}$  PGL NPs; however, the difference is not statistically significant. Two of the surfactants, SDS (anionic) and benzalkonium chloride (cationic), that were used as positive controls were found to be highly toxic to HCE cells (approximately 4% and 7% of cells were viable, respectively). Treatment with pDNA alone and with the non-ionic Tween 80 surfactant, caused no significant irritation in the HCE tissue (~ 90-100% viability).

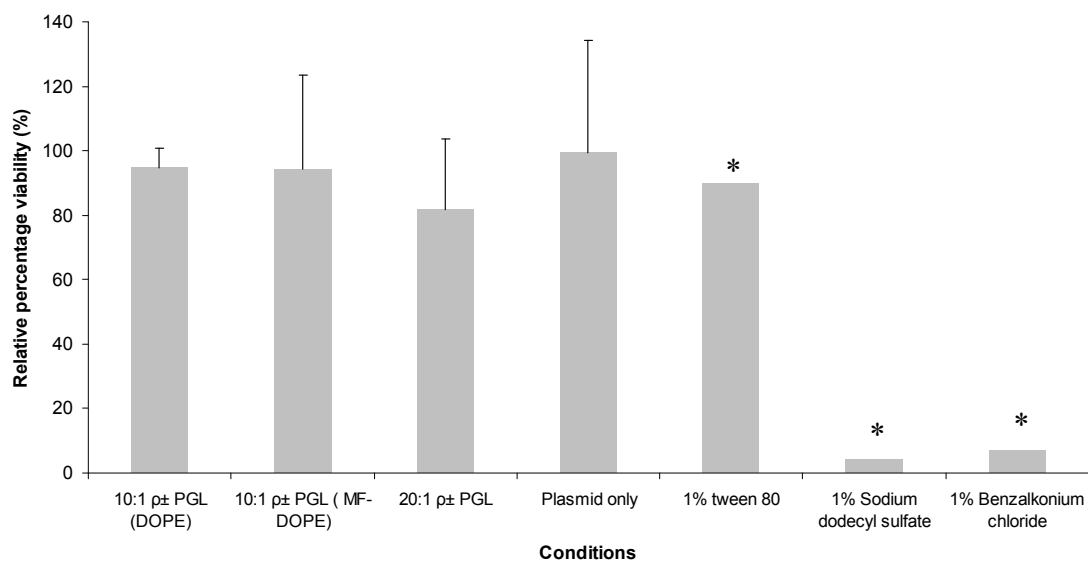


**Figure 24** **Assessment of corneal toxicity of several PGL NPs, and various surfactants in the EpiOcular HCE model**

Viability of HCE model tissue was assessed, following a 24-hour incubation period with 10:1, 20:1  $\rho_{\pm}$ PGL<sub>DOPE</sub> NPs, and 10:1  $\rho_{\pm}$  PGL<sub>MF-DOPE</sub> NPs. Viability of NPs is presented as an average (n=2); error bars reflect standard deviation. Several controls were used for comparison, including pDNA, Tween, SDS, and benzalkonium chloride. Viability values were normalized to the no-treatment control.

\* Controls were run once, due to tissue sample limitations.

### **3.7. *In vivo* evaluation of biodistribution and transfection in mice**

Confocal microscopy assessment of eye sections, collected from all treated animals, revealed only a biodistribution pattern of NPs within ocular tissue after: 1) intravitreal injection of 10:1  $\rho\pm$  PGL<sub>DOPE</sub> NPs and 2) topically administered fluorescent 10:1  $\rho\pm$  PGL<sub>DOPE-N</sub> (short-term assessment). All other analyzed tissue samples revealed neither expression, nor biodistribution –associated fluorescence.

#### **3.7.1. Evaluation of biodistribution of PGL<sub>DOPE</sub> NPs *in vivo***

Four hours after topical administration of the fluorescently tagged 10:1  $\rho\pm$  PGL<sub>DOPE-N</sub> NPs, Cy5 labeled pDNA was localized around the limbus (Figure 25- A2), the iris, and the conjunctiva (Figure 25-D2). The green fluorescent NBD-PE lipid, which was used incorporated in these NPs, was not observed in any of the aforementioned tissues. Imaging did not reveal any evidence of pDNA localization in the retina or the posterior chamber (Figure 25-C2). Imaging of tissue, that was collected 48 hours post topical administration, did not show any pDNA localization or GFP expression.

Fourty eight hours following the intravitreal injection of 10:1  $\rho\pm$  PGL<sub>DOPE</sub> NPs, Cy5 labeled pDNA was localized within the nerve fiber layer (NFL) of the retina, near the interface with ganglion cell layer (Figure 26-B1). Labeled pDNA can also be seen within other ocular parts, including the lens and the vitreous. However, the majority of the NPs' payload appeared to have localized within the inner retina. Despite of pDNA localization within the retina, GFP expression was not observed. In contrast, no pDNA was located in ocular tissue, following intravitreal injection of naked, labeled pDNA.

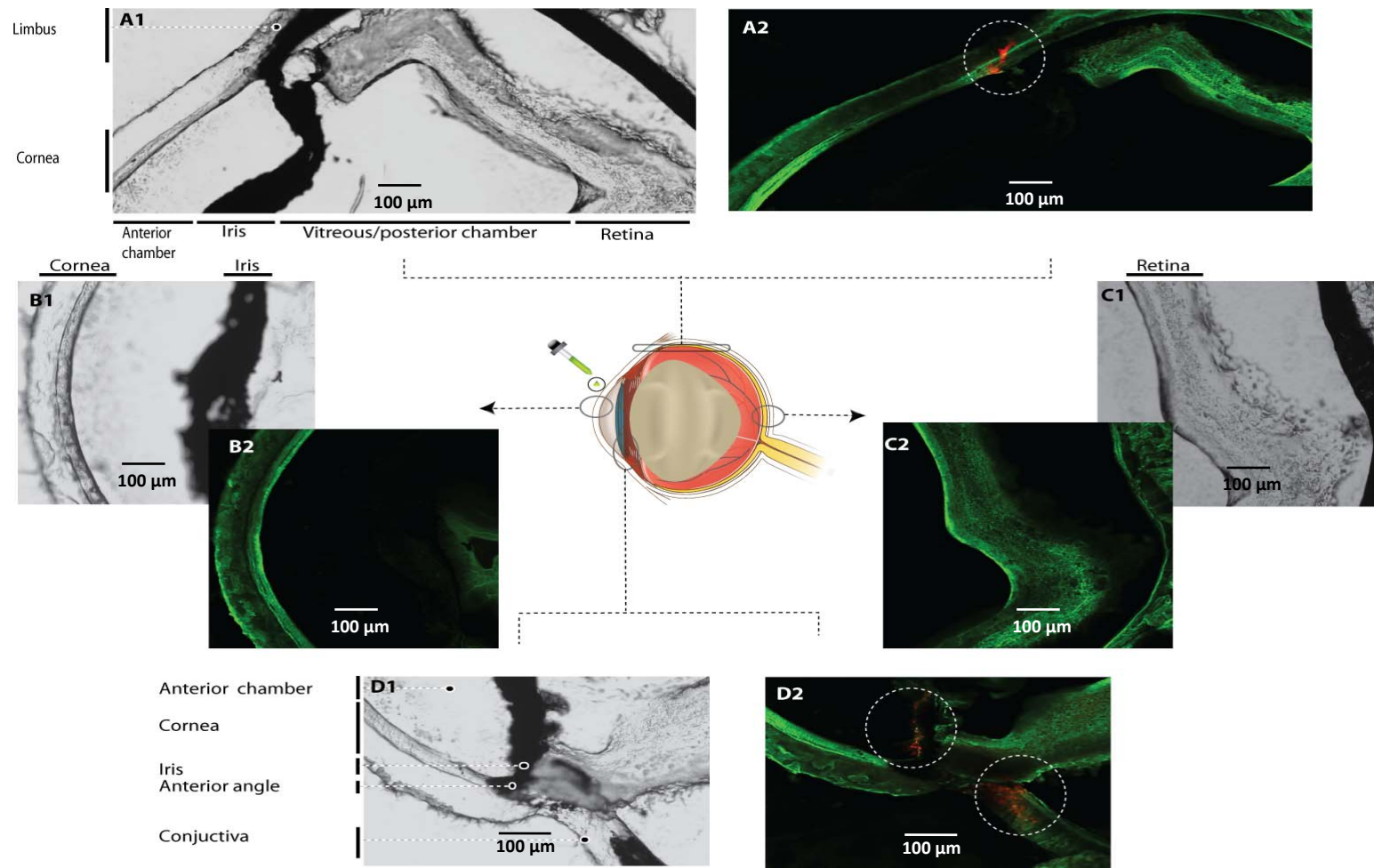


**Figure 25** Biodistribution pattern of PGL<sub>DOPE-N</sub> NPs, 4 hours after topical application

Cy5 labeled pDNA (red) was localized around the conjunctiva, the limbus and the iris (white circles, A2, D2). Ocular tissue was stained using WGA, Alexa Fluor 488 conjugate (green). Animals were treated with the fluorescently tagged 10:1  $\rho \pm$  PGL<sub>DOPE-N</sub> NPs, carrying 1.0  $\mu\text{g}$  of Cy5 labeled pDNA. Bright field images (left of confocal microscopic images) of the same tissue location are presented to highlight anatomical details (note the relatively large lens in the mouse eye). Animal (n=1) were sacrificed 4 hours after topical dose administration.

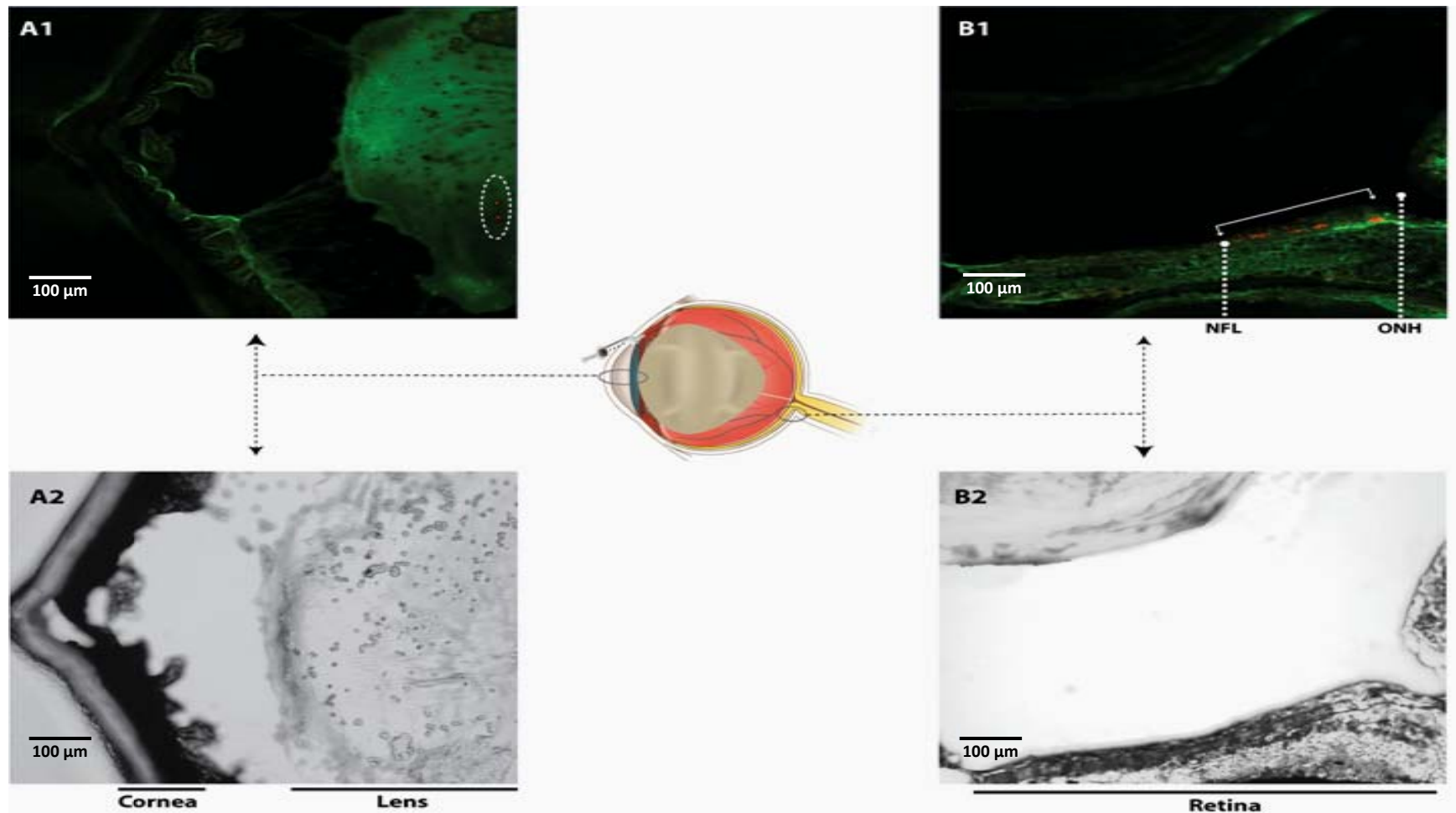


**Figure 26 Biodistribution pattern of PGL<sub>DOPE</sub> NPs 48 hours after intravitreal injection**

Cy5 labeled pDNA (red) is mainly localized within the NFL of the retina, around the lens and the vitreous. The ocular tissue was stained, using WGA Alexa Fluor 488 conjugate (green). Animals were treated with the original 10:1  $\rho \pm$  PGL<sub>DOPE</sub> NPs, carrying 0.1  $\mu$ g of Cy5 labeled pDNA. Bright field images (below confocal microscopic images) of the same tissue location are presented to highlight anatomical details (note the relatively large lens in the mouse eye). Animals (n=3) were sacrificed 48 hours after topical dose administration.

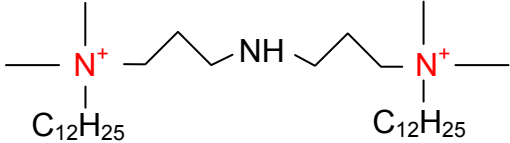
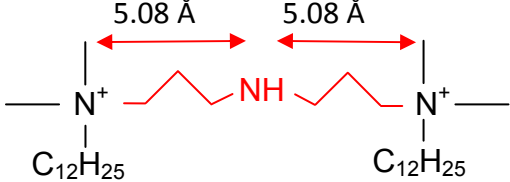
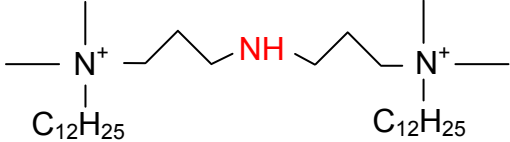
## 4. Discussion

### 4.1. Design of 12-7NH-12 NPs for the retina

Previous studies from our laboratory have demonstrated the potential of gemini surfactants (a library of dicationic first-generation underivatized and second-generation derivatized cationic compounds) as efficient and relatively safe gene delivery systems, both in cell culture and animal models [95, 113-115]. The pH-sensitive second-generation gemini NPs in particular, and namely 12-7NH-12 GL-NPs were amongst the most efficient in gene delivery, in the murine keratinocyte cell line (PAM 212) [114]. Particle characterization data of 12-7NH-12 GL-NPs provided several possible explanations for their enhanced performance, compared to other gemini NPs. First, the 12-7NH-12 surfactant is thought to have an enhanced affinity for DNA, given that the distance between the two cationic head groups and the NH group within the spacer (i.e. the length of the three carbon chain) closely matches the distance between phosphate groups on the DNA backbone [114]. Compared to other gemini surfactants that have a different charge configuration, the 12-NH-12 surfactant was designed to bind to DNA and compact it more efficiently. Second, the spacer's amine group is thought to aid in the release of DNA in the cytoplasm, via induction of pH-sensitive structural change that facilitates endosomal escape of NPs [95]. Third, 12-7NH-12 NPs have an excellent safety profile, causing very minimal toxicity in several cell lines or observable immune reactions following administration in animals [97, 113, 114]. Due to these advantages (Table 15), 12-7NH-12 GL-NPs were chosen for further optimization for gene delivery in the RGC-5 neuronal cell line. These features are presented in Table 15 to demonstrate their relevance to ocular gene delivery applications.



**Table 15 Advantages of employing the 12-7NH-12 gemini surfactant as a building block for a retina-targeted PGL NPs**

Attribute	Description	Implication for ocular improved delivery	Functional group/structure
<b>Cationic net charge</b>	The 12-7NH-12 surfactant has a net positive charge, contributed by the two quaternary ammonium groups, which make up the molecule's headgroups.	- Improved binding to negatively charged ocular tissues, including the cornea and the retina. This ultimately increases the bioavailability of the transgene in targeted tissues.	 <p style="text-align: center;">12-7NH-12</p>
<b>Spacer structure</b>	The distance between the N1-N2-N3 head groups of the 12-7NH-12 surfactant (5.08 Å) is similar to that between the phosphate groups that make up DNA's structural backbone (6.5-7.1 Å) [116, 117].	- Highly specific electrostatic binding between the gemini surfactant and DNA [113]. This provides additional protection of the therapeutic transgene <i>in vivo</i> , from various DNA degradation mechanisms.	 <p style="text-align: center;">12-7NH-12</p>
<b>pH sensitivity</b>	The secondary amine of the spacer is a pH sensitive group, which was shown to significantly improve transfection efficiency. This effect is believed to occur due to pH-dependent ionization and subsequent structural changes of the NP, particularly in the acidic endosomal vesicles, which is thought to aid in more efficient DNA release [106].	Improved gene transfer capacity to ocular tissue, and consequently better expression of transgenes. The hypothesized pH dependent structural change of the NP could allow for a timely release of DNA in target ocular tissues. For example, this function could improve transgene retention during vitreal migration, and allow its timely release, specifically in retinal cells.	 <p style="text-align: center;">12-7NH-12</p>

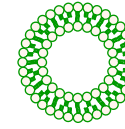
---

**Compaction  
by lipid  
vesicles**

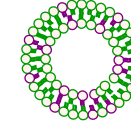
Incorporation of DOPE and DOPE/DPPC helper lipid vesicles within gemini NPs further improves transgene compaction (150-250 nm) and structural stability, enhances the fusion capacity of NPs with cellular and endosomal membranes, and reduces toxicity [118].

- The improved transgene compaction results in a smaller NP size, which allows better access to ocular tissues, through facilitated passage through the tight junctions of the cornea and the inner limiting membrane (ILM) of the retina.

- Neutral lipids reduce the overall toxicity of PGL NPs, reducing potential ocular irritation.



DOPE  
vesicle



DOPE/DPPPC  
vesicle

It is well accepted that each cell type requires careful selection of optimum NP composition and fine tuning [119, 120]. The reason is that each cell type has a unique set of physiochemical characteristics, which govern the way NPs are received and processed. These factors include cell morphology, membrane charge distribution and cell-specific uptake mechanisms [73, 121]. Unlike most mammalian cells, neurons have an elongated cell shape with specialized domains (cell body, axon, and dendrites), each with domain-specific structural and surface properties [122]. Accordingly, the current work carried out optimization of the 12-7NH-12 GL-NPs, specifically for RGC-5 cells. The optimization parameters of 12-7NH-12 GL-NPs for RGC-5 cells included the NP charge, size, size distribution, helper lipid composition, order of assembly, process of manufacturing of helper lipid vesicles. For each of these parameters, the goal was to investigate how the particle's physical features are influenced, and how the transfection efficiency is affected as a result.

#### **4.2. Optimization of charge ratio of PGL<sub>DOPE</sub> NPs**

Charge ratio optimization is an important step in the development of efficient and safe non-viral gene delivery systems. In charge ratio optimization trials, the goal is to find an ideal formulation with a charge ratio that produces maximal transfection efficiency and minimal toxic effects. The  $\rho_{\pm}$  charge ratio of 12-7NH-12 GL-NPs reflects the ratio of the surfactant's cationic amine groups to the anionic phosphate groups of the DNA. The  $\rho_{\pm}$  charge ratio of a gene carrier has several implications on its performance *in vitro* and *in vivo*. Most importantly, the  $\rho_{\pm}$  charge ratio affects the physical features of gene carriers, such as  $\zeta$  potential and size [123]. The  $\zeta$  potential, which is a measure of electrostatic repulsion or attraction forces between particles in a colloidal suspension, increases with higher  $\rho_{\pm}$  charge ratios [124]. High magnitudes of  $\zeta$

potential values ( $+30 \text{ mV} < \zeta < -30 \text{ mV}$ ) are associated with better colloidal stability, and improved transfection, both *in vitro* and *in vivo* [111]. This is because gene carriers with higher  $\zeta$  potential magnitudes do not tend to aggregate or sediment, due to the high electrostatic repulsion forces between them. Accordingly, the effect on aggregation also makes the  $\rho_{\pm}$  charge ratio a determinant of particle size. The  $\rho_{\pm}$  charge ratio of NPs also influences the degree and efficiency of DNA compaction, one of the principal functions of a gene carrier. Low  $\rho_{\pm}$  charge ratio usually leads to insufficient or loose compaction of DNA, which exposes the it to various cellular degradation mechanisms [125]. Secondly, the charge ratio of a NP determines the extent of binding of NPs to the negatively charged cell membrane. With some exceptions, it is generally accepted that positively charged gene carriers bind to mammalian cell surfaces more efficiently than negative or neutral ones. Finally, the charge ratio has a direct effect on the cytotoxicity of gene carriers, since higher amounts of the cationic compaction agent is required to achieve higher  $\rho_{\pm}$  charge ratios [123].

#### **4.2.1. Size and $\zeta$ potential patterns of charge optimized PGL<sub>DOPE</sub> NPs**

$\zeta$  potential of PGL<sub>DOPE</sub> NPs, of all tested  $\rho_{\pm}$  charge ratios, were above the  $\pm 30 \text{ mV}$  colloidal stability threshold. In general, the  $\zeta$  potential of PGL<sub>DOPE</sub> appeared to peak at the 7.5:1  $\rho_{\pm}$  charge ratio condition ( $\zeta$  potential=  $+48.7 \pm 2.2 \text{ mV}$ ) before it slowly trended downwards at higher  $\rho_{\pm}$  charge ratios (Figure 27). The  $\zeta$  potential of PG complexes (before helper lipid addition) was positively correlated with the  $\rho_{\pm}$  charge ratio, as higher charge ratio formulations had higher molar concentrations of the cationic gemini surfactant. However,  $\zeta$  potential values of the PG complexes were generally below  $+20 \text{ mV}$ , indicating moderate colloidal stability. The positive  $\zeta$  potential values of PG complexes and PGL<sub>DOPE</sub> NPs are evidence of the gemini

surfactant complexation with DNA, given that DNA has a net negative charge (and  $\zeta$  potential) [126]. Additionally, the relatively high  $\zeta$  potential values of PGL<sub>DOPE</sub> NPs, following helper lipid addition was reported previously by a similar study by our group [126]. This increase in  $\zeta$  potential was explained by differences in charge distribution between the PG complexes and PGL NPs. In contrast to PG complexes, where surfactant charge may be shielded by bound water molecules, cationic charge of PGL NPs is thought to be localized and shielded within the DOPE bilayer structure [126-128].

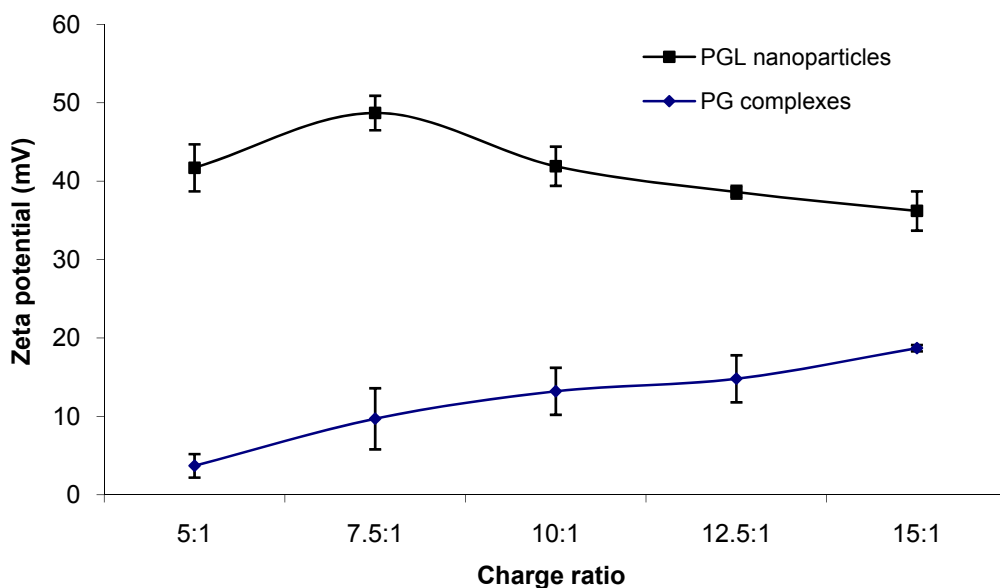


**Figure 27** Comparison of the change in  $\zeta$  potential as a function of  $\rho_z$  charge ratio in PG and PGL<sub>DOPE</sub> particles.

Combining the gemini surfactant with pDNA produced large particles, that fluctuated within a 500-1000 nm size range. This is likely due to the moderate inter-particle repulsion, reported earlier by  $\zeta$  potential analysis (Table 8). A recent study investigating the interaction between several gemini surfactants and pDNA supports the current data [129]. This study

demonstrated that when pDNA is combined with a gemini surfactant, the resulting complex undergoes a series of structural rearrangements that end with flocculation and precipitation of PG complexes. The relatively low  $\zeta$  potential and aggregation potential of PG complexes is perhaps what limits their transfection efficiency, as was shown in previous work by our group [114].

The addition of DOPE vesicles to PG complexes appeared to have compacted the large PG complexes to significantly smaller PGL<sub>DOPE</sub> NPs within a relatively narrow size range of 150 – 225 nm (Figure 28). This compaction is primarily attributed to the bilayer structure of DOPE vesicles, which was induced as a result of their preparation at pH 9. In neutral and acidic environments, DOPE assumes a relatively larger structure, due to the pH-dependent structural configuration (discussed in next section). At pH 9, DOPE's head groups gain a net negative charge, as they become deprotonated, which increases the inter-headgroup electrostatic repulsion, causing the formation of bilayer vesicles. A previous study investigated the structure of gemini-DOPE GL-NPs, using small-angle X-ray scattering (SAXS), and has shown this effect, by demonstrating an improved structural organization of PGL NPs, following the addition of DOPE vesicles prepared at pH 9 [126].

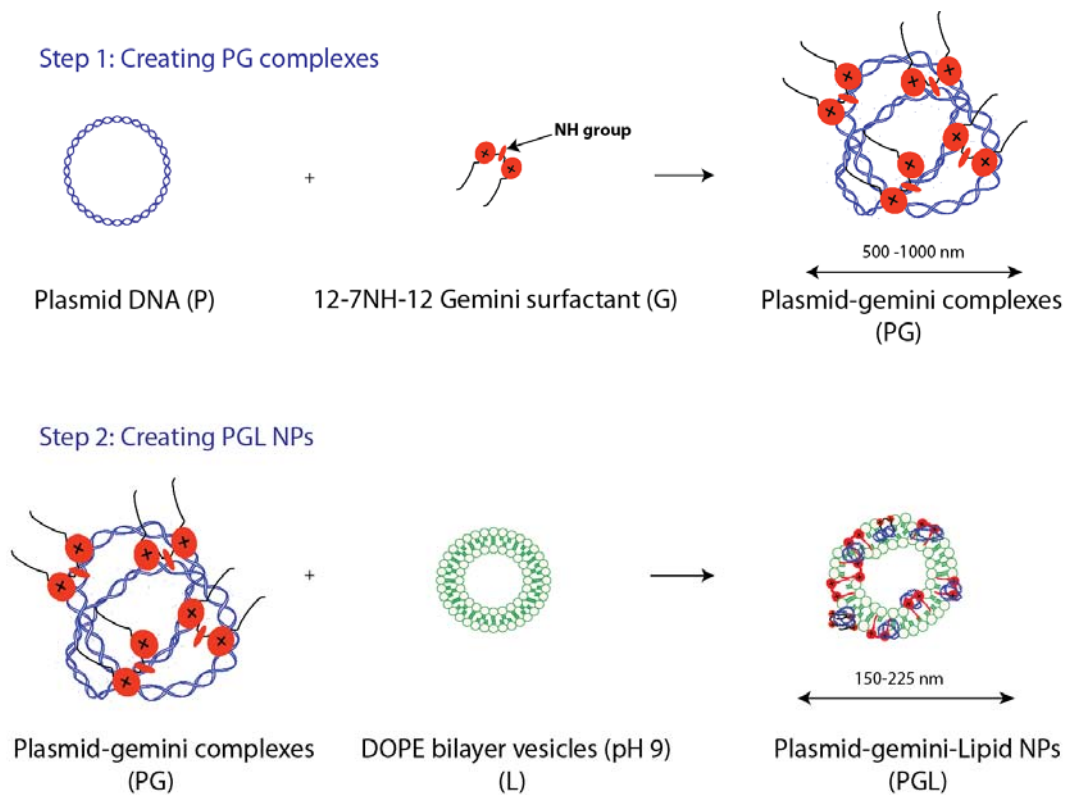


**Figure 28 Stepwise assembly of PGL NPs and the associated structural characteristics**

Combining plasmid DNA with the 12-7NH-12 gemini surfactant (step1) creates relatively large complexes, that range between 500 – 1000 nm in size. The addition of DOPE bilayer vesicles (pH 9) to PG complexes (step 2) creates organized and compacted structures that range between 150-225 nm in size. The observed compaction is a result of DOPE bilayer structure, which allows DOPE to form relatively small structures that can tightly pack PG complexes.

The size of PGL<sub>DOPE</sub> NPs appeared inversely proportional to their respective charge ratio (Table 7 and Figure 11). This inverse relationship has been reported by several characterization studies of cationic gene delivery systems [66, 130]. For gemini NPs in particular, a recent study has shown that increasing the ratio of gemini surfactant to DOPE gradually shifts the bilayer structure of DOPE/gemini bilayers, to a more compact micellar structure [131]. The interaction was attributed to the gradual solubilization of the DOPE bilayers by the gemini surfactant.

#### 4.2.2. Transfection efficiency of charge-optimized PGLDOPE NPs

Optimization of the  $\rho_{\pm}$  charge ratio of PGL<sub>DOPE</sub> NPs showed that 10:1  $\rho_{\pm}$  NPs produced the highest level of gene expression in RGC-5 cells ( $M_{TE} = 8.6 \pm 1.6 \%$ ). A recent study from our laboratory found that 10:1  $\rho_{\pm}$  12-7NH-12 PGL<sub>DOPE</sub> NPs also performed optimally in murine keratinocytes (PAM 212 cell line), compared to other tested charge ratios [114]. The current data also shows that increasing the charge ratio of PGL<sub>DOPE</sub> NPs is associated with an increase in the transfection efficiency, which reaches a maximum at 10:1  $\rho_{\pm}$  charge ratio (Figure 18). The size of the optimum 10:1  $\rho_{\pm}$  PGL<sub>DOPE</sub> NP was amongst the smallest tested, with a diameter of  $166.7 \pm 5.7$  nm. The  $\zeta$  potential of 10:1  $\rho_{\pm}$  PGL PGL<sub>DOPE</sub> NPs was  $+41.9 \pm 2.5$  mV, indicating high colloidal stability of the NPs. These findings suggest that that relatively high  $\zeta$  potential, and NP size below 200 nm, mediate a considerable level of transfection in RGC-5 cells (Figure 29).

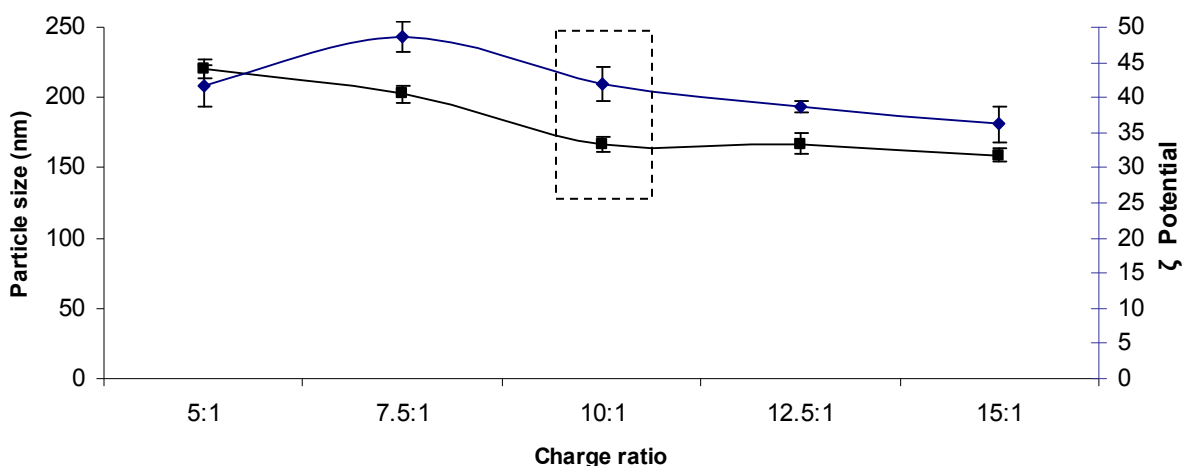


**Figure 29** Particle size (black graph) and  $\zeta$  potential (blue graph) of PGL<sub>DOPE</sub> NPs at different charge ratios.

Box indicates set of parameters of optimal transfection efficiency in RGC-5 cells



Particle size has a direct impact on the uptake mechanism of gene carriers, which in turn, impacts the respective transfection efficiency [132]. Given the size range of PGL<sub>DOPE</sub> NPs (~ 150 – 225 nm), it is predicted that PGL<sub>DOPE</sub> NPs are internalized by clathrin or caveolae-mediated endocytosis, which collectively take up particles in the 150-500 nm size range [133]. More specifically, caveolae-mediated endocytosis specifically internalizes particles between 200- 500 nm in size, while clathrin-mediated endocytosis takes up particles less than 200 nm. Indeed, a recent study has recently demonstrated that 12-7NH-12 PGL<sub>DOPE</sub> NPs are internalized by both clathrin and caveolae-mediated endocytosis in cotton tail rabbit epithelial cells, Sf 1 Ep [134] (Figure 30). The study showed that endocytosis of PGL NPs was significantly reduced, following inhibition of the two endocytotic mechanisms. Further, endocytosis was inhibited to a similar extent, after inhibition of caveolae-mediated endocytosis alone, indicating a primary role of this endocytotic mechanism in uptake of PGL<sub>DOPE</sub> NPs. These findings can be extended to the current results, since RGC-5 cells have been shown to employ both clathrin and caveolae-mediated endocytosis for particle uptake. The predicted involvement of both uptake mechanisms in the internalization of PGL<sub>DOPE</sub> NPs is likely a result of the heterogeneity of particle sizes (Table 7). This size heterogeneity is not unique to gemini NPs; several studies have reported similar observations, especially for cationic carriers [135]. In fact, later discussion will demonstrate that such heterogeneity may improve transfection efficiency, since a heterogeneous size distribution may activate a wider range of uptake mechanisms, compared to a homogenous one.

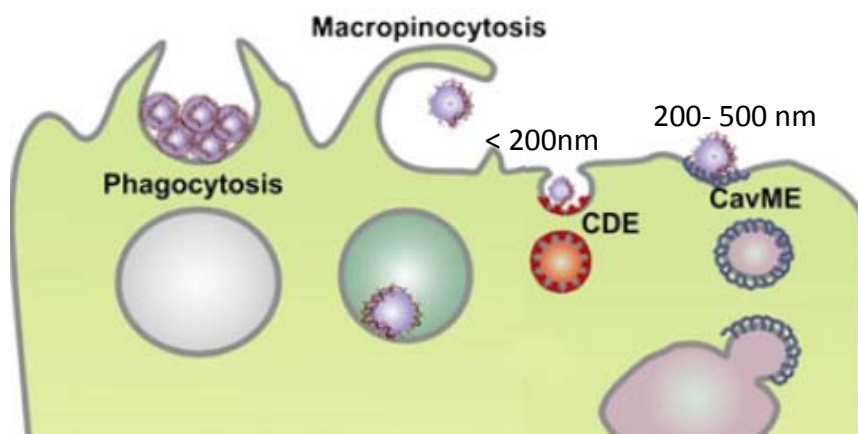


**Figure 30** A schematic diagram of the common cellular uptake mechanisms involved in uptake of NPs. The caveolae-mediated endocytosis (CavME), and the clathrin-mediated endocytosis (CDE) have been shown to have a primary role in the uptake of PGL<sub>DOPe</sub> NPs. CavME internalizes particles that range between 200-500 nm in size, while CDE uptakes particles that are smaller than 200 nm. Other mechanisms, including phagocytosis, and macropinocytosis are also potential mechanisms for uptake of similar non-viral gene carriers. The type of mechanism involved in a NP uptake depends primarily on the physical and chemical features of the gene carrier, including particle size, charge, and surface chemistry. *Adopted with permission and modified from Vercauteren et al [136].*

Reports about the relationship between size of gene carriers and their respective transfection efficiency have been somewhat conflicting. While some studies have shown increased transfection efficiency with smaller carrier size [137, 138], others showed an inverse relationship [139, 140], or did not find any association [141, 142]. Intuitively, smaller complexes are expected to navigate through the various barriers of the cellular environment and reach the nucleus more easily, as was demonstrated by some studies [80]. Similarly, the relationship between  $\zeta$  potential and transfection success has been a subject of debate, with some studies reporting a relationship between  $\zeta$  potential and transfection efficiency [143], while others reporting none [144]. The reason for this discrepancy is that analyzing a single variable at one time is often not sufficient to understanding a gene carrier's performance in a given setting.

The emerging literature suggests that there is an interaction between particle size,  $\zeta$  potential, cell type, and the chemical nature of compaction agent, which collectively determine the success of a gene carrier in a particular environment [145, 146].

### **4.3. Optimization of helper lipid composition**

Helper lipid vesicles are widely used in gene delivery systems to increase their transfection efficiency by improving DNA compaction, cell entry, and endosomal escape [147, 148]. These functions have been shown to be highly dependent on the structure of lipid in the lipid vesicle in question. In fact, certain structures have been shown to favor transfection, while others have been shown to hinder it [149]. A lipid vesicle structure is determined by its physical and chemical features, including the charge and the size of the head group, the length and the saturation levels of the tail, and many others (see review by [135]). Further, the pH at which the vesicles are prepared influences the physicochemical characteristics of lipids to further impact their molecular arrangement. For example, DOPE has a 'conical' molecular shape at neutral or mildly acidic pH; in the sense that its head group is smaller than the cross section area of its alkyl tails [150]. Similar to its phosphatidylethanolamines (PE) counterparts, DOPE's conical shape inclines it to assemble into circular subunits, which in turn, form long cylindrical lipid structures stacked on one another (Figure 31 A). This structural form, which is known as the inverted hexagonal structure ( $H_{II}$ ), lends DOPE the ability to fuse with cellular and lysosomal membranes, allowing it to achieve effective cell entry and endosomal escape, respectively [149, 151, 152]. While this structure may improve the gene transfer efficiency inside the cell, it does not offer the compaction needed to tightly pack DNA during the NP preparation process. Accordingly, DOPE vesicles are induced to assume the bilayer structure, by preparing them at

pH 9, allowing for more compaction and retention of DNA. The subsequent deprotonation of DOPE's headgroups increases the inter-headgroup repulsive interaction, which allows them to pack as semi-cylindrical subunits, forming bilayer structures (Figure 30-A). The pH-dependent fusogenic character of DOPE, while advantageous, predisposes NPs to fuse with one another, or with surrounding biological molecules [153]. This can lead to the aggregation or precipitation of NPs, which could either reduce or eliminate their gene transfer capacity. One way to improve the stability of DOPE lipid vesicles is to prepare them in combination with a lipid that exhibits a more stable structure. An example of these lipids is a category called phosphatidylcholines (PC), whose molecules assemble into what is known as lamellar structures ( $L_{\alpha}$ ). PC lipids have a more symmetrical molecular shape compared to PE lipids, with a comparable headgroup size to the tail cross sectional area, at neutral pH (Figure 30-B). Accordingly, PC molecules tend to form stacked  $L_{\alpha}$  bilayers, which do not exhibit fusogenic behavior (Figure 30-B). The challenge is to find the ratio the PE: PC that would improve NPs' stability, while maintaining its fusogenic behavior. In the current study, the helper lipid, DPPC was used to prepare DPPC lipid vesicles, and in combination with DOPE at varying ratios (25 %, 50%, and 75%) to achieve this goal.

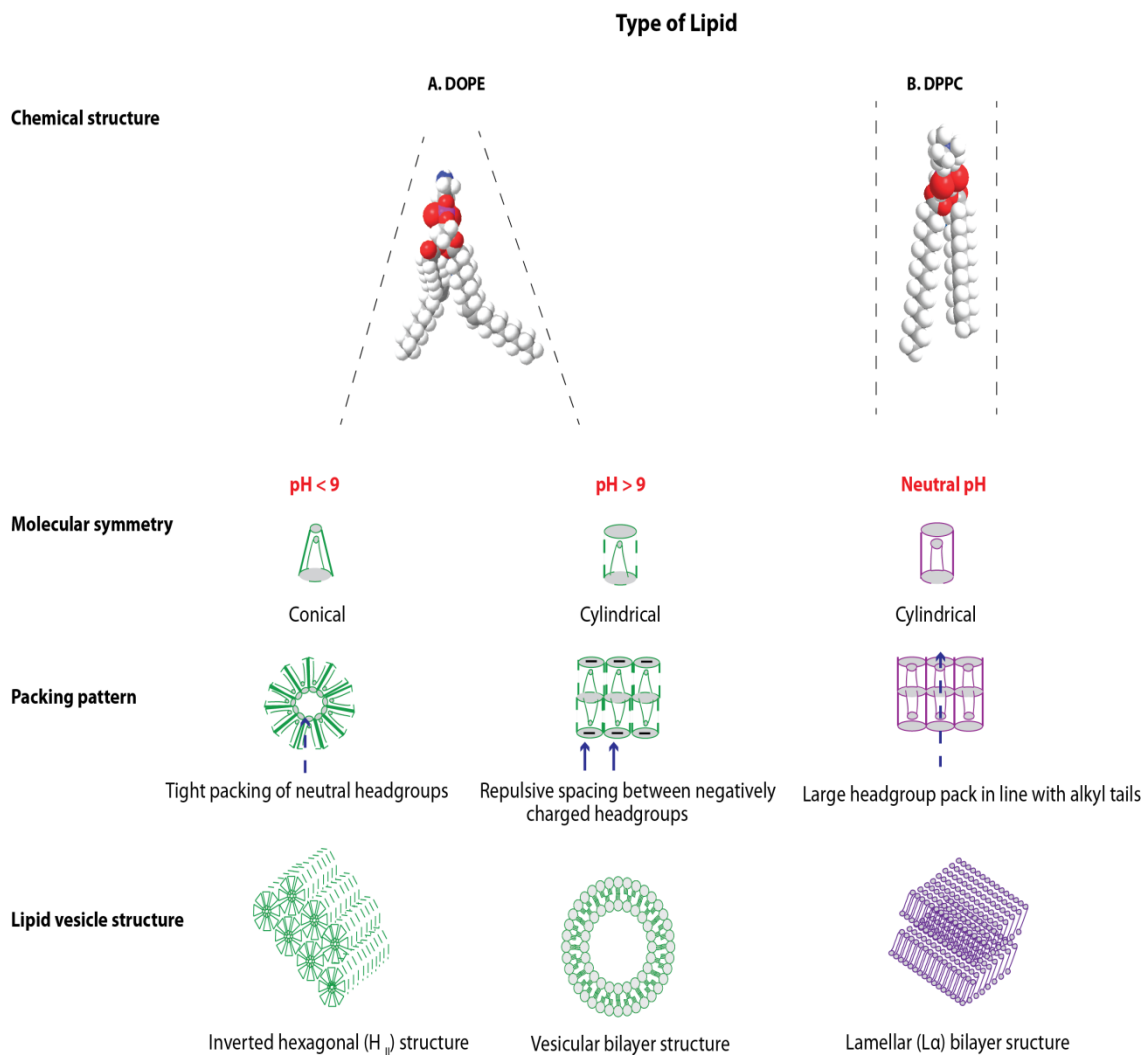


**Figure 31 Structure and symmetry of DOPE and DPPC lipids and their vesicular structural properties**

At neutral pH, the head group of DOPE lipid vesicles is smaller than the area of its tail cross section, which inclines them to assume the hexagonal structure (H<sub>II</sub>). Preparing DOPE vesicles at pH 9 allows them to pack in more compact vesicular bilayer structures. DPPC has a naturally cylindrical molecular symmetry at neutral pH, allowing it to pack lamellar bilayer vesicles. Physicochemical characterization of PGL NPs as a function of DPPC ratio in helper lipid vesicles.

Several studies have investigated the characteristics of mixed PE:PC lipid and the effect of the ratio of PE: PC on the resulting bilyaer structure of NPs [154-156]. These studies indicate that PE:PC mixtures typically exhibit an ideal mixing behavior, in the sense that there is a homogenous lipid distribution within the structure of lipid vesicle [154]. Additionally, it was

demonstrated that the bilayer structure of a PE:PC mixtures is be mainly determined by the preferred structure of the lipid available in higher ratio [155, 157]. Accordingly, we may predict that PGL<sub>DOPE</sub> NPs form vesicular-shaped NPs (Figure 32-A) at pH 9, while those prepared at DOPE: DPPC mixtures containing > 50% DPPC (PGL<sub>F4</sub> NPs) will exhibit a mainly lamellar ( $L_{\alpha}$ ) structure (Figure 32-B). Interestingly, at neutral or acidic pH (such as that of the endosome) PGL<sub>DOPE</sub> NPs exhibit mixed structural characteristics, including the H<sub>II</sub> among others [158]. This polymorphic character is thought to aid in increased transfection performance, promoting better cytosolic DNA release [158].

1. Schematic diagram    2. Electron microscopic image

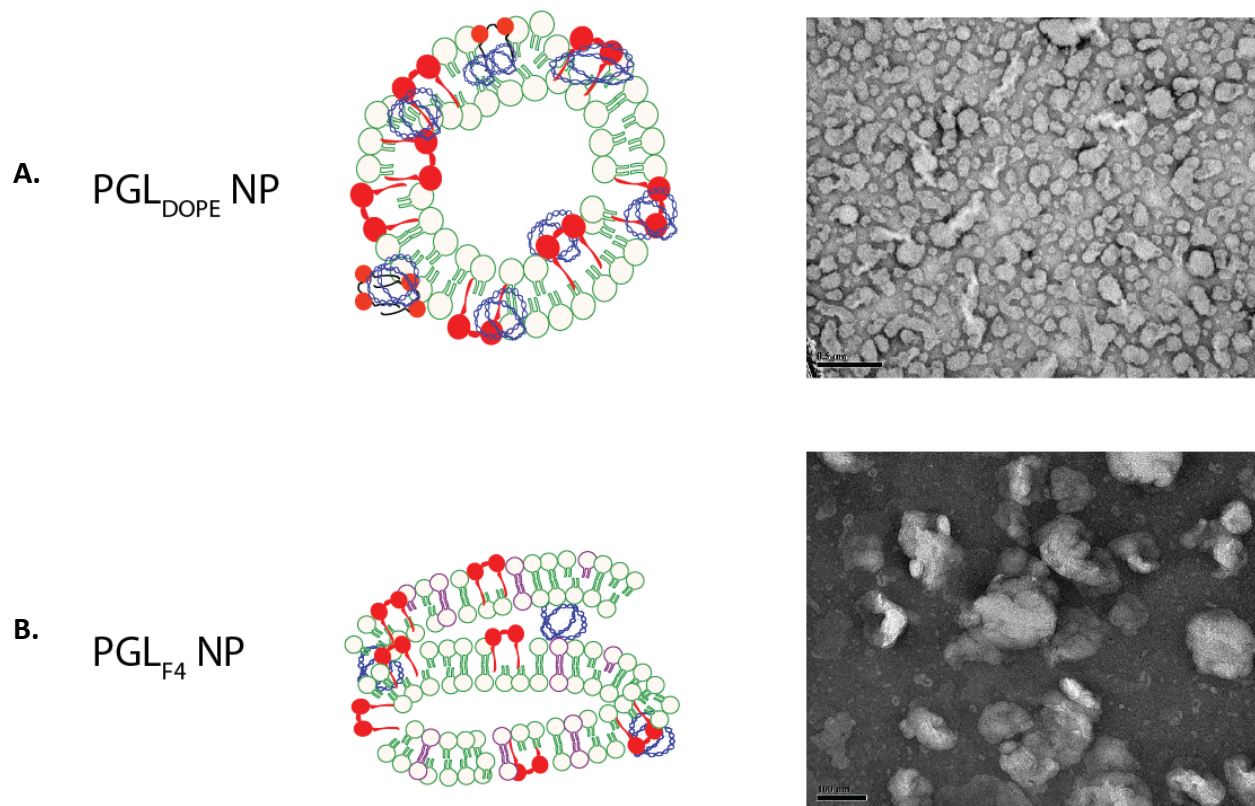


**Figure 32**    **Schematic diagrams and electron microscopic images of PGL NPs, assembled with different helper lipids compositions**

PGL<sub>DOPE</sub> NPs have a vesicular structure (A1), when assembled with DOPE at pH 9. PGL<sub>F4</sub> NPs have a stacked lamellar structure (A2), due to the DPPC-rich F4 formulation. The different structural arrangements of these NPs are a result of the assembling kinetics of the helper lipid vesicles. NPs were prepared by *Dr. M. El-Sabahy* and *electron microscopic images were taken by Dr. M. Foldvari*.

#### 4.3.1. Effect of helper lipid composition on transfection efficiency

Assessment of transfection efficiency of NPs assembled with DPPC and DOPE/DPPC co-lipids appeared dependent on the ratio of the DPPC in helper lipid vesicles. The highest transfection efficiency achieved, as a result of DPPC incorporation, was mediated by PGL<sub>F4</sub> NPs ( $M_{TE} = 5.2 \pm 1.6\%$ ), containing 75% DPPC and 25% DOPE. The role of PC lipids in improving the efficiency of DOPE-mediated transfection is a debatable subject. Some studies reported a reduction in the transfection efficiency, as a result of PC lipid introduction [159, 160], and attributed this due to a less than favorable PE: PC lipid vesicle structure. The resulting structure, which was shown to be a primarily lamellar one, was believed to reduce NP's ability to fuse with cell and endosomal membranes, which would reduce the rate of cell entry and endosomal escape, respectively. On the other hand, other studies demonstrated that PC lipid's L<sub>α</sub> structure is capable of mediating high transfection efficiencies, similar to those mediated by PE lipids [161, 162]. These studies argued that since L<sub>α</sub> NPs are less susceptible to forming large aggregates, their uptake is favored by cells, whose main uptake mechanism favors uptake of smaller particles, such as Chinese Hamster Ovary (CHO) cells [161]. Lin et al. demonstrated that this discrepancy can be explained by the variability of the charge density ( $\sigma_m$ ) in NPs containing PC lipids.  $\sigma_m$  is defined as the average charge per unit area of a NP surface, a parameter that was proposed to play a critical role in the transfection efficiency and toxicity of NPs [162, 163]. Lin et al. proposed that the efficiency of L<sub>α</sub> NPs can be drastically improved, given that their  $\sigma_m$  is adjusted to exceed threshold value of  $1.04 \cdot 10^{-2} e/\text{\AA}^2$ , which was achieved by optimizing the neutral lipid: cationic lipid ratio.



To test whether the hypothesis proposed by Lin et al. can explain the current data, the  $\sigma_M$  values for 10:1 PGL NPs were calculated as a function of the helper lipid composition, using the equation [164] below:

$$\sigma_m = \frac{eZN_{cl}}{N_{nl}A_{nl}+N_{cl}A_{cl}} \quad (\text{Equation 1})$$

where Z is the valency (+2) of the gemini surfactant,  $N_{cl}$  (0.23) and  $N_{nl}$  (0.73) are the calculated molar fractions of the gemini surfactant and the DOPE, and  $A_{cl}$  ( $156 \text{ \AA}^2$  [106]) and  $A_{nl}$  ( $46 \text{ \AA}^2$  [165]) are the headgroup area of the gemini surfactant and DOPE, respectively; equation by Ewert et al [164]. Given that there are two neutral lipids,  $A_{nl}$  values were calculated by multiplying each lipid  $A_{nl}$  with the corresponding molar fraction of the lipid.

**Table 16**  $\sigma_m$  values of PGL NPs assembled with DOPE/DPPC and DPPC helper lipid vesicles

Lipid formulation	Composite $A_{NL}$ value ( $\text{\AA}^2$ )	$\sigma_M$ ( $10^{-2} e/\text{\AA}^2$ )
F2: 75% DOPE – 25% DPPC	50.2	2.12
F3: 50% DOPE- 50% DPPC	54.5	2.03
F4: 25% DOPE-75% DPPC	58.7	1.95
F5: 100% DPPC	62.9	1.88

$\sigma_m$  calculations showed that PGL NPs assembled with DPPC and DOPE/DPPC lipid vesicles exceed the threshold value of  $1.04 \cdot 10^{-2} e/\text{\AA}^2$  (table 15). Therefore, the model by Lin et al. alone does not provide a clear explanation for the variability of transfection efficiency mediated by DPPC and DOPE/DPPC helper lipid vesicles. Perhaps the high predicted stability of the DPPC-rich F4 vesicles, in combination with PGL NP general polymorphic structure can collectively explain the enhanced transfection. Further structural characterization of DOPE/DPPC lipids are needed to confirm these predictions.

### 4.3.2. Optimization of order of assembly

Changing the order of assembly of multi-component gene carriers has been shown to affect their physical features and transfection efficiencies [166]. While PG complexes and PGL NPs were previously the focus of physical characterization, here we investigate those of GL vesicles and GL+P NPs. The  $\zeta$  potential of GL vesicles was less positive than that of GL+P NPs, which is a direct result of the presence of the anionic pDNA in GL+P NPs. This suggests that negatively charged pDNA has electrostatically bound to the cationic gemini surfactant. Further, in comparison to the  $\zeta$  potential PGL<sub>DOPE</sub> NPs ( $41.9 \pm 2.5$  mV), GL<sub>DOPE</sub>+P NPs had a lower  $\zeta$  potential ( $26.4 \pm 0.4$  mV). Given that both of these two NPs are identical in composition, this difference in  $\zeta$  potential is likely a result of the difference in component arrangement within the NPs. In the original PGL<sub>DOPE</sub> NPs, the cationic surfactant was brought in direct contact with pDNA within the PG complexes, before adding the helper lipid vesicles. This order of assembly probably led to maximal pDNA complexation, via attractive electrostatic interactions between pDNA and the gemini surfactant. In the alternative order of assembly, binding of the surfactant to pDNA was likely less direct, leading to a lower net positive charge. This is why the  $\zeta$  potential values of GL<sub>DOPE</sub>+P NPs were less positive than their PGL<sub>DOPE</sub> NPs.

Changing the order of assembly also had an effect on the size of NPs. GL vesicles exhibited a lipid-dependent size change, following addition of pDNA. More specifically, GL<sub>DOPE</sub>+P became  $\sim 25$  nm smaller, following pDNA addition, while GL<sub>F4</sub>+P NP became  $\sim 100$  nm larger. Simulation and spectroscopic studies of mixed cationic-neutral liposomes have provided useful models for understanding the structural characteristics and sizes of cationic liposomes, such as GL vesicles [167, 168]. These studies reported that the size of mixed cationic-neutral

liposomes is mainly determined by two factors: net electrostatic interaction between the head groups of mixed liposome, in addition to the equilibrium orientation of the lipid head groups in reference to the bilayer surface (parallel vs perpendicular) [169]. Lipid head groups consist of a single dipole, with a spatially fixed negative charge, acting as a pivot point, and a relatively mobile positive end. As a general rule, higher repulsive interactions between head groups causes an increase on the lipid's cross sectional area, which leads to a larger vesicle size. Similarly, parallel head group orientation leads to 'stretching' of the vesicle's bilayer membrane, due to the lateral shear forces that result from steric (crowding) interactions of the head groups.

The reduced size of  $GL_{DOPE+P}$  NP, compared to  $GL_{DOPE}$  vesicle, is likely a result of a partial neutralization of the cationic repulsive forces between the surfactant head groups, following pDNA addition. This partial neutralization likely lowered the lateral repulsive forces that contributed to the relatively larger size of GL vesicles. On the other hand, the increased size of  $GL_{F4+P}$  NP, compared to  $GL_{F4}$  vesicles is a result of a more complex interaction, involving the bulky DPPC head groups, in addition to the aforementioned electrostatic interaction factor. The size of  $GL_{F4}$  vesicles was relatively smaller, probably because of the perpendicular orientation of DPPC head groups, in reference to the bilayer surface. This was a result of the electrostatic attractive force between the gemini surfactant head group and the negative end of DPPC's dipole head group, at the surface of the bilayer vesicle. This resulted in 'pulling' of the negative dipole ends towards the adjacent gemini surfactant head groups, causing the positive dipole ends of DPPC head groups to 'rotate' in the opposite direction, assuming a nearly vertical orientation in reference to the bilayer's surface (Figure 33). This cationic-dipole interaction has

been proposed to reduce vesicle size, via the formation of cation-dipole clusters, that shrinks the cross sectional area of the bilayer vesicle, and by reducing the sterics between the mobile positive dipole ends [170]. The increased size of  $GL_{F4}+P$  NPs was likely a result of the reduced cation-dipole clustering, following charge shielding of the surfactant's head groups, as a result of pDNA addition. Additionally, a strong dipole-dipole steric repulsion is expected to have taken place between the bulky DPPC head groups, following pDNA addition, as a result of the reduced clustering effect (Figure 33). This likely forced the dipoles to 'tilt' towards the bilayer membrane, to minimize repulsion, which would have increased DPPC's cross section area. These observations show that effective stabilization of intra-NP repulsive interactions, by optimizing the order of assembly, is necessary to achieve compact NPs.

### DOPE-DPPC GL vesicles ( $GL_{F4}$ )

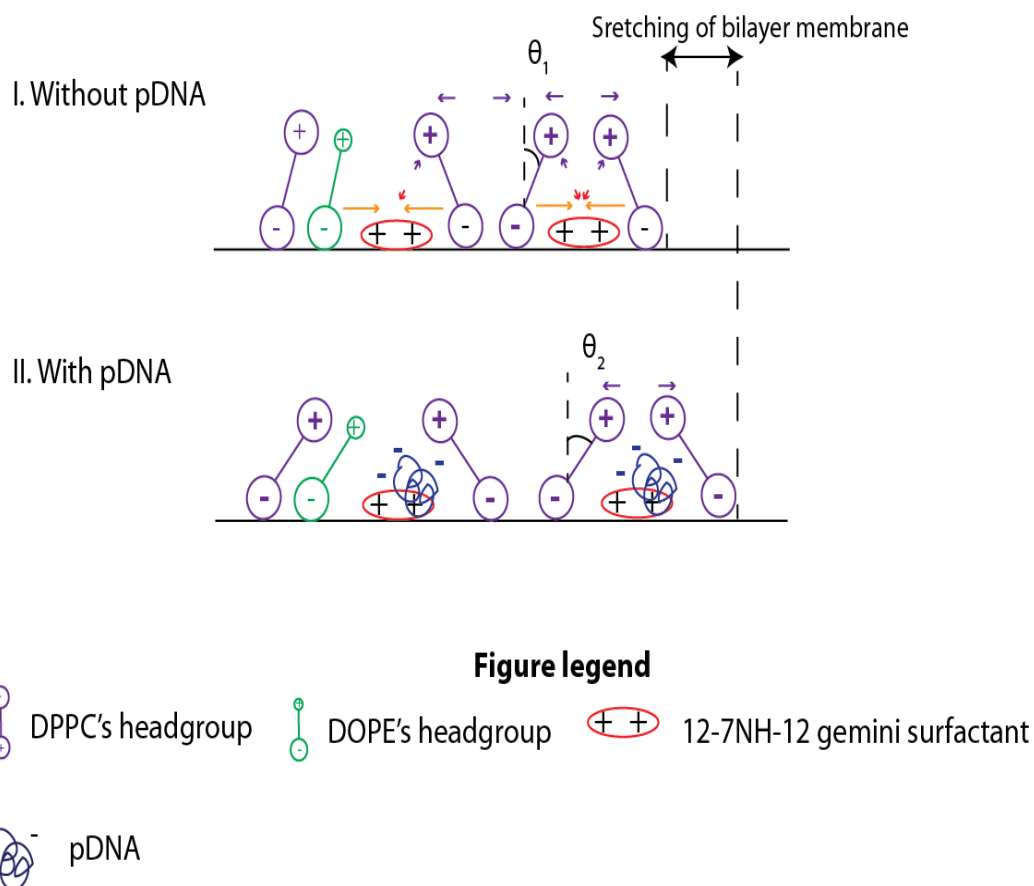


**Figure 33**      **Schematic illustration of dicationic-neutral mixed lipid membrane model**

The size of mixed cationic liposomes is determined primarily by electrostatic interactions between the cationic and neutral headgroups, and the orientation of the  $P^- - N^+$  dipole. Before the addition of pDNA, GL vesicle's size is kept at a minimum due to the cation-dipole attractive interaction (orange arrow). This in effect orients the dipole headgroups towards in a nearly perpendicular angle with the bilayer's surface. The addition of pDNA reduces the clustering of dipoles around the surfactant headgroup and increases the cross sectional area of the lipid. This increase is mediated by the parallel orientation of DPPC head groups, which causes stretching of the bilayer membrane, due to steric interactions.

#### 4.3.3. Effect of order of assembly on transfection efficiency

Changing the order of assembly (PGL vs GL+P) had a significant effect on the transfection efficiency of NPs.  $GL_{DOPE}+P$  and  $GL_{F4}+P$  NPs mediated a transfection efficiency of  $4.6 \pm 3.0\%$  and

2.1 ± 0.3 %, respectively. This was significantly lower than the transfection efficiency of PGL<sub>DOPE</sub> and PGL<sub>F4</sub> NPs. Based on the particle characterization investigation, differences in the degree of pDNA compaction may account for this reduced transfection efficiency. Combining pDNA with gemini-lipid mixtures may have yielded reduced pDNA complexation, since a proportion of the gemini surfactant's cationic binding may have been blocked by the surrounding lipid molecules [171].

#### **4.3.4. Optimization of NP manufacturing technique**

Preparation of NPs by high shear homogenization (frequently used for liposome production) is advantageous, as it produces particle population with high reproducibility and size uniformity. However, high shear (sonication and extrusion through polycarbonate membrane) can damage DNA either by converting the active supercoiled isoform to non-active open circular isoform [172], or by complete degradation [173]. Therefore, the complete NP with all its components, including the plasmid, cannot be subjected to high shear forces. In our case, we decided to prepare the helper lipid vesicles only by high-pressure homogenization and combine it with PG complexes to create the PGL<sub>MF</sub> NPs. Preparation of helper lipid vesicles by microfluidization as opposed to by thin-film method would provide a more feasible scale-up option of NP components for future studies. Microfluidization of helper lipid vesicles produced NPs that were generally larger than those assembled with thin-film helper lipid vesicles. PGL<sub>MF-DOPE</sub> and PGL<sub>MF-F4</sub> NPs were approximately 130 nm and 100 nm larger, respectively, than their original equivalents (original method). The  $\zeta$  potential of PGL<sub>MF-F4</sub> NPs (+33.5 ± 2.9mV) was similar to the PGL<sub>F4</sub> NPs, while PGL<sub>MF-DOPE</sub> NP  $\zeta$  potential (+9.2 ± 2.1 mV), was significantly lower

than that of PGL<sub>DOPE</sub> NPs. The large size of helper lipid vesicles produced by microfluidization and low  $\zeta$  potential values are possible explanations for this size difference.

#### **4.3.5. Effect of manufacturing technique of helper lipid vesicles on transfection efficiency**

Assembling NPs with microfluidized lipid vesicles was shown to significantly improve the transfection efficiency of PGL NPs. 10:1  $p\pm$  PGL<sub>MF-DOPE</sub> and PGL<sub>MF-F4</sub> NPs mediated a transfection efficiency of  $12.3 \pm 1.0 \%$  and  $14.5 \pm 1.4\%$ , respectively. These values are both significantly higher than those achieved by the equivalent original PGL NPs, which were prepared by thin film lipid vesicles. Particle characterization of PGL<sub>MF</sub> NPs showed that they had higher particle size ( $> 200$  nm), compared to those assembled with thin film lipid. This data implies that PGL<sub>MF</sub> NPs would most likely be internalized via the caveolae-mediated endocytosis, the primary mechanism in uptake of PGL<sub>DOPE</sub> NPs. More specifically, PGL<sub>MF-DOPE</sub> NP entry into RGC-5 cells is expected to have been highly dependent on the caveolae-mediated endocytosis, which processes particles of 200- 500 size range. The clathrin-mediated pathway, which takes up particles below 200 nm in size, was likely involved in the uptake of PGL<sub>MF</sub> NPs, but to a lesser extent, compared to its role in the of uptake of traditional PGL<sub>DOPE</sub> NPs, whose average size was below 200 nm. Thus, the hypothesized involvement of an additional uptake mechanism is thought to underlie the improved transfection efficiency of PGL<sub>MF</sub> NPs.

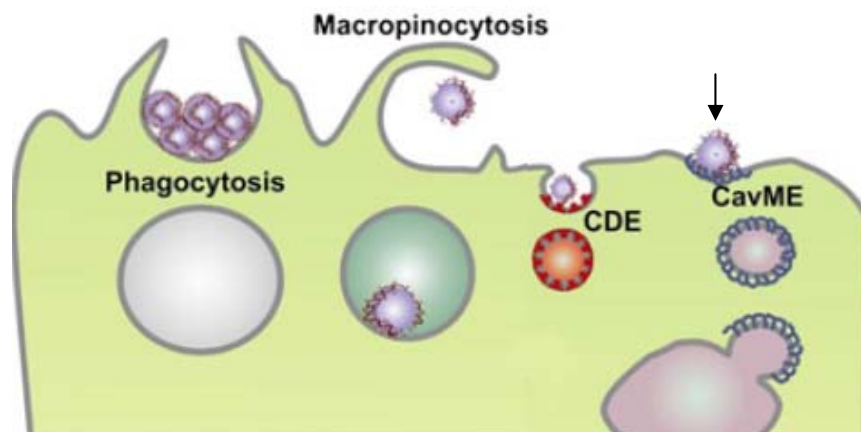


**Figure 34** Primary mechanism involved in uptake of 10:1  $\rho_{\pm}$  PGL<sub>MF</sub> NPs in RGC-5 cells

10:1  $\rho_{\pm}$  PGL<sub>MF-DOPE</sub> and PGL<sub>MF-F4</sub> NPs had an average size > 200 nm, which suggests that the CavME was primarily involved in their uptake, given CavME's specificity to uptake of particles above 200 nm. The primary role of this mechanism is thought to be the reason for PGL<sub>MF</sub> NPs superior transfection efficiency. Additionally, PGL<sub>MF</sub> NPs had several of their physical parameters optimized, over several stages of refinement and fine tuning. *Adopted with permission and modified from Vercauteren et al [136].*

Finally, PGL<sub>MF-DOPE</sub> NPs mediated the highest transfection, yet had lower  $\zeta$  potential values than their original equivalent. This variability in  $\zeta$  potential brings into question the importance of  $\zeta$  potential as an individual determinant of transfection success. Perhaps, efficient transfection can be achieved by surpassing a minimal  $\zeta$  potential threshold; beyond which, no difference in efficiency is observed.

#### 4.4. Assessment of toxicity of PGL NPs in RGC-5 cells

Toxicity screening showed that PGL<sub>DOPE</sub> NPs with charge ratios up to 12.5:1  $\rho_{\pm}$  were well tolerated by RGC-5 cells. Cells did not show signs of toxicity (close to 100% viability by Presto Blue assay) following a 12 hour incubation period with PGL NPs at these charge ratios. RGC-5 cells treated with PGL NPs at charge ratio range of 12.5:1 – 20:1 showed a gradually increasing toxicity, which reached a maximum at 20:1  $\rho_{\pm}$  charge ratio, where approximately 75% of the



cells were viable at the end of the incubation period. PGL NPs prepared with DPPC and DOPE/DPPC lipid vesicles were highly tolerated by RGC-5 cells as well, with 100% viability measurements for all four types of lipids and PGL NPs (Figure 19). Exposure of RGC-5 cells to the gemini surfactant and PG complexes was the most toxic, with toxicity levels increasing with higher surfactant concentrations (Figure 18). The toxicity of PG complexes at various charge ratios did not significantly differ from that of the gemini surfactant alone.

The high viability of RGC-5 cells following treatment with PGL NPs highlights the protective role of the helper lipids (DOPE and DPPC) in reducing the overall toxicity of the PGL NPs. This effect is especially pronounced at the 20:1  $\rho_{\pm}$  charge ratio, where the viability of RGCs treated with PGL NPs treated condition is several folds higher than those treated with the gemini surfactant or PG complexes. The role of neutral lipids in reducing toxicity of gene delivery systems was observed in several studies investigating liposome-mediated cationic gene delivery systems [174-176]. The neutral charge of these helper lipids helps keep the overall charge density of NPs at a sufficient minimum, which has been shown to significantly reduce their toxicity profile [163]. The harmful effects of high charge density gene carriers include damage to the cellular membranes and functional enzymes, vacuolization of the cytoplasm and cell shrinking [177, 178]. These toxic affects are often seen with liposomes containing cationic lipids, such as cholesterol derivatives that contain highly charged head groups [179].

#### **4.5. Effect of NP treatment on neurite outgrowth**

In order to confirm the functionality of BDNF produced by transfected cells prior to *in vivo* experiments, we carried out neurite outgrowth assays in RGC-5 cells using the two optimized NPs, 10:1  $\rho_{\pm}$  PGL<sub>DOPE</sub> and PGL<sub>F4</sub> NPs and Lipofectamine Plus, each carrying the BDNF

gene in the bicistronic plasmid pCMV6-AC-GF. Transfection of RGC-5 cells with PGL<sub>DOPE</sub>, PGL<sub>F4</sub> NPs, and Lipofectamine lipoplexes did not induce a significant outgrowth response. Although Lipofectamine mediated higher transfection efficiency, compared to PGL NPs, and was hence expected to express a higher amount of BDNF, it is likely that it did not achieve the concentration level required to stimulate neurite outgrowth. The hrBDNF protein was used as a control in RGC-5 cells, to compare its effect on neurite outgrowth to that induced by NPs. It is important to note that the neurite outgrowth 'concentration curve', generated using BDNF protein in the range of 50-200 ng/mL, did not show a linear relationship. While 50 ng/mL of BDNF stimulated neurite outgrowth, neurite outgrowth plateaued at 100 ng/mL concentration and above. Despite the non-linear nature of these results, they are in line with findings from related studies that reported maximum neurite outgrowth, using a BDNF concentration between 20 ng/mL and 50 ng/mL, in cultured spiral ganglion cells and primary pig RGCs, respectively [180, 181]. The activity of NTFs in neuronal cells is dependent on their specific binding to their respective high affinity Trk receptors, which are shared by more than one NTF in some cases [182]. Increasing the concentration of a certain NTF beyond a certain level, does not necessarily enhance neurite growth, since excessive binding of one NTF to a common receptor prevents equally important NTFs from binding [183]. Additionally, all NTFs also commonly bind to receptors that are believed to enhance their binding affinity. An example of these receptors is the p75 receptor [184]; increasing BDNF concentration beyond its normal level has been shown to reduce NGF's access to bind to the p75 receptor in DRG culture. These factors ultimately result in inhibition of neurites' growth.

Most of the studies that investigated neurite outgrowth following induction of BDNF expression were completed using CNS cell models, and very few of these employed non-viral gene delivery systems. One study investigated the individual effect of inducing BDNF and NGF expression on the neurite outgrowth, in a rat hippocampal explant, using gold nanoparticles. The authors reported that BDNF expression, and not NGF expression, induced a significant increase in the number of axonal branches and basal dendrites in the neuronal explant culture [185]. Another study investigated this relationship by optimizing the transfection reagent Lipofectamine 2000™ to deliver the NGF gene to dorsal root ganglia (DRG), extracted from chicken embryo. The authors report that transfection efficiency of lipoplexes was directly proportional to the concentration of NGF in the culture media, and consequently the extent of neurite outgrowth of DRG [186]. Finally, the effect of the transfection technique investigated in by one study in relation to the level of observed neurite outgrowth on DRG, which showed that the electroporation method causes an overall reduction in the average neurite growth [187]. This effect was attributed to the structural disturbance of the neurons' membrane, which is induced to allow pDNA entry to the cell [188].

The BDNF gene was used in the current study, mainly as candidate therapeutic for glaucoma treatment. However, to achieve clinically significant ON regeneration, especially in glaucoma models, targeting other neuronal growth mechanisms may be needed, not just the BDNF-dependent one. For example, several studies have demonstrated that combinations of NTFs and other growth factors, yield significantly better outgrowth outcomes, compared to the use of a single NTF [189, 190]. This is because each neuronal subpopulation (RGCs, or glia) are most responsive to a specific NTF type, due to inter-subpopulation differences in the Trk

receptor expression patterns [191-193]. Additionally, despite the many benefits of glaucoma NTF therapy in general, several considerations must be addressed. Following ON injury, the number of Trk receptors in RGCs rapidly decreases, which leads to a reduction to the RGC sensitivity to NTF neuro-protective and neuro-regenerative effects [194]. Additionally, sustained NTF application has been shown to directly downregulate TrkB expression in RGCs, leading to a similar loss of sensitivity to NTFs [195]. Accordingly, NTFs' protective effects are limited by the scarcity of Trk receptor in RGCs, following ON injury, which explains the often observed temporary effects of NTFs [31]. Cheng et al. addressed this challenge by increasing the expression of TrkB receptors using a viral vector, in combination with exogenous BDNF treatment, in a CNS injury model. The authors reported that this treatment significantly increased the survival rate of RGCs, compared to treatment with BDNF alone [196].

Extrapolating *in vitro* neurite outgrowth responses to *in vivo* glaucoma settings must be done with caution, due to the inherent environmental differences between the two settings. Unlike *in vitro* conditions, *in vivo* conditions of the ON and retina highly inhibit neuronal outgrowth. These inhibitory factors include macrophage-mediated phagocytosis [197], scar tissue formation [198], immune system activation [199], myelin-induced inhibition [200] and several others. Accordingly, inducing neurite outgrowth *in vitro*, should preferably be undertaken in environments that resemble *in vivo* conditions, as closely as possible. Similarly, the physiology of cells or tissues, employed in glaucoma models, should also reflect *in vivo* conditions, if possible. Of course, animal models, neuronal tissue explants and primary cells provide the most accurate physiological simulations; however, their use in early optimization stages of research is not always practical, due to the intensive labor involved in their use and

related ethical concerns. On the other hand, neuronal cell lines, such as RGC-5, are significantly easier to maintain and handle. However, they have been shown to less closely resemble native RGCs, than organ-derived cells, primarily due to their susceptibility to genetic mutations over time [98, 201].

#### **4.6. Assessment of corneal permeation and toxicity of PGL NPs in HCE tissue**

The cornea is a multi-layered structure, whose thickness varies from 500  $\mu\text{m}$  in its central region, to approximately 700  $\mu\text{m}$  in its periphery [202]. The corneal epithelial layer is approximately 50  $\mu\text{m}$ , while the stroma, which is approximately 450  $\mu\text{m}$  thick [203], constitutes the majority of the corneal thickness. Although there are several potential pathways for trafficking of NPs/therapeutic agents to the retina, following topical administration, transcorneal permeation is considered the primary one. Generally, topically administered therapeutics can achieve transcorneal permeation via two potential routes: 1) the intercellular route, and the intracellular route. Trafficking through the intracellular pathway requires therapeutics to transverse the epithelium, stroma and the endothelial layers by directly passing through cells in the multi-layered cornea (Figure 35). Non-specific gene delivery or expression, in non-target cells, is the main disadvantage of this route. Generally, lipophilic therapeutics have more success permeating through this pathway than hydrophilic ones. The intercellular pathway requires the passage of therapeutics through the tight junctions and desmosomes of the corneal epithelium, which can be as narrow as 2 nm [204, 205]. Accordingly, this route significantly restricts the passage of macromolecules, allowing mainly solutes and other small molecules to pass through [206]. Generally, the predicted transcorneal pathway of a topically

applied drug is determined by its chemical and physical features, include size, lipophilicity, and charge, which are all factors that highly depend on pH as well.

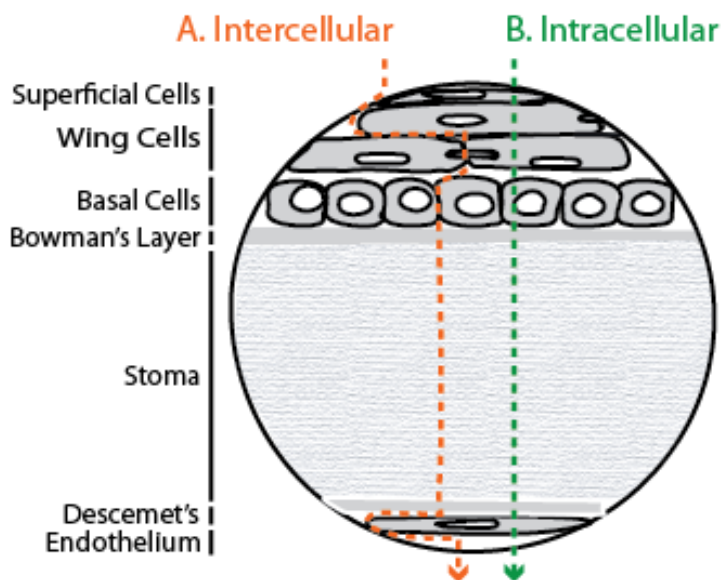


**Figure 35** Routes of transcorneal permeation of topically administered therapeutics

The intercellular permeation pathway (A) involves passage of therapeutics through the intercellular tight junctions between epithelial cell, which can be as narrow as 2 nm, through the stroma, and between endothelial cells. Only solutes, and nano-sized molecules are able to take this transcorneal permeation pathway. The intracellular pathway (B) requires therapeutics to transverse the thickness of the various corneal layers. The permeation pathway of any therapeutic is decided by its chemical and physical features, including charge, size, and pH.

To determine whether this could be a potential pathway for NPs, assessment of corneal permeation capacity of PGL<sub>DOPE</sub> NPs, was undertaken, using a reconstructed 3-D corneal model, whose permeability and structural properties have been shown to closely resemble that of the human corneal epithelium [207]. The optimized 10:1  $\rho_{\pm}$  PGL<sub>DOPE</sub> NPs were able to permeate a total distance of approximately 35-40  $\mu\text{m}$  out of the 65  $\mu\text{m}$  total thickness, 15 hours after

topical application. Two main factors are thought to have aided the permeation of PGL NPs through the HCE. First, the cationic nature of PGL<sub>DOPE</sub> NPs lends them the ability to bind to the negatively charged HCE surface and initiate the permeation process [103-105]. It is important to point out that PGL<sub>DOPE</sub> NP contact with the cornea *in vivo* is expected to be less direct and for a shorter period than in the HCE model, given the high turnover of the tear film. Nevertheless, achieving this binding step is a promising result, given that failure of binding would lead to lacrimal elimination of the therapeutic dose. Similar studies have shown that positively charged liposomes generally achieve better corneal binding and a more prolonged therapeutic effect, compared to negatively charged ones [208]. Second, since PGL<sub>DOPE</sub> NPs are assembled with lipophilic helper lipid vesicles, their permeation through the lipophilic epithelium is probably enhanced through hydrophobic-hydrophobic interactions with the epithelial cell membranes. Several studies support this view, by demonstrating that lipophilic gene and drug carriers have a significantly higher epithelial permeation capacity, compared to hydrophilic ones [196-198]. The reason is that lipophilic carriers are able to permeate the cornea through the transcellular pathway, via fusion with the lipophilic epithelial layers, where hydrophilic carriers, which typically follow the intercellular pathway, are limited in that aspect (see review by [51]).

PGL<sub>DOPE</sub> NPs showed high biocompatibility with HCE tissue, *in vitro* based on the MTT assay. More specifically, the viability of HCE cells was  $94.8 \pm 6 \%$ , 24 hours following topical administration of 10:1  $\rho_{\pm}$  PGL<sub>DOPE</sub> NPs. Increasing the charge ratio of PGL<sub>DOPE</sub> NPs to 20:1  $\rho_{\pm}$  led to a moderate decrease in the viability of HCE model cells ( $M_{\text{viability}}$ :  $81.8 \pm 22\%$ ), due to the increased cationic surfactant-induced toxicity. PGL<sub>MF-DOPE</sub> NPs (DOPE helper lipid vesicles, prepared by microfluidization) did not increase the toxicity of PGL NPs, as demonstrated by the

comparable viability to traditional PGL<sub>DOPE</sub> NPs. These findings are in line with other studies that reported a safe toxicity profile for arginine-based gemini surfactants in ocular toxicity studies [209].

#### **4.7. *In vivo* biodistribution and gene expression of PGL<sub>DOPE</sub> NPs after ocular application**

##### **4.7.1. Intravitreally injected PGL NPs**

After 48 hours from intravitreal injection of PGL<sub>DOPE</sub> NPs in mice, the majority of labeled pDNA was localized within the INL of the retina. Several pDNA particles were observed throughout the posterior chamber, namely the vitreous (Figure 27). The capacity of PGL<sub>DOPE</sub> NP to deliver pDNA to the retina is a promising result, since it is considered the first step of initiating the gene therapy process within the retina. Furthermore, these findings are especially encouraging, considering the obstacles associated with direct injection into the posterior chamber. Intravitreal injection of cationic NPs, in general, often leads to their entrapment in the vitreous by anionic proteoglycans and fibers [50]. PGL<sub>DOPE</sub> NP small size (< 200 nm) could be one of the factors that aided in its vitreal movement. Generally lipoplexes, below 500 nm have been shown to achieve efficient vitreal mobility [210]. Interestingly, at 4 hours post-injection, intravitreally administered PGL<sub>DOPE</sub> NPs were not detected in any of posterior segment tissues. This reflects a time-course for NP trafficking, in that PGL<sub>DOPE</sub> NPs did not have a sufficient period of time to achieve complete vitreal migration. Labeled pDNA was not found in either the retina or the vitreous, 48 hours after intravitreal injection of the labeled pDNA solution. This is likely due to binding in the vitreous or DNAase degradation activity, which was previously suggested by similar studies [50, 210].



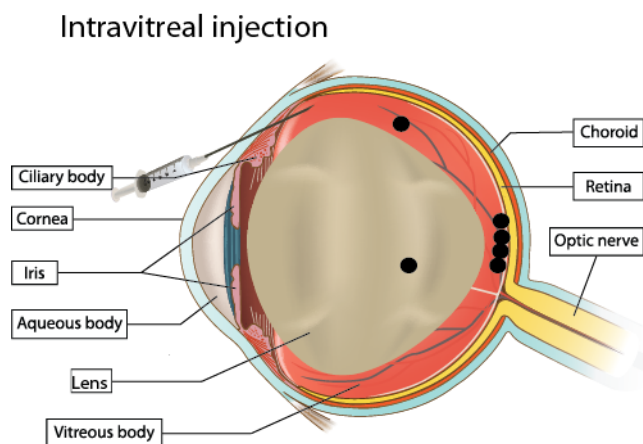


**Figure 36** A schematic figure of the biodistribution pattern of intravitreally administered 10:1 p± PGL<sub>DOPE</sub> NPs in mouse eyes

This figure is deduced from confocal microscopic observations of fluorescence in whole eye cryo-sections. 48 hour after intravitreal injection of NPs, successful localization of labeled pDNA was observed mainly within the retina's NFL, the vitreous, and on the lens (note the large size of the mouse lens).

Despite of successful localization within the retina's NFL, PGL<sub>DOPE</sub> NPs did not induce any detectable gene expression (no green GFP fluorescence). This could be due to the relatively short period following intravitreal injection (48 hours), that may not have been sufficient for enough number of PGL<sub>DOPE</sub> NPs to reach and transfect RGCs. The peak gene expression of intravitreally administered liposomes and lipoplexes *in vivo* ranges between 2-5 days. For example, transgene expression in rabbits, following intravitreal injection of cationic liposome/plasmid DNA complexes, typically peaks 3 days after intravitreal application [211, 212]. Similarly, polymer-mediated gene expression was reported to take as many as 5 days before reaching its peak [213]. Accordingly, a longer expression period would likely allow a higher proportion of PGL<sub>DOPE</sub> NPs to pass the ILM barrier, and reach RGCs to complete their gene transfer process. The ILM is considered a limiting barrier to the internalization of non-viral and viral gene delivery vectors, following intravitreal injection [214, 215]. The ILM structure is

formed by the fusion of Müller glia foot processes, where tight junctions are formed, protecting the retina from potential contaminants or pathogens [216]. Various ECM components, including several proteins and proteoglycans [217] also pose resistance to the passage of NPs and viral vectors towards the RGC layer [214].

Another consideration is the limited intravitreal dosage volume (2 $\mu$ L) due to the small size of mouse eye, and relatively large lens size, which takes up the majority of the mouse's eye volume. To meet this limited dose volume requirement, and maintain the plasmid dose in the correct ratio with the gemini surfactant and lipid, the NP dispersion was concentrated by centrifugal filtration. NPs typically interact more strongly in a highly concentrated dispersion which may lead to aggregation, which in turn could affect the transfection efficiency of NPs. The use of larger animals would allow for use of larger injection volumes, and physicochemical instability would not be a concern.

Currently, viral gene delivery systems remain more efficient in delivering genes to the retina, than non-viral ones, in most cases [218, 219]. As previously mentioned, the main shortcoming of the viral systems, their immunogenicity, remains largely unresolved. More recently, parameter optimization of certain non-viral gene delivery systems have yielded comparable transfection efficiencies to those achieved by viral ones. For example, a transfection efficiency of 75 $\pm$ 4% was achieved in RGCs, by intravitreal injection of polymeric PEI-based NPs in mice [213]. The study used a short hairpin RNA (shRNA) to knock down the expression of the melanopsin photopigment, and induce expression of the red reporter protein, *discosoma*. Expression was reported to last for at least two months, post injection. Similarly, extensive expression in RGCs was recently achieved, following intravitreal injection of

low molecular weight, chitosan-based polyplexes in adult Sprague-Dawley rats [220]. Similar to PGL NPs, the chitosan-based polyplexes had a net positive charge, and size between  $67.3 \pm 0.44$  nm and  $256.5 \pm 5.6$  nm, depending on the charge ratio. Additionally, intravitreal injection of sterically stabilized liposomes in rabbits, have recently been shown to provide excellent gene transfer and sustained release to the retina, while minimizing non-specific tissue uptake [221]. These emerging systems commonly use small nucleic acids, siRNA and small oligonucleotides. This would naturally further decrease their size profile and improve their transfection efficiency. These findings provide strong incentive for the pursuit of efficient and safe non-viral gene delivery systems for glaucoma treatments.

#### **4.8. Topically administered eye drops of PGL<sub>DOPE-N</sub> NPs**

Topically administered therapeutics to the retina typically take one of two possible diffusion routes (Figure 37). The first is the transcorneal diffusion route, which requires complete corneal permeation towards the anterior chamber, before migrating through the posterior chamber and vitreous, and finally towards the retina. The second route, lateral diffusion, begins with trans-conjunctival permeation, continuing through the sclera, uvea, and the posterior chamber [205]. Lateral diffusion is generally more accessible than the heavily restrictive trans-corneal route, due to the leaky conjunctival gap junctions. However, trafficked therapeutics through the conjunctiva face lymphatic and circulatory system elimination, which often reroutes therapeutic material towards systemic circulation [215]. This reduces the therapeutic potency of the treatment, and may lead to unwanted systemic exposure.

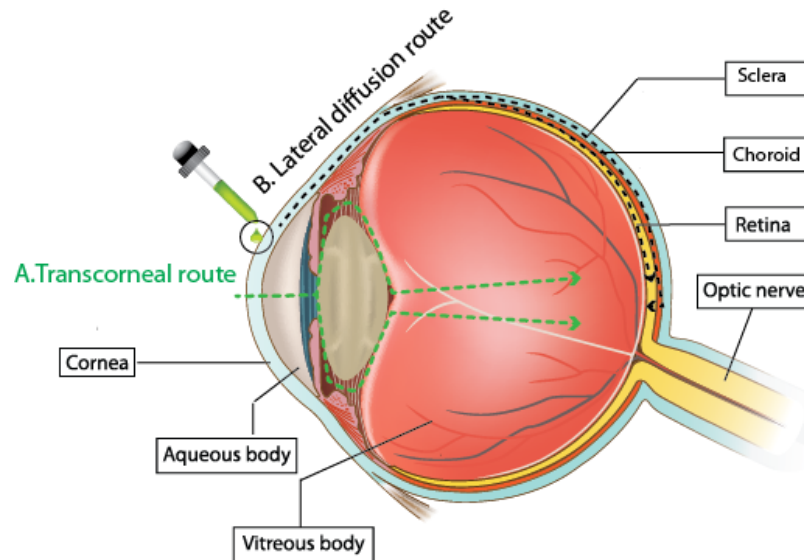


**Figure 37** Potential routes for topically administered, retina-targeted therapeutics

The transcorneal route (A), while highly restrictive, is a very important permeation pathway to the retina. In addition to targeting the retina, therapeutics that pass through the cornea could also target important glaucoma-relevant tissues, such as the TM and the ciliary muscle. The lateral diffusion pathway (B) requires passage of therapeutics through the corneal junctions to the sclera, and their diffusion laterally to the retina. The main limitation of this pathway is the risk of systemic elimination of therapeutics as they pass through the various tissue layers. Non-specific uptake and expression is also a downside of the lateral diffusion pathway.

Three hours following topical administration of PGL<sub>DOPE-N</sub> NPs, Cy5 labeled pDNA was located around the limbus, the iris and the conjunctive (Figure 38). Based on the localization of the labeled pDNA, several speculations can be made. First, PGL<sub>DOPE-N</sub> NPs appear to have diffused in the direction of lacrimal drainage towards the Schlemm canal, before releasing their payload. Therefore, the diffusion pattern suggests that they were trafficked through the lateral diffusion pathway, as opposed to the transcorneal one. This diffusion pattern led to the accumulation of labeled pDNA in the tissue of the anterior angle of the eye. Second, the biodistribution of pDNA within the tissues of the anterior angle suggests that PGL<sub>DOPE-N</sub> NPs are capable of diffusing through the epithelial junctions of the conjunctiva, sclera and the iris for a

considerable distance. Thirdly, imaging did not reveal the presence of green fluorescent NBD-PE, which was incorporated in the DOPE lipid vesicles for short-term biodistribution assessment. This suggests the dissociation of helper lipid vesicles from the NP and its clearance or metabolism, possibly through the lacrimal drainage system, which would eventually lead to the stomach. In contrast, 48 hours following topical administration, labeled pDNA was not found in any of the anterior ocular tissues, possibly due to systemic or lymphatic elimination of pDNA during its lateral diffusion through the conjunctiva and sclera. Similar to the finding in the intravitreal administration condition, no gene expression was found in the tissues that PGL<sub>DOPE-N</sub> NPs reached.

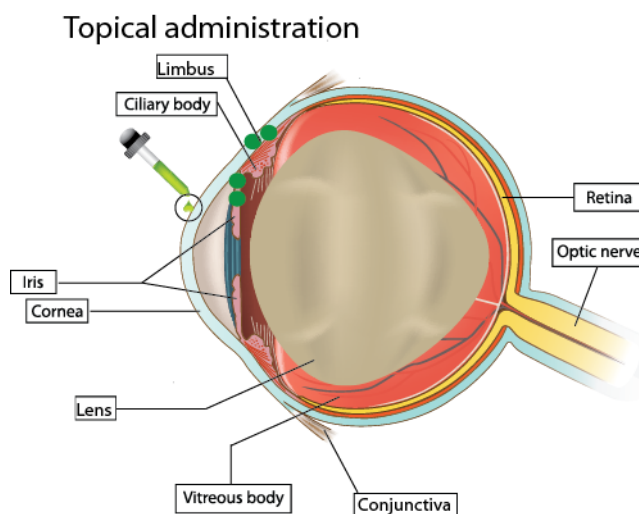


**Figure 38** A schematic figure of the biodistribution pattern of topically administered PGL<sub>DOPE-N</sub> NPs in mouse eyes

This figure is deduced from confocal microscopic observations of fluorescence in whole eye cryosections. Four hours after topical administration of PGL<sub>DOPE-N</sub> NPs, successful localization of labeled pDNA was observed mainly within the limbus, the iris, and the conjunctiva.

## 5. Conclusions and future direction

12-7NH-12 PGL NPs have demonstrated many advantages to their use as retina-targeted ocular gene delivery systems. These include considerable transfection efficiency in an *in vitro* RGC model, very low toxicity in RGC cells and corneal tissue, efficient corneal binding, and a promising *in vivo* biodistribution pattern, following topical and intravitreal injection. PGL NP responsiveness to the optimization of their physical and chemical parameters suggests that their capacity can be further enhanced, to achieve higher transfection efficiencies. By achieving this improvement, we can expect PGL NPs to be more efficient in inducing clinically significant cellular responses, such as neurite outgrowth. Furthermore, PGL NP binding and moderate permeation in the HCE model provides a starting point for further work aimed at tailoring these NPs to overcoming the corneal barrier. The capacity of PGL NPs to reach the anterior chamber, as was seen in localization of transgene in the iris, could allow for targeting of glaucoma-relevant tissue, such as the TM and the ciliary body. Since TM's function of maintaining IOP relies heavily on the structural density of the ECM [74], these components can be targeted in future gene delivery studies to regulate aqueous humor outflow and lower intraocular pressure. For example, Rho guanosine triphosphate (GTPase) pathway, which regulates aqueous outflow by altering TM's cell morphology and the structure of the actin cytoskeleton, could serve as a target pathway for regulating aqueous humor drainage [77]. In conclusion, the current work has provided an incentive for further development of 12-7NH-12 PGL NPs for ocular gene delivery, which could provide options for a new glaucoma treatment approach.

## Copyright permissions

### License for text and figures in introduction

License Number	3072800241858
License date	Jan 19, 2013
Licensed content publisher	Future Medicine Ltd
Licensed content title	Nanomedicine
Licensed content date	Jan 1, 2006
Type of Use	Thesis/Dissertation
Requestor type	Author of requested content
Format	Print, Electronic
Portion	chapter/article
Title or numeric reference of the portion(s)	article and figures in pages 1067-1083
Editor of portion(s)	n/a
Author of portion(s)	n/a
Volume of serial or monograph.	7
Issue, if republishing an article from a serial	7
Page range of the portion	
Publication date of portion	2012
Rights for	Main product
Duration of use	Life of current edition
Creation of copies for the disabled	no
With minor editing	no

privileges	
For distribution to	United States
In the following language(s)	Original language of publication
With incidental promotional use	no
The lifetime unit quantity of new product	0 to 499
Made available in the following markets	Education
Specified additional information	author wants to use his material in the thesis
The requesting person/organization is:	Samih Alqawlaq
Author/Editor	Samih Alqawlaq
The standard identifier	thesisSamih13
Title	Non-viral gemini phospholipid nanoparticles for topical gene delivery to the retina
Publisher	Samih Alqawlaq
Expected publication date	Feb 2013
Estimated size (pages)	15

### License for figure used in methods (Figure 9-B)

Order detail ID	63369158
Article Title	Morphological evaluation of normal human corneal epithelium
Author(s)	Ehlers, Niels ; et al
DOI	10.1111/J.1755-3768.2009.01610.X
Date	Nov 29, 2010
ISSN	1755-375X
Publication Type	Journal
Volume	88
Issue	8
Start page	858



Publisher	BLACKWELL PUBLISHING
Author/Editor	Dansk oftalmologisk selskab
Start page	858
End page	861
Requestor type	University/Academic
Format	Print and electronic
Portion	Figure/table
Number of figures/tables	1
Original Wiley figure/table number(s)	1-A
Will you be translating?	No

### License for figure used in the discussion (Figure 30, 34)

License Number	3053820843151
License date	Dec 21, 2012
Licensed content publisher	Elsevier
Licensed content publication	Journal of Controlled Release
Licensed content title	On the cellular processing of non-viral nanomedicines for nucleic acid delivery:Mechanisms and methods
Licensed content author	Dries Vercauteren,Joanna Rejman,Thomas F. Martens, Jo Demeester,Stefaan C. De Smedt,Kevin Braeckmans
Licensed content date	20 July 2012
Licensed content volume number	161
Licensed content issue number	2
Number of pages	16
Type of Use	reuse in a thesis/dissertation
Portion	figures/tables/illustrations
Number of figures/tables/illustrations	1
Format	both print and electronic
Are you the author of this	No

Elsevier article?	
Will you be translating?	No
Order reference number	None
Title of your thesis/dissertation	Non-viral gemini surfactant-phospholipid nanoparticles for topical gene delivery to the retina
Expected completion date	Jan 2013
Estimated size (number of pages)	130
Elsevier VAT number	GB 494 6272 12

## References

1. Quigley, H.A. and A.T. Broman, *The number of people with glaucoma worldwide in 2010 and 2020*. Br J Ophthalmol, 2006. **90**(3): p. 262-7.
2. Foster, A. and S. Resnikoff, *The impact of Vision 2020 on global blindness*. Eye, 2005. **19**(10): p. 1133-5.
3. Margalit, E. and S.R. Sadda, *Retinal and optic nerve diseases*. Artif Organs, 2003. **27**(11): p. 963-74.
4. Quigley, H.A., *Open-angle glaucoma*. N Engl J Med, 1993. **328**(15): p. 1097-106.
5. Crawford Downs, J., M.D. Roberts, and I.A. Sigal, *Glaucomatous cupping of the lamina cribrosa: a review of the evidence for active progressive remodeling as a mechanism*. Exp Eye Res, 2011. **93**(2): p. 133-40.
6. Alqawlaq, S., et al., *Challenges in neuroprotective nanomedicine development: progress towards noninvasive gene therapy of glaucoma*. Nanomedicine (Lond), 2012. **7**(7): p. 1067-83.
7. Hayreh, S.S., *The 1994 Von Sallman Lecture. The optic nerve head circulation in health and disease*. Exp Eye Res, 1995. **61**(3): p. 259-72.
8. Kass, M.A. and B. Becker, *Genetics of primary open-angle glaucoma*. Sight Sav Rev, 1978. **48**(1): p. 21-8.
9. Quigley, H.A. and S. Vitale, *Models of open-angle glaucoma prevalence and incidence in the United States*. Invest Ophthalmol Vis Sci, 1997. **38**(1): p. 83-91.
10. Klein, B.E., R. Klein, and S.E. Moss, *Incidence of self reported glaucoma in people with diabetes mellitus*. Br J Ophthalmol, 1997. **81**(9): p. 743-7.
11. Sigal, I.A., J.G. Flanagan, and C.R. Ethier, *Factors influencing optic nerve head biomechanics*. Invest Ophthalmol Vis Sci, 2005. **46**(11): p. 4189-99.
12. Lavery, W.J., et al., *Magnetic resonance imaging indicates decreased choroidal and retinal blood flow in the DBA/2J mouse model of glaucoma*. Invest Ophthalmol Vis Sci, 2012. **53**(2): p. 560-4.
13. Yang, Q., et al., *Effect of acute intraocular pressure elevation on blood flow velocity and resistance in the rabbit ophthalmic artery*. Vet Ophthalmol, 2011. **14**(6): p. 353-7.
14. Alm, A. and A. Bill, *The oxygen supply to the retina. II. Effects of high intraocular pressure and of increased arterial carbon dioxide tension on uveal and retinal blood flow in cats. A study with radioactively labelled microspheres including flow determinations in brain and some other tissues*. Acta Physiol Scand, 1972. **84**(3): p. 306-19.
15. Okuno, T., et al., *Glutamate level in optic nerve head is increased by artificial elevation of intraocular pressure in rabbits*. Experimental Eye Research, 2006. **82**(3): p. 465-470.
16. Neufeld, A.H., M.R. Hernandez, and M. Gonzalez, *Nitric oxide synthase in the human glaucomatous optic nerve head*. Arch Ophthalmol, 1997. **115**(4): p. 497-503.
17. Neufeld, A.H., et al., *Loss of retinal ganglion cells following retinal ischemia: the role of inducible nitric oxide synthase*. Exp Eye Res, 2002. **75**(5): p. 521-8.
18. Siu, A.W., et al., *Total retinal nitric oxide production is increased in intraocular pressure-elevated rats*. Exp Eye Res, 2002. **75**(4): p. 401-6.
19. Malone, P., et al., *Pressure induces loss of gap junction communication and redistribution of connexin 43 in astrocytes*. Glia, 2007. **55**(10): p. 1085-98.

20. Quigley, H.A., et al., *Retrograde Axonal Transport of BDNF in Retinal Ganglion Cells Is Blocked by Acute IOP Elevation in Rats*. Investigative Ophthalmology & Visual Science, 2000. **41**(11): p. 3460-3466.
21. van der Valk, R., et al., *Intraocular Pressure–Lowering Effects of All Commonly Used Glaucoma Drugs: A Meta-analysis of Randomized Clinical Trials*. Ophthalmology, 2005. **112**(7): p. 1177-1185.
22. Johnson, T.V., N.D. Bull, and K.R. Martin, *Neurotrophic factor delivery as a protective treatment for glaucoma*. Exp Eye Res, 2010.
23. Bessero, A.C. and P.G. Clarke, *Neuroprotection for optic nerve disorders*. Curr Opin Neurol, 2010. **23**(1): p. 10-5.
24. Baltmr, A., et al., *Neuroprotection in glaucoma - Is there a future role?* Exp Eye Res, 2010. **91**(5): p. 554-66.
25. Lundmark, P.O., et al., *Melatonin in the eye: implications for glaucoma*. Exp Eye Res, 2007. **84**(6): p. 1021-30.
26. Tezel, G. and M.B. Wax, *Increased production of tumor necrosis factor-alpha by glial cells exposed to simulated ischemia or elevated hydrostatic pressure induces apoptosis in cocultured retinal ganglion cells*. J Neurosci, 2000. **20**(23): p. 8693-700.
27. Ellis-Behnke, R.G., et al., *Nano neuro knitting: peptide nanofiber scaffold for brain repair and axon regeneration with functional return of vision*. Proc Natl Acad Sci U S A, 2006. **103**(13): p. 5054-9.
28. Harvey, A.R., et al., *Gene therapy and transplantation in CNS repair: the visual system*. Prog Retin Eye Res, 2006. **25**(5): p. 449-89.
29. Henderson, C.E., *Role of neurotrophic factors in neuronal development*. Curr Opin Neurobiol, 1996. **6**(1): p. 64-70.
30. Weber, A.J., C.D. Harman, and S. Viswanathan, *Effects of optic nerve injury, glaucoma, and neuroprotection on the survival, structure, and function of ganglion cells in the mammalian retina*. J Physiol, 2008. **586**(Pt 18): p. 4393-400.
31. Di Polo, A., et al., *Prolonged delivery of brain-derived neurotrophic factor by adenovirus-infected Muller cells temporarily rescues injured retinal ganglion cells*. Proc Natl Acad Sci U S A, 1998. **95**(7): p. 3978-83.
32. van Adel, B.A., et al., *Delivery of ciliary neurotrophic factor via lentiviral-mediated transfer protects axotomized retinal ganglion cells for an extended period of time*. Hum Gene Ther, 2003. **14**(2): p. 103-15.
33. Leaver, S.G., et al., *Cooperative effects of bcl-2 and AAV-mediated expression of CNTF on retinal ganglion cell survival and axonal regeneration in adult transgenic mice*. Eur J Neurosci, 2006. **24**(12): p. 3323-32.
34. Ishikawa, H., et al., *Effect of GDNF gene transfer into axotomized retinal ganglion cells using in vivo electroporation with a contact lens-type electrode*. Gene Ther, 2005. **12**(4): p. 289-98.
35. Watanabe, M. and Y. Fukuda, *Survival and axonal regeneration of retinal ganglion cells in adult cats*. Prog Retin Eye Res, 2002. **21**(6): p. 529-53.
36. Peinado-Ramon, P., et al., *Effects of axotomy and intraocular administration of NT-4, NT-3, and brain-derived neurotrophic factor on the survival of adult rat retinal ganglion cells. A quantitative in vivo study*. Invest Ophthalmol Vis Sci, 1996. **37**(4): p. 489-500.

37. Yan, Q., et al., *Glial cell line-derived neurotrophic factor (GDNF) promotes the survival of axotomized retinal ganglion cells in adult rats: comparison to and combination with brain-derived neurotrophic factor (BDNF)*. J Neurobiol, 1999. **38**(3): p. 382-90.
38. Koeberle, P.D. and A.K. Ball, *Neurturin enhances the survival of axotomized retinal ganglion cells in vivo: combined effects with glial cell line-derived neurotrophic factor and brain-derived neurotrophic factor*. Neuroscience, 2002. **110**(3): p. 555-67.
39. Mansour-Robaey, S., et al., *Effects of ocular injury and administration of brain-derived neurotrophic factor on survival and regrowth of axotomized retinal ganglion cells*. Proc Natl Acad Sci U S A, 1994. **91**(5): p. 1632-6.
40. Benowitz, L. and Y. Yin, *Rewiring the injured CNS: lessons from the optic nerve*. Exp Neurol, 2008. **209**(2): p. 389-98.
41. Benowitz, L.I. and Y. Yin, *Optic nerve regeneration*. Arch Ophthalmol, 2010. **128**(8): p. 1059-64.
42. Chen, T.J., et al., *Cdc42 participates in the regulation of ADF/cofilin and retinal growth cone filopodia by brain derived neurotrophic factor*. J Neurobiol, 2006. **66**(2): p. 103-14.
43. Cohen-Cory, S., et al., *Brain-derived neurotrophic factor and the development of structural neuronal connectivity*. Dev Neurobiol, 2010. **70**(5): p. 271-88.
44. Kurz, D. and T.A. Ciulla, *Novel approaches for retinal drug delivery*. Ophthalmology Clinics of North America, 2002. **15**(3): p. 405-410.
45. Bill, A., *The blood-aqueous barrier*. Trans Ophthalmol Soc U K, 1986. **105 ( Pt 2)**: p. 149-55.
46. Smith, R.S., *Ultrastructural studies of the blood-aqueous barrier. I. Transport of an electron-dense tracer in the iris and ciliary body of the mouse*. Am J Ophthalmol, 1971. **71**(5): p. 1066-77.
47. Cunha-Vaz, J.G., *The blood-retinal barriers*. Doc Ophthalmol, 1976. **41**(2): p. 287-327.
48. Ijichi, H., et al., [*Scanning and transmission electron microscopic studies of the ultrastructure of the corneal endothelium in developing human eye*]. Nihon Ganka Gakkai Zasshi, 1992. **96**(11): p. 1351-6.
49. Rabinovich-Guilatt, L., et al., *Cationic vectors in ocular drug delivery*. J Drug Target, 2004. **12**(9-10): p. 623-33.
50. Pitkanen, L., et al., *Vitreous is a barrier in nonviral gene transfer by cationic lipids and polymers*. Pharm Res, 2003. **20**(4): p. 576-83.
51. Barar, J., A.R. Javadzadeh, and Y. Omid, *Ocular novel drug delivery: impacts of membranes and barriers*. Expert Opin Drug Deliv, 2008. **5**(5): p. 567-81.
52. de la Fuente, M., et al., *Chitosan-based nanostructures: a delivery platform for ocular therapeutics*. Adv Drug Deliv Rev, 2010. **62**(1): p. 100-17.
53. Danesh-Meyer, H.V., *Neuroprotection in glaucoma: recent and future directions*. Curr Opin Ophthalmol, 2011. **22**(2): p. 78-86.
54. Gardlik, R., et al., *Vectors and delivery systems in gene therapy*. Med Sci Monit, 2005. **11**(4): p. RA110-21.
55. Provost, N., et al., *Biodistribution of rAAV vectors following intraocular administration: evidence for the presence and persistence of vector DNA in the optic nerve and in the brain*. Mol Ther, 2005. **11**(2): p. 275-83.
56. Glover, D.J., H.J. Lipps, and D.A. Jans, *Towards safe, non-viral therapeutic gene expression in humans*. Nature Reviews Genetics, 2005. **6**(4): p. 299-310.

57. Huang, L., M.-C. Hung, and E. Wagner, *Non-viral vectors for Gene Therapy* Vol. 1. 2005: Elsevier Academic Press.
58. Ward, C.M., M.L. Read, and L.W. Seymour, *Systemic circulation of poly(L-lysine)/DNA vectors is influenced by polycation molecular weight and type of DNA: differential circulation in mice and rats and the implications for human gene therapy*. *Blood*, 2001. **97**(8): p. 2221-9.
59. Karra, D. and R. Dahm, *Transfection techniques for neuronal cells*. *J Neurosci*, 2010. **30**(18): p. 6171-7.
60. Ohki, E.C., et al., *Improving the transfection efficiency of post-mitotic neurons*. *J Neurosci Methods*, 2001. **112**(2): p. 95-9.
61. Dalby, B., et al., *Advanced transfection with Lipofectamine 2000 reagent: primary neurons, siRNA, and high-throughput applications*. *Methods*, 2004. **33**(2): p. 95-103.
62. Liaw, J., S.F. Chang, and F.C. Hsiao, *In vivo gene delivery into ocular tissues by eye drops of poly(ethylene oxide)-poly(propylene oxide)-poly(ethylene oxide) (PEO-PPO-PEO) polymeric micelles*. *Gene Ther*, 2001. **8**(13): p. 999-1004.
63. Tong, Y.C., et al., *Eye drop delivery of nano-polymeric micelle formulated genes with cornea-specific promoters*. *J Gene Med*, 2007. **9**(11): p. 956-66.
64. Masuda, I., et al., *Gene transfer with liposomes to the intraocular tissues by different routes of administration*. *Invest Ophthalmol Vis Sci*, 1996. **37**(9): p. 1914-20.
65. Matsuo, T., et al., *Gene transfer to the retina of rat by liposome eye drops*. *Biochem Biophys Res Commun*, 1996. **219**(3): p. 947-50.
66. Puras, G., et al., *Low molecular weight oligochitosans for non-viral retinal gene therapy*. *Eur J Pharm Biopharm*, 2012.
67. Zhang, Y., et al., *Organ-specific gene expression in the rhesus monkey eye following intravenous non-viral gene transfer*. *Mol Vis*, 2003. **9**: p. 465-72.
68. Jeun, M., et al., *Engineered superparamagnetic Mn<sub>0.5</sub>Zn<sub>0.5</sub>Fe<sub>2</sub>O<sub>4</sub> nanoparticles as a heat shock protein induction agent for ocular neuroprotection in glaucoma*. *Biomaterials*, 2011. **32**(2): p. 387-394.
69. Raju, H.B., et al., *Evaluation of Magnetic Micro- and Nanoparticle Toxicity to Ocular Tissues*. *PLoS One*, 2011. **6**(5): p. e17452.
70. Van Nostrum, C. *polymeric micelles for drug delivery*. *SciTopics* 2008, October 28 February 7, 2012]; Available from: [http://www.scitopics.com/polymeric\\_micelles\\_for\\_drug\\_delivery.html](http://www.scitopics.com/polymeric_micelles_for_drug_delivery.html).
71. Bergen, J.M. and S.H. Pun, *Analysis of the intracellular barriers encountered by nonviral gene carriers in a model of spatially controlled delivery to neurons*. *The Journal of Gene Medicine*, 2008. **10**(2): p. 187-197.
72. Templeton, N.S., *Gene and Cell Therapy: Therapeutic Mechanisms and Strategies*. 2004: Marcel Dekker.
73. Bergen, J.M. and S.H. Pun, *Analysis of the intracellular barriers encountered by nonviral gene carriers in a model of spatially controlled delivery to neurons*. *J Gene Med*, 2008. **10**(2): p. 187-97.
74. Rejman, J., A. Bragonzi, and M. Conese, *Role of clathrin- and caveolae-mediated endocytosis in gene transfer mediated by lipo- and polyplexes*. *Mol Ther*, 2005. **12**(3): p. 468-74.

75. Rejman, J., M. Conese, and D. Hoekstra, *Gene transfer by means of lipo- and polyplexes: role of clathrin and caveolae-mediated endocytosis*. J Liposome Res, 2006. **16**(3): p. 237-47.
76. Juliano, R.L., et al., *Integrin targeted delivery of gene therapeutics*. Theranostics, 2011. **1**: p. 211-9.
77. Reynolds, A.J., S.E. Bartlett, and I.A. Hendry, *Molecular mechanisms regulating the retrograde axonal transport of neurotrophins*. Brain Res Brain Res Rev, 2000. **33**(2-3): p. 169-78.
78. Moseley, G.W., et al., *Dynein light chain association sequences can facilitate nuclear protein import*. Mol Biol Cell, 2007. **18**(8): p. 3204-13.
79. Luby-Phelps, K., D.L. Taylor, and F. Lanni, *Probing the structure of cytoplasm*. J Cell Biol, 1986. **102**(6): p. 2015-22.
80. Zhou, R., R.C. Geiger, and D.A. Dean, *Intracellular trafficking of nucleic acids*. Expert Opin Drug Deliv, 2004. **1**(1): p. 127-40.
81. Minchin, R.F. and S. Yang, *Endosomal disruptors in non-viral gene delivery*. Expert Opin Drug Deliv, 2010. **7**(3): p. 331-9.
82. Hoekstra, D., et al., *Gene delivery by cationic lipids: in and out of an endosome*. Biochem Soc Trans, 2007. **35**(Pt 1): p. 68-71.
83. Ameri, K., E. Wagner *Receptor-Targeted Polyplexes.*, in *Gene Therapy. Therapeutic Mechanisms and Strategies*, N. Smyth-Templeton, Editor. 2005, Marcel Dekker Inc: New York.
84. Edinger, D. and E. Wagner, *Bioresponsive polymers for the delivery of therapeutic nucleic acids*. Wiley Interdiscip Rev Nanomed Nanobiotechnol, 2011. **3**(1): p. 33-46.
85. Allen, T.D., et al., *Chapter 20 Scanning Electron Microscopy of Nuclear Structure*, in *Methods in Cell Biology*, D.A. Terence, Editor. 2008, Academic Press. p. 389-409.
86. Dworetzky, S.I. and C.M. Feldherr, *Translocation of RNA-coated gold particles through the nuclear pores of oocytes*. J Cell Biol, 1988. **106**(3): p. 575-84.
87. Paine, P.L., L.C. Moore, and S.B. Horowitz, *Nuclear envelope permeability*. Nature, 1975. **254**(5496): p. 109-14.
88. Feldherr, C.M., E. Kallenbach, and N. Schultz, *Movement of a karyophilic protein through the nuclear pores of oocytes*. The Journal of Cell Biology, 1984. **99**(6): p. 2216-2222.
89. Lange, A., et al., *Classical nuclear localization signals: definition, function, and interaction with importin alpha*. J Biol Chem, 2007. **282**(8): p. 5101-5.
90. Chan, C.-K. and D.A. Jans, *Using nuclear targeting signals to enhance non-viral gene transfer*. Immunol Cell Biol, 2002. **80**(2): p. 119-130.
91. Fei, Y. and T.E. Hughes, *Nuclear trafficking of photoreceptor protein crx: the targeting sequence and pathologic implications*. Invest Ophthalmol Vis Sci, 2000. **41**(10): p. 2849-56.
92. Haller, J.A., et al., *Randomized, sham-controlled trial of dexamethasone intravitreal implant in patients with macular edema due to retinal vein occlusion*. Ophthalmology, 2010. **117**(6): p. 1134-1146 e3.
93. Kirby, A.J., et al., *Gemini surfactants: new synthetic vectors for gene transfection*. Angew Chem Int Ed Engl, 2003. **42**(13): p. 1448-57.
94. Badea, I. and T.U.o.S. . *Gemini Cationic Surfactant-based Delivery Systems for Non-invasive Cutaneous Gene Therapy*. 2006: University of Saskatchewan (Canada).

95. Yang, P., et al., *Enhanced gene expression in epithelial cells transfected with amino acid-substituted gemini nanoparticles*. Eur J Pharm Biopharm, 2010. **75**(3): p. 311-20.
96. Wasungu, L., et al., *Transfection mediated by pH-sensitive sugar-based gemini surfactants; potential for in vivo gene therapy applications*. J Mol Med, 2006. **84**(9): p. 774-84.
97. Badea, I., et al., *Topical non-invasive gene delivery using gemini nanoparticles in interferon-gamma-deficient mice*. Eur J Pharm Biopharm, 2007. **65**(3): p. 414-22.
98. Frassetto, L.J., et al., *Kinase-dependent differentiation of a retinal ganglion cell precursor*. Invest Ophthalmol Vis Sci, 2006. **47**(1): p. 427-38.
99. Hornof, M., E. Toropainen, and A. Urtti, *Cell culture models of the ocular barriers*. Eur J Pharm Biopharm, 2005. **60**(2): p. 207-25.
100. Vecino, E., [*Animal models in the study of the glaucoma: past, present and future*]. Arch Soc Esp Oftalmol, 2008. **83**(9): p. 517-9.
101. Bouhenni, R.A., et al., *Animal models of glaucoma*. J Biomed Biotechnol, 2012. **2012**: p. 692609.
102. Baba, K., et al., *A method for enhancing the ocular penetration of eye drops using nanoparticles of hydrolyzable dye*. J Control Release, 2011.
103. Schaeffer, H.E. and D.L. Krohn, *Liposomes in topical drug delivery*. Invest Ophthalmol Vis Sci, 1982. **22**(2): p. 220-7.
104. Law, S.L., K.J. Huang, and C.H. Chiang, *Acyclovir-containing liposomes for potential ocular delivery. Corneal penetration and absorption*. J Control Release, 2000. **63**(1-2): p. 135-40.
105. Klang, S.H., et al., *Evaluation of a positively charged submicron emulsion of piroxicam on the rabbit corneum healing process following alkali burn*. J Control Release, 1999. **57**(1): p. 19-27.
106. Wettig, S.D., et al., *Thermodynamic and aggregation properties of aza- and imino-substituted gemini surfactants designed for gene delivery*. Phys Chem Chem Phys, 2007. **9**(7): p. 871-7.
107. McMillian, M.K., et al., *An improved resazurin-based cytotoxicity assay for hepatic cells*. Cell Biol Toxicol, 2002. **18**(3): p. 157-73.
108. Scientific, T. *beta-3 Tubulin Monoclonal Antibody, FITC conjugate (TU-20)*. 2012 [cited 2012; Available from: <http://www.pierce-antibodies.com/beta-3-Tubulin-antibody-clone-TU-20-Monoclonal--MA119582.html>].
109. Ricker, H.A., Neal, P.J., Kubilus, J., Klausner, M. (1994) *INITIAL CHARACTERIZATION OF A NEW MODEL FOR OCULAR IRRITANCY TESTING*. **30A**.
110. Ehlers, N., et al., *Morphological evaluation of normal human corneal epithelium*. Acta Ophthalmol, 2010. **88**(8): p. 858-61.
111. Segura, T. and L.D. Shea, *Materials for non-viral gene delivery*. Annual Review of Materials Research, 2001. **31**: p. 25-46.
112. Reinstein, D.Z., et al., *Epithelial thickness in the normal cornea: three-dimensional display with Artemis very high-frequency digital ultrasound*. J Refract Surg, 2008. **24**(6): p. 571-81.
113. Wettig, S.D., et al., *Structural and transfection properties of amine-substituted gemini surfactant-based nanoparticles*. J Gene Med, 2007. **9**(8): p. 649-58.



114. Donkuru, M., et al., *Designing pH-sensitive gemini nanoparticles for non-viral gene delivery into keratinocytes*. Journal of Materials Chemistry, 2012. **22**(13): p. 6232-6244.
115. Badea, I., et al., *Effect of topical interferon-gamma gene therapy using gemini nanoparticles on pathophysiological markers of cutaneous scleroderma in Tsk/+ mice*. Gene Ther, 2012. **19**(10): p. 978-87.
116. Karlsson, L., M.C. van Eijk, and O. Soderman, *Compaction of DNA by gemini surfactants: effects of surfactant architecture*. J Colloid Interface Sci, 2002. **252**(2): p. 290-6.
117. del Pozo-Rodriguez, A., et al., *Short- and long-term stability study of lyophilized solid lipid nanoparticles for gene therapy*. Eur J Pharm Biopharm, 2009. **71**(2): p. 181-9.
118. Liang, W. and J.K.W. Lam, *Endosomal Escape Pathways for Non-Viral Nucleic Acid Delivery Systems*. Molecular Regulation of Endocytosis. 2012.
119. Chen, H.H., et al., *Quantitative analysis of nanoparticle internalization in mammalian cells by high resolution X-ray microscopy*. J Nanobiotechnology, 2011. **9**: p. 14.
120. Zhu, L., et al., *Structural and formulation factors influencing pyridinium lipid-based gene transfer*. Bioconjug Chem, 2008. **19**(12): p. 2499-512.
121. Izumisawa, T., et al., *Cell line-dependent internalization pathways determine DNA transfection efficiency of decaarginine-PEG-lipid*. Int J Pharm, 2011. **404**(1-2): p. 264-70.
122. Fitzgibbon, T., R.J. Wingate, and I.D. Thompson, *Soma and axon diameter distributions and central projections of ferret retinal ganglion cells*. Vis Neurosci, 1996. **13**(4): p. 773-86.
123. Brgles, M., et al., *Influence of charge ratio of liposome/DNA complexes on their size after extrusion and transfection efficiency*. Int J Nanomedicine, 2012. **7**: p. 393-401.
124. Hunter, R.J., *Zeta potential in colloid science : principles and applications*. 1981, London; New York: Academic Press.
125. Madeira, C., et al., *Liposome complexation efficiency monitored by FRET: effect of charge ratio, helper lipid and plasmid size*. Eur Biophys J, 2007. **36**(6): p. 609-20.
126. Badea, I., *Gemini cationic surfactant-based delivery systems for non-invasive cutaneous gene therapy*. 2007, Library and Archives Canada = Bibliothèque et Archives Canada: Ottawa.
127. Wolfe, J., et al., *The interaction and fusion of bilayers formed from unsaturated lipids*. Eur Biophys J, 1991. **19**(5): p. 275-81.
128. Witoonsaridsilp, W., et al., *Influence of microenvironment and liposomal formulation on secondary structure and bilayer interaction of lysozyme*. Colloids Surf B Biointerfaces, 2010. **75**(2): p. 501-9.
129. Trantum, K., et al., *Calorimetric Investigations of Non-Viral DNA Transfection Systems*. Thermodynamics - Kinetics of Dynamic Systems. 2011.
130. Kreiss, P., et al., *Plasmid DNA size does not affect the physicochemical properties of lipoplexes but modulates gene transfer efficiency*. Nucleic Acids Res, 1999. **27**(19): p. 3792-8.
131. Akbar, J., et al., *Mixed aggregate formation in gemini surfactant/1,2-dialkyl-sn-glycero-3-phosphoethanolamine systems*. J Colloid Interface Sci, 2012. **377**(1): p. 237-43.
132. Albanese, A., P.S. Tang, and W.C. Chan, *The effect of nanoparticle size, shape, and surface chemistry on biological systems*. Annu Rev Biomed Eng, 2012. **14**: p. 1-16.

133. Rejman, J., et al., *Size-dependent internalization of particles via the pathways of clathrin- and caveolae-mediated endocytosis*. *Biochem J*, 2004. **377**(Pt 1): p. 159-69.
134. Singh, J., et al., *Evaluation of cellular uptake and intracellular trafficking as determining factors of gene expression for amino acid-substituted gemini surfactant-based DNA nanoparticles*. *J Nanobiotechnology*, 2012. **10**: p. 7.
135. Ma, B., et al., *Lipoplex morphologies and their influences on transfection efficiency in gene delivery*. *J Control Release*, 2007. **123**(3): p. 184-94.
136. Vercauteren, D., et al., *On the cellular processing of non-viral nanomedicines for nucleic acid delivery: mechanisms and methods*. *J Control Release*, 2012. **161**(2): p. 566-81.
137. Cebrian, V., et al., *Size-dependent transfection efficiency of PEI-coated gold nanoparticles*. *Acta Biomater*, 2011. **7**(10): p. 3645-55.
138. Oh, E., et al., *Cellular uptake and fate of PEGylated gold nanoparticles is dependent on both cell-penetration peptides and particle size*. *ACS Nano*, 2011. **5**(8): p. 6434-48.
139. Almofti, M.R., et al., *Lipoplex size determines lipofection efficiency with or without serum*. *Mol Membr Biol*, 2003. **20**(1): p. 35-43.
140. Turek, J., et al., *Formulations which increase the size of lipoplexes prevent serum-associated inhibition of transfection*. *J Gene Med*, 2000. **2**(1): p. 32-40.
141. Yang, X.R., L. Zong, and X.Y. Yuan, [*Chitosan nanoparticles as gene vector: effect of particle size on transfection efficiency*]. *Yao Xue Xue Bao*, 2007. **42**(7): p. 774-9.
142. Stegmann, T. and J.Y. Legendre, *Gene transfer mediated by cationic lipids: lack of a correlation between lipid mixing and transfection*. *Biochim Biophys Acta*, 1997. **1325**(1): p. 71-9.
143. Son, K.K., D. Tkach, and D.H. Patel, *Zeta potential of transfection complexes formed in serum-free medium can predict in vitro gene transfer efficiency of transfection reagent*. *Biochim Biophys Acta*, 2000. **1468**(1-2): p. 11-4.
144. Ross, P.C. and S.W. Hui, *Lipoplex size is a major determinant of in vitro lipofection efficiency*. *Gene Ther*, 1999. **6**(4): p. 651-9.
145. Madani, F., et al., *Mechanisms of cellular uptake of cell-penetrating peptides*. *J Biophys*, 2011. **2011**: p. 414729.
146. Saha, K., et al., *Surface Functionality of Nanoparticles Determines Cellular Uptake Mechanisms in Mammalian Cells*. *Small*, 2012.
147. Zuidam, N.J. and Y. Barenholz, *Electrostatic and structural properties of complexes involving plasmid DNA and cationic lipids commonly used for gene delivery*. *Biochim Biophys Acta*, 1998. **1368**(1): p. 115-28.
148. Zuidam, N.J., Y. Barenholz, and A. Minsky, *Chiral DNA packaging in DNA-cationic liposome assemblies*. *FEBS Lett*, 1999. **457**(3): p. 419-22.
149. Li, Y., et al., *Relationships between liposome properties, cell membrane binding, intracellular processing, and intracellular bioavailability*. *AAPS J*, 2011. **13**(4): p. 585-97.
150. Cullis, P.R., M.J. Hope, and C.P. Tilcock, *Lipid polymorphism and the roles of lipids in membranes*. *Chem Phys Lipids*, 1986. **40**(2-4): p. 127-44.
151. Koltover, I., et al., *An inverted hexagonal phase of cationic liposome-DNA complexes related to DNA release and delivery*. *Science*, 1998. **281**(5373): p. 78-81.
152. Farhood, H., N. Serbina, and L. Huang, *The role of dioleoyl phosphatidylethanolamine in cationic liposome mediated gene transfer*. *Biochimica et Biophysica Acta (BBA) - Biomembranes*, 1995. **1235**(2): p. 289-295.

153. Sakurai, F., et al., *Effects of erythrocytes and serum proteins on lung accumulation of lipoplexes containing cholesterol or DOPE as a helper lipid in the single-pass rat lung perfusion system*. Eur J Pharm Biopharm, 2001. **52**(2): p. 165-72.
154. Orsi, M. and J.W. Essex, *Physical properties of mixed bilayers containing lamellar and nonlamellar lipids: insights from coarse-grain molecular dynamics simulations*. Faraday Discussions, 2013.
155. Kirk, G.L. and S.M. Gruner, *Lyotropic effects of alkanes and headgroup composition on the la-Hii lipid liquid crystal phase transition : hydrocarbon packing versus intrinsic curvature*. J. Phys. France, 1985. **46**(5): p. 761-769.
156. Tilcock, C.P.S., P.R. Cullis, and S.M. Gruner, *On the validity of 31P-NMR determinations of phospholipid polymorphic phase behaviour*. Chemistry and Physics of Lipids, 1986. **40**(1): p. 47-56.
157. Marrink, S.J. and A.E. Mark, *Molecular view of hexagonal phase formation in phospholipid membranes*. Biophys J, 2004. **87**(6): p. 3894-900.
158. Foldvari, M., et al., *Structural characterization of novel gemini non-viral DNA delivery systems for cutaneous gene therapy*. Journal of Experimental Nanoscience, 2006. **1**(2): p. 165-176.
159. Farhood, H., N. Serbina, and L. Huang, *The role of dioleoyl phosphatidylethanolamine in cationic liposome mediated gene transfer*. Biochim Biophys Acta, 1995. **1235**(2): p. 289-95.
160. Felgner, J.H., et al., *Enhanced gene delivery and mechanism studies with a novel series of cationic lipid formulations*. J Biol Chem, 1994. **269**(4): p. 2550-61.
161. Hui, S.W., et al., *The role of helper lipids in cationic liposome-mediated gene transfer*. Biophys J, 1996. **71**(2): p. 590-9.
162. Lin, A.J., et al., *Three-dimensional imaging of lipid gene-carriers: membrane charge density controls universal transfection behavior in lamellar cationic liposome-DNA complexes*. Biophys J, 2003. **84**(5): p. 3307-16.
163. Piest, M. and J.F. Engbersen, *Effects of charge density and hydrophobicity of poly(amido amine)s for non-viral gene delivery*. J Control Release, 2010. **148**(1): p. 83-90.
164. Ewert, K., et al., *Cationic lipid-DNA complexes for gene therapy: understanding the relationship between complex structure and gene delivery pathways at the molecular level*. Curr Med Chem, 2004. **11**(2): p. 133-49.
165. Angelov, B., M. Ollivon, and A. Angelova, *X-ray Diffraction Study of the Effect of the Detergent Octyl Glucoside on the Structure of Lamellar and Nonlamellar Lipid/Water Phases of Use for Membrane Protein Reconstitution*. Langmuir, 1999. **15**(23): p. 8225-8234.
166. Zuidam, N.J., et al., *Lamellarity of cationic liposomes and mode of preparation of lipoplexes affect transfection efficiency*. Biochim Biophys Acta, 1999. **1419**(2): p. 207-20.
167. Seelig, J. and H. Gally, *Investigation of phosphatidylethanolamine bilayers by deuterium and phosphorus-31 nuclear magnetic resonance*. Biochemistry, 1976. **15**(24): p. 5199-204.
168. Seelig, J. and A. Seelig, *Lipid conformation in model membranes and biological membranes*. Q Rev Biophys, 1980. **13**(1): p. 19-61.
169. Mbamala, E.C., A. Fahr, and S. May, *Electrostatic model for mixed cationic-zwitterionic lipid bilayers*. Langmuir, 2006. **22**(11): p. 5129-36.

170. Levadny, V. and M. Yamazaki, *Cationic DMPC/DMTAP lipid bilayers: local lateral polarization of phosphatidylcholine headgroups*. Langmuir, 2005. **21**(13): p. 5677-80.
171. Mohammed-Saeid, W., et al., *Development of lyophilized gemini surfactant-based gene delivery systems: influence of lyophilization on the structure, activity and stability of the lipoplexes*. J Pharm Pharm Sci, 2012. **15**(4): p. 548-67.
172. Pupo, E., et al., *Preparation of plasmid DNA-containing liposomes using a high-pressure homogenization--extrusion technique*. J Control Release, 2005. **104**(2): p. 379-96.
173. Carstens, M.G., et al., *Evaluation of the high-pressure extrusion technique as a method for sizing plasmid DNA-containing cationic liposomes*. J Liposome Res, 2011. **21**(4): p. 286-95.
174. Pinnaduwege, P., L. Schmitt, and L. Huang, *Use of a quaternary ammonium detergent in liposome mediated DNA transfection of mouse L-cells*. Biochim Biophys Acta, 1989. **985**(1): p. 33-7.
175. Kawakami, S., et al., *Asialoglycoprotein receptor-mediated gene transfer using novel galactosylated cationic liposomes*. Biochem Biophys Res Commun, 1998. **252**(1): p. 78-83.
176. Kearns, M.D., Y.N. Patel, and M. Savva, *Physicochemical characteristics associated with transfection of cationic cholesterol-based gene delivery vectors in the presence of DOPE*. Chem Phys Lipids, 2010. **163**(8): p. 755-64.
177. Lappalainen, K., et al., *Comparison of cell proliferation and toxicity assays using two cationic liposomes*. Pharm Res, 1994. **11**(8): p. 1127-31.
178. Aberle, A.M., et al., *A novel tetraester construct that reduces cationic lipid-associated cytotoxicity. Implications for the onset of cytotoxicity*. Biochemistry, 1998. **37**(18): p. 6533-40.
179. Lv, H., et al., *Toxicity of cationic lipids and cationic polymers in gene delivery*. J Control Release, 2006. **114**(1): p. 100-9.
180. Stover, T., et al., *[In vitro neurite outgrowth induced by BDNF and GDNF in combination with dexamethasone on cultured spiral ganglion cells]*. Laryngorhinootologie, 2007. **86**(5): p. 352-7.
181. Bonnet, D., et al., *Brain-derived neurotrophic factor signalling in adult pig retinal ganglion cell neurite regeneration in vitro*. Brain Res, 2004. **8**: p. 1-2.
182. Barbacid, M., *The Trk family of neurotrophin receptors*. J Neurobiol, 1994. **25**(11): p. 1386-403.
183. Kimpinski, K., R.B. Campenot, and K. Mearow, *Effects of the neurotrophins nerve growth factor, neurotrophin-3, and brain-derived neurotrophic factor (BDNF) on neurite growth from adult sensory neurons in compartmented cultures*. J Neurobiol, 1997. **33**(4): p. 395-410.
184. Barker, P.A. and E.M. Shooter, *Disruption of NGF binding to the low affinity neurotrophin receptor p75LNTR reduces NGF binding to TrkA on PC12 cells*. Neuron, 1994. **13**(1): p. 203-15.
185. Danzer, S.C., et al., *Increased Expression of Brain-Derived Neurotrophic Factor Induces Formation of Basal Dendrites and Axonal Branching in Dentate Granule Cells in Hippocampal Explant Cultures*. The Journal of Neuroscience, 2002. **22**(22): p. 9754-9763.

186. Houchin-Ray, T., et al., *Non-viral gene delivery transfection profiles influence neuronal architecture in an in vitro co-culture model*. Biotechnol Bioeng, 2009. **103**(5): p. 1023-33.
187. McCall, J., et al., *Optimization of adult sensory neuron electroporation to study mechanisms of neurite growth*. Front Mol Neurosci, 2012. **5**: p. 11.
188. Xie, T.D., L. Sun, and T.Y. Tsong, *Study of mechanisms of electric field-induced DNA transfection. I. DNA entry by surface binding and diffusion through membrane pores*. Biophys J, 1990. **58**(1): p. 13-9.
189. Deister, C. and C.E. Schmidt, *Optimizing neurotrophic factor combinations for neurite outgrowth*. J Neural Eng, 2006. **3**(2): p. 172-9.
190. Cao, X. and M.S. Shoichet, *Investigating the synergistic effect of combined neurotrophic factor concentration gradients to guide axonal growth*. Neuroscience, 2003. **122**(2): p. 381-9.
191. Leclere, P., et al., *Effects of glial cell line-derived neurotrophic factor on axonal growth and apoptosis in adult mammalian sensory neurons in vitro*. Neuroscience, 1998. **82**(2): p. 545-58.
192. Gavazzi, I., et al., *Growth responses of different subpopulations of adult sensory neurons to neurotrophic factors in vitro*. Eur J Neurosci, 1999. **11**(10): p. 3405-14.
193. McMahan, S.B., et al., *Expression and coexpression of Trk receptors in subpopulations of adult primary sensory neurons projecting to identified peripheral targets*. Neuron, 1994. **12**(5): p. 1161-71.
194. Cui, Q., et al., *Expression of trkA, trkB, and trkC in injured and regenerating retinal ganglion cells of adult rats*. Invest Ophthalmol Vis Sci, 2002. **43**(6): p. 1954-64.
195. Frank, L., et al., *BDNF down-regulates neurotrophin responsiveness, TrkB protein and TrkB mRNA levels in cultured rat hippocampal neurons*. Eur J Neurosci, 1996. **8**(6): p. 1220-30.
196. Cheng, L., et al., *TrkB gene transfer protects retinal ganglion cells from axotomy-induced death in vivo*. J Neurosci, 2002. **22**(10): p. 3977-86.
197. Horn, K.P., et al., *Another barrier to regeneration in the CNS: activated macrophages induce extensive retraction of dystrophic axons through direct physical interactions*. J Neurosci, 2008. **28**(38): p. 9330-41.
198. Yucel, Y.H., et al., *Histomorphometric analysis of optic nerve changes in experimental glaucoma*. J Glaucoma, 1999. **8**(1): p. 38-45.
199. Kitayama, M., et al., *Activated microglia inhibit axonal growth through RGMA*. PLoS One, 2011. **6**(9): p. e25234.
200. Lu, L.Q. and Y.C. Lu, *[Myelin associated inhibitors and regeneration of optic nerve]*. Zhonghua Yan Ke Za Zhi, 2006. **42**(9): p. 854-8.
201. Pan, C., et al., *Comparative proteomic phenotyping of cell lines and primary cells to assess preservation of cell type-specific functions*. Mol Cell Proteomics, 2009. **8**(3): p. 443-50.
202. Doughty, M.J. and M.L. Zaman, *Human corneal thickness and its impact on intraocular pressure measures: a review and meta-analysis approach*. Surv Ophthalmol, 2000. **44**(5): p. 367-408.
203. Reinstein, D.Z., et al., *Stromal thickness in the normal cornea: three-dimensional display with artemis very high-frequency digital ultrasound*. J Refract Surg, 2009. **25**(9): p. 776-86.

204. Hamalainen, K.M., et al., *Characterization of paracellular and aqueous penetration routes in cornea, conjunctiva, and sclera*. Invest Ophthalmol Vis Sci, 1997. **38**(3): p. 627-34.
205. Urtti, A., *Challenges and obstacles of ocular pharmacokinetics and drug delivery*. Adv Drug Deliv Rev, 2006. **58**(11): p. 1131-5.
206. Mohan, R.R., et al., *Gene therapy in the cornea: 2005--present*. Prog Retin Eye Res, 2012. **31**(1): p. 43-64.
207. Kolle, S.N., et al., *In-house validation of the EpiOcular(TM) eye irritation test and its combination with the bovine corneal opacity and permeability test for the assessment of ocular irritation*. Altern Lab Anim, 2011. **39**(4): p. 365-87.
208. Hathout, R.M., et al., *Liposomes as an ocular delivery system for acetazolamide: in vitro and in vivo studies*. AAPS PharmSciTech, 2007. **8**(1): p. 1.
209. Mitjans, M., et al., *Low potential ocular irritation of arginine-based gemini surfactants and their mixtures with nonionic and zwitterionic surfactants*. Pharm Res, 2003. **20**(10): p. 1697-701.
210. Peeters, L., et al., *Vitreous: a barrier to nonviral ocular gene therapy*. Invest Ophthalmol Vis Sci, 2005. **46**(10): p. 3553-61.
211. Kawakami, S., et al., *In vivo gene transfection via intravitreal injection of cationic liposome/plasmid DNA complexes in rabbits*. Int J Pharm, 2004. **278**(2): p. 255-62.
212. Uematsu, M., et al., *Gene Transfer to the Eye Utilizing the Cationic Liposomes After Intravitreal Injection in Rabbits*. Invest. Ophthalmol. Vis. Sci., 2005. **46**(5): p. 5193-.
213. Liao, H.W. and K.W. Yau, *In vivo gene delivery in the retina using polyethylenimine*. Biotechniques, 2007. **42**(3): p. 285-6.
214. Dalkara, D., et al., *Inner limiting membrane barriers to AAV-mediated retinal transduction from the vitreous*. Mol Ther, 2009. **17**(12): p. 2096-102.
215. Gaudana, R., et al., *Ocular drug delivery*. AAPS J, 2010. **12**(3): p. 348-60.
216. Savige, J., et al., *Retinal basement membrane abnormalities and the retinopathy of Alport syndrome*. Invest Ophthalmol Vis Sci, 2010. **51**(3): p. 1621-7.
217. Candiello, J., et al., *Biomechanical properties of native basement membranes*. FEBS J, 2007. **274**(11): p. 2897-908.
218. Harvey, A.R., et al., *Intravitreal injection of adeno-associated viral vectors results in the transduction of different types of retinal neurons in neonatal and adult rats: a comparison with lentiviral vectors*. Mol Cell Neurosci, 2002. **21**(1): p. 141-57.
219. Pitkanen, L., et al., *Neural retina limits the nonviral gene transfer to retinal pigment epithelium in an in vitro bovine eye model*. AAPS J, 2004. **6**(3): p. e25.
220. Puras, G., et al., *Low molecular weight oligochitosans for non-viral retinal gene therapy*. Eur J Pharm Biopharm, 2012. **8**(12): p. 00308-6.
221. Bochot, A., et al., *Intravitreal delivery of oligonucleotides by sterically stabilized liposomes*. Invest Ophthalmol Vis Sci, 2002. **43**(1): p. 253-9.